RADIATION EFFECTS IN THIN FILM HEXAGONAL BORON NITRIDE

THESIS

Nathaniel M. Kaminski, CPT, USA

AFIT-ENP-MS-16-M-072

DEPARTMENT OF THE AIR FORCE
AIR UNIVERSITY

AIR FORCE INSTITUTE OF TECHNOLOGY

Wright-Patterson Air Force Base, Ohio

DISTRIBUTION STATEMENT A
APPROVED FOR PUBLIC RELEASE; DISTRIBUTION UNLIMITED

AFIT-ENP-MS-16-M-072

RADIATION EFFECTS IN THIN FILM HEXAGONAL BORON NITRIDE

THESIS

Presented to the Faculty
Department of Engineering Physics
Graduate School of Engineering and Management
Air Force Institute of Technology
Air University
Air Education and Training Command
in Partial Fulfillment of the Requirements for the
Degree of Master of Science

Nathaniel M. Kaminski, MS
CPT, USA

March 2016

DISTRIBUTION STATEMENT A
APPROVED FOR PUBLIC RELEASE; DISTRIBUTION UNLIMITED

AFIT-ENP-MS-16-M-072

RADIATION EFFECTS IN THIN FILM HEXAGONAL BORON NITRIDE

THESIS

Nathaniel M. Kaminski, MS
CPT, USA

Committee Membership:

Michael R. Hogsed, PhD
Chair

James C. Petrosky, PhD
Member

John W. McClory, PhD
Member

AFIT-ENP-MS-16-M-072

Abstract

The effects of ion and gamma radiation on hBN are investigated to determine the suitability of hBN as a substrate material for device operation in a radiation environment. To study the radiation response of thin film hBN, metal insulator semiconductor (MIS) devices were fabricated via chemical vapor deposition (CVD) with the insulator composed of either a 2 nm or 12 nm layer of hBN. Current-voltage (I-V), capacitance-voltage (C-V), and impedance spectroscopy measurements were compared to quantify changes in hBN resistance due to radiation induced displacement damage. The hBN resistance exhibited no discernible degradation up to high levels of displacement damage and total ionizing dose relative to Earth orbit satellite environments. MIS devices exposed to gamma irradiation from a Co-60 source with a total dose deposition of 3.1 Mrad(Si) exhibited a small increase in hBN resistance and no observable C-V shift associated with charge trapping. MIS devices irradiated with 4.5 MeV silicon ions showed no significant resistivity decrease to a threshold fluence of 1×10^{12} for the 2 nm sample and 5×10^{12} ions/cm^2 for the 12 nm sample, beyond which both devices exhibited hard dielectric breakdown. This result suggests a correlation between threshold ion fluence and a thickness dependent critical density of displacement defects. Conduction mechanism fitting showed some evidence of a transition from electrode limited conduction mechanisms to bulk limited conduction mechanisms at threshold ion fluence in both the 2 nm and 12 nm hBN samples, however, this result is inconclusive and requires further research.

AFIT-ENP-MS-16-M-072

Dedicated to the village because it takes a village to raise a leader. To my step father Ronald who past away during the course of this research. Over the short time I had Ron in my life, he emphasized "education is the one thing nobody can ever take away from you" which inspired me to attend West Point, become an engineer, and to never stop asking questions. Finally, to my sons who I hope will flip through this document someday and become inspired to do more than I could ever imagine in my life.

Acknowledgements

First and foremost, I would like to express my sincere appreciation to the director of the Sandia National Laboratories Ion Beam Laboratory for the ion beam time and the fantastic support that went along with it. You could not ask for a better group of scientists, engineers, and technicians to work with. Without their support or the tandem ion beam time, my research would have been a lot less interesting. It truly was an amazing first experience using a multi-million dollar equipment setup to conduct a real science experiment that I'll never forget, so Thank You!

I would like to thank Dr. Michael Snure from the Air Force Research Laboratory for the research funding and providing the material devices which made this research possible. To my committee members, Dr. James Petrosky and Dr. John McClory, thank you for your time, encouragement, and support throughout my research. In particular, I would like to thank Dr. James Petrosky for his contributions in setting up the initial coordination with the Ion Beam Laboratory. Thank you for giving me the opportunity and access to equipment and facilities that enriched both my experience and research efforts while I was at AFIT.

To my research advisor, LtCol (Dr.) Michael Hogsed, I can't thank you enough for all the effort and time spent with me over the last six months. Over the course of those six months, I went from understanding absolutely little about semiconductors and MIS devices, to developing a modest understanding. A lot of that is owed to fact that you were willing to spend large blocks of time that sometimes spanned a few hours to talk about theory and answer whatever questions I had. What I most enjoyed were our talks centered around drawing figures and equations on a white board because out of it came the best ideas which propelled this research forward.

Next, I want to thank all the friends, mentors, commanders, supervisors, and subordinates who helped me get to where I am at in life. Of note, I would especially

like to thank my company first sergeant and battle buddy who endured hell with me and never gave up trying to improve our foxhole.

Finally, I would like to thank my wife who epitomizes all the romanticized values of spartan women. She has been there with me from the start of this journey through all the rigors that come with officership and supporting other families as the family readiness group leader through two deployments. Not to mention, surviving a tornado, a family move, company command, and giving birth to twins all within the same year. Yet again, she was there to support me through all the late nights and long weekends associated with this research. No words can describe my admiration for the strength, support, and encouragement that she has provided me since I have known her, and I hope that I may somehow to find a way to return the favor in full. I love you!

Nathaniel M. Kaminski

Table of Contents

List of Figures

Figure Page

List of Tables

RADIATION EFFECTS IN THIN FILM HEXAGONAL BORON NITRIDE

I. Introduction

1.1 Background

Radiation resistant electronics have been integral to the aerospace, nuclear, and military communities for many years. From the 1950's through present day, silicon has been the fundamental material that the overwhelming majority of semiconductor electronic devices have been built upon. Through advancements in science and technology, miniaturization of those electronics has been realized and developed at a pace consistent with Gordon E. Moore's 1975 prediction, better known as Moore's law. The properties of silicon are well understood, and commercial manufacturing is currently configured to adapt the latest material or process advancement to a silicon substrate. However, the semiconductor industry has predicted that device scaling will not continue indefinitely as small scale architectural limitations are approached [3]. As a result, a search is underway for new materials with better electrical properties with carbon based materials identified as likely candidates for use in complementary metal-oxide semiconductors (CMOS) devices [4].

One particular carbon based material which has shown promise for a high current conduction capability is graphene. The structure of graphene is composed of a two dimensional (2D) layer of carbon atoms arrayed in a honeycomb lattice which possesses high intrinsic electron mobility at room temperature [5]. Monte Carlo simulations that incorporate electron-phonon interactions in graphene as defined by density functional perturbation theory have predicted an electron mobility of

$9.5 \times 10^5\,\mathrm{cm^2/(V \cdot s)}$ at $\mathrm{T} = 300\,\mathrm{K}$ which is in reasonable agreement with experimental results [5]. However, the achievement of this measured mobility in graphene was in the absence of a substrate, and the practical application of graphene in transistors currently requires a compatible substrate. When graphene was computationally modeled with a traditional silicon oxide (SiO_2) substrate, electron mobility in the graphene was reduced to $25,000\,\mathrm{cm^2/(V \cdot s)}$ [5]. The reduction in electron mobility is primarily due to additional scattering caused from dangling bonds in the lattice structure mismatch between the 3D geometry of SiO_2 and flat 2D geometry of graphene [4, 5].

In contrast, when graphene was computationally modeled on top of hexagonal boron nitride (hBN) substrate, an increased electron mobility of $140,000\,\mathrm{cm^2/(V \cdot s)}$ was calculated [5]. The mobility improvement is primarily due to the hBN being an insulating isomorph of graphene with an improved $\sim 1.6 - 1.7\%$ lattice mismatch to graphene [6, 7]. Additionally, due to inert van der Waals bonding in the vertical direction, hBN is theoretically suitable for use as a substrate material for other 2D materials irrespective of lattice matching. Therefore hBN shows promise as a substrate for graphene and other 2D materials. However, thin film hBN growth techniques are relatively immature, and research into large area growth and device fabrication is ongoing [6]. As a result, much remains unknown about how hBN will perform in a harsh radiation environments which may be applicable in both commercial and government applications.

1.1.1 hBN Material Characteristics and Properties

hBN is a wide band gap III-V compound with a direct band gap ranging between 5.2 to 5.9 eV, an optical band gap of 5.69 eV, and a theoretical density of

2.275 g/cm^3 [8, 9, 10, 11]. The structure and composition of hBN discrete nano layers is shown in Figure 1 [12].

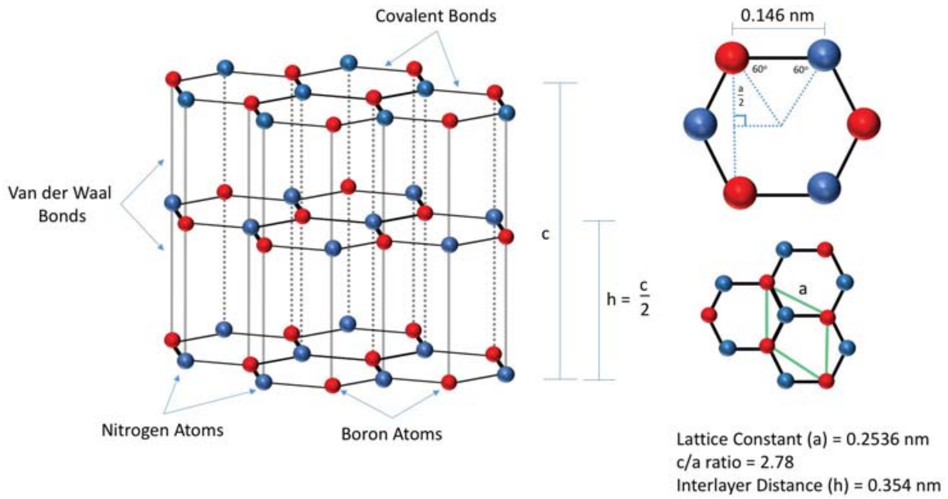

Figure 1. Theoretical lattice structure, dimensions, and composition of hBN discrete layers.

As shown in Figure 1, hBN is composed of alternating nitrogen and boron atoms; forming a 2D hexagonal geometric lattice layer arrangement with a theoretical lattice constant of 0.2536 nm and interlayer distance of 0.354 nm [12]. These theoretical dimensions are in close agreement with experimental measurements which show the interlayer distance as approximately 0.33 nm [13, 14, 15]. Atoms in each layer of hBN are bound together by strong covalent bonds, and the layers of hBN are held together by weak van der Waals forces [16]. Dielectric properties of hBN include experimentally reported permittivity values between 4.16 - 4.95 perpendicular to the plane and 2.21 - 4.10 parallel to the plane [17] with a breakdown voltage $V_{breakdown} \approx 7$ MV/cm [18]. For this study, a dielectric permittivity value of 4 was used for all calculations.

The crystalline form of hBN of interest for advanced electronic applications is a simple crystal structure grown by chemical vapor deposition (CVD). This is advantageous because single crystalline structures contain fewer charge trapping centers which should allow for a rapid sweep out of electrons and holes generated in an ionizing radiation [15]. However, it is not well understood exactly how hBN performs in the presence of an ionizing radiation environment.

Understanding the structure, electrical characteristics, and variability of the test devices is critical to being able to attribute radiation effects. Part of the device performance variability in some hBN thin films stem from the transition of a well ordered crystalline growth to a polycrystalline growth beyond the first couple of hBN layers grow on a substrate during the CVD process. This phenomenon is shown in Figure 2 taken by transmission electron microscopy (TEM) at the Air Force Research Laboratory (AFRL).

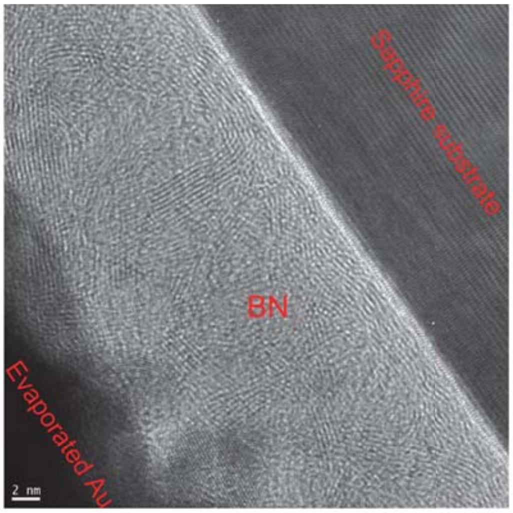

Figure 2. TEM Image of hBN grown on a sapphire substrate by CVD. Image provided courtesy of Dr. Michael Snure, AFRL.

The image shown in Figure 2 depicts hBN grown on a sapphire substrate. Polycrystalline growth was suspected to also occur on a silicon substrate, but after the first couple of deposited nano layers [19]. Polycrystalline growth lowers the resistivity of the hBN through the creation of conduction paths parallel to the disordered hBN layers/planes making the overall hBN superstructure less of an ideal insulator. Though this idea does not appear to be discussed in the literature, it is plausible because electrical resistivity is greatest in the direction perpendicular to the hBN layer/plane due to the inert van der Waals bonds which hold layers of hBN. This effect is in addition to any defect mediating conduction paths that are also created along the grain boundaries. Grain boundaries impede conduction in a good conductor, but for conduction through hBN in the vertical direction the net effect could be an increase in conductivity due to grain boundaries. Apart from the material growth, other sources of variability arise from statistical error associated with handling of the samples between the numerous manufacturing/measurement processes such as deposition of contacts and uniformity of temperature distribution during annealing.

1.1.2 Previous Radiation Effect Studies

To date of this publication, a literature review has yielded limited published information about radiation effects on thin film hBN. Previous AFIT research conducted with Co-60 gamma and fission reactor energy spectrum neutron irradiation indicated the radiation response was primarily due to the pre-existing and further induced interface charge characteristics at the hBN and silicon junction [1]. As supporting evidence, a negative voltage shift was reported and attributed to positive space charge production at the hBN/Si interface following neutron irradiation as shown in Figure 3. This result bears some similarity to research on x-ray effects on back gated graphene transistors where radiation induced oxide trapped charge near the graphene and silicon oxide interface increased the resistance of the device and required a larger positive gate bias voltage to neutralize the trapped charge [4].

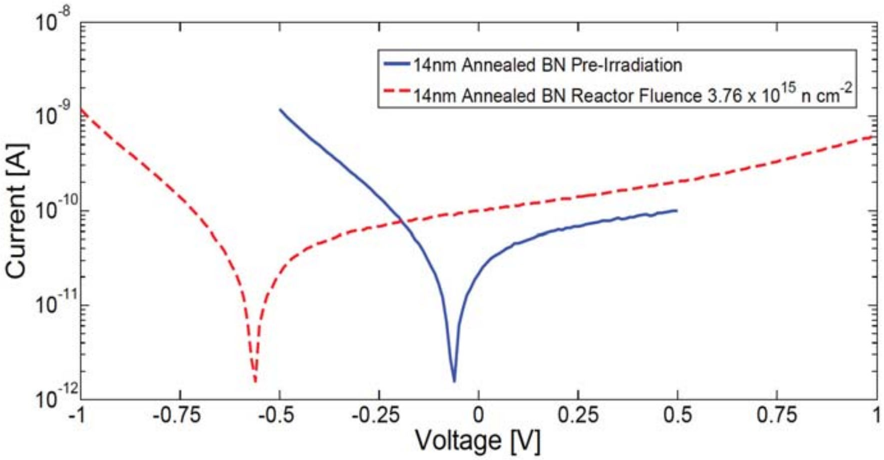

Figure 3. Current as a function of bias voltage for a 14nm hBN device plotted on a linear-logarithmic scale showing a device voltage shift following neutron irradiation. [1]

Other publications have yielded experimental inferential or theoretical evidence of radiation effects on hBN. Relatively thick films of hBN ($0.3\,\mu$m) have been used in the experimental fabrication of neutron detectors that capitalize on the large thermal neutron absorption cross section (~ 5380 barns) [15]. Furthermore, Doan points out that hBN has a demonstrated negligible response to gamma ray interactions. In reference to transistor device fabrication techniques, another article indicated that low energy silicon ion implantation conducted on hBN films 1 μm thick was observed to increase the hBN resistance from vacancy formation achieved with a fluence of 2.5×10^{15} ions/cm^2[9]. These studies almost invariably involved relatively thick films of hBN; however, requirements for high quality growth make thin films of primary interest for 2D electronic applications, and the radiation response of thin films can, in principle, vary considerably from thick films.

1.2 Electrical Device Composition

The devices used in this study are Metal-Insulator-Silicon (MIS) devices with hBN grown on top of a silicon (P doped) substrate through CVD. The configuration of the device is shown in Figure 4. The device layout is the same for all samples with devices possessing hBN insulating layer thickness of either 2 or 12 nm. Following growth of hBN onto the silicon substrate, metalization deposited the gold/nickel front contact. A diamond scribe was used to cleave samples from the main wafer, and all samples were annealed at 600 °C for 37 seconds (which included 7 seconds for temperature ramp up and ran ramp down) prior to being measured.

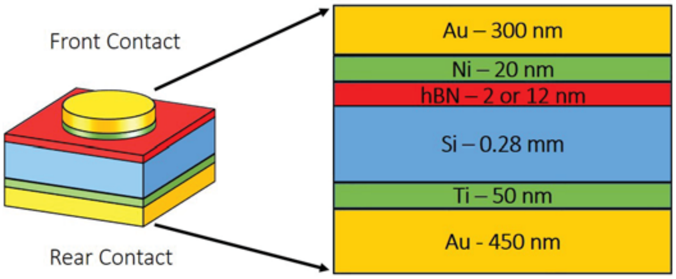

Figure 4. Structural layout and composition of hBN transistor MIS device under evaluation.

1.3 Research Purpose

The purpose of this research is to determine and characterize the radiation hardness of hBN through irradiating the MIS devices described above. This was achieved using ion and gamma irradiation to create displacement damage and charge traps in the hBN layer/depletion region of the device. High energy ions create both ionization and displacement damage whereas a typical gamma ray energy spectrum, as in a nuclear reactor or prompt nuclear weapon, primarily interact with matter through absorption and Compton scattering, causing ionization damage. The advantage of selecting ion irradiation over neutron irradiation is the ability to obtain a mono-energic beam of ions tailored to achieve a desired damage depth profile. Studying the effects of both ions and gamma irradiation facilitates a comparison to distinguish the effects in an MIS device caused through ionization and displacement damage.

1.4 Hypothesis

This research began with the hypothesis the hBN MIS device would exhibit changes in resistance in the hBN dielectric layer due to radiation induced displacement damage. The resistivity of the hBN thin film dominates the overall resistance presented by the MIS device with resistivity of hBN reported between $5 \times 10^{10} - 1 \times 10^{13}\,\Omega - \text{cm}$ [15]. Therefore small amounts of displacement damage in the hBN film are expected to create a detectable level of additional conductivity through the thin film before the conductivity of the Si substrate is affected. Furthermore, it was hypothesized the turbostatic structure of the hBN thin film would present opportunities for charge trapping in the presence of ionizing radiation similar to that seen in the oxide layer of MOS devices.

1.5 Research Objectives

The main objective of this research was to establish how the resistivity of the hBN changes in the presence of radiation through experimental in situ and post irradiation I-V, C-V, and impedance measurements to refine a hBN conduction path model used in previous research [1]. The previous conduction path model accounted for Frenkel-Poole (a bulk limited conduction mechanism) and Fowler-Nordheim (an electrode limited conduction). However, bulk limited conduction mechanisms are primarily a function of trap energies and densities within a dielectric whereas the electrode limited conduction mechanisms are primarily a function of potential barriers between material layers. Therefore, it is assumed if charge trapping is occurring in the bulk dielectric, analysis of the bulk limited conduction mechanisms through data fitting can be used to inferentially derive information about trap density and energy in the bulk dielectric.

1.6 Methods

The methods for this research consist of experimental electrical measurements and computational modeling. Equivalent circuit models are developed for the MIS device under test, and compared against measured impedance spectroscopy data through complex fitting analysis to solve for electronic properties of the MIS device.

1.7 Limitations

There were many constraints in this study that primarily stemmed from sample fabrication and measurement equipment capability limitations. The number of samples available for study were limited due to a highly specialized small scale production process. Even though a number of samples were available, the density of functioning devices per sample area was small. Initial contact problems were believed to be caused by the metal contact work function incompatibility with the hBN and annealing temperature. The combination of replacing the Ti/Au metal contacts with Ti/Ni contacts and increased anneal temperature to 600 °C improved device functionality, but ultimately, functionality was limited to the present growth quality of the hBN.

As shown above, the growth quality of the hBN is still an immature process that is unable to produce uniform layers of hBN beyond a few atomic layer. The hBN grown on all samples used in this study is believed to resemble more of a polycrystalline structure which contributes to leakage current through the device. As a result of the growth quality and associated leakage current, the applied gate voltage bias was limited to a range of -0.6 to 0.9 volts for a 12 nm hBN sample and -0.21 to 0.21 for a 2 nm sample. Due to the limited applied voltage range, it is believed that the C-V measurements in this study represent only a portion of the entire curve. With only a portion of the C-V curve obtained, detecting and characterizing a flat band voltage shift became more difficult. Furthermore, the Keithley 4200 limited the C-V frequency sweep range to between 1×10^7 - 1,000 Hz divided into 37 unalterable frequency presets. The inability to obtain lower frequency capacitance measurements below 1,000 Hz prevented the acquisition of full impedance measurements which significantly limited the accuracy of that technique for measurement of the hBN resistance.

II. Theory

This chapter is broken into five sections. The first three sections will cover basic semiconductor fundamentals describing the operating characteristics of the MIS device. The fourth section will discuss theory related to impedance spectroscopy, and the fifth section will cover radiation interactions and effects on the MIS device.

2.1 Ideal MIS Electronic Theory

The theory describing the electronic operation of MIS devices is fundamentally based upon Ohm's law defined as equation 1.

$$V = IR \tag{1}$$

The variable I represents the amount of current through a system in units of amps, R is resistance in units of ohms, and V is the resultant voltage, or potential, in units of volts. In equation 1, the current is related to voltage through a linear proportionality with resistance. However, the MIS devices used in this study exhibit a non-linear current response with an applied linear change in voltage as shown in Figure 5. In the ideal state, the MIS device represent a series capacitor, or as a capacitor and resistor in parallel as current conduction is a function of the frequency dependent applied voltage. As a result, Ohm's law must be modified to account for the frequency dependent resistance (impedance) of the dielectric capacitance. Before discussing impedance further, the idealities and non-idealities that allow the MIS device to be represented as a resistor-capacitor network will be described through energy band and semiconductor theory.

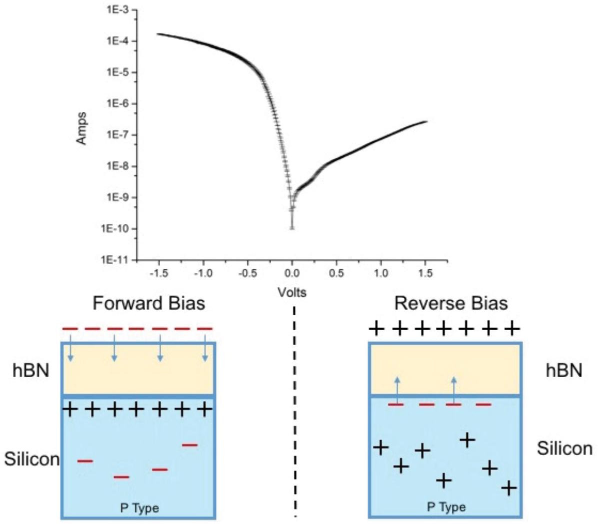

Figure 5. Typical I-V response of a hBN/silicon p-type MIS device.

In general, the energy band diagram describes potential barriers that carriers must overcome to flow through a device; measured as total current. The flat energy band diagram for the ideal MIS device is shown in Figure 6 which was extracted and updated from previous work on this subject[1].

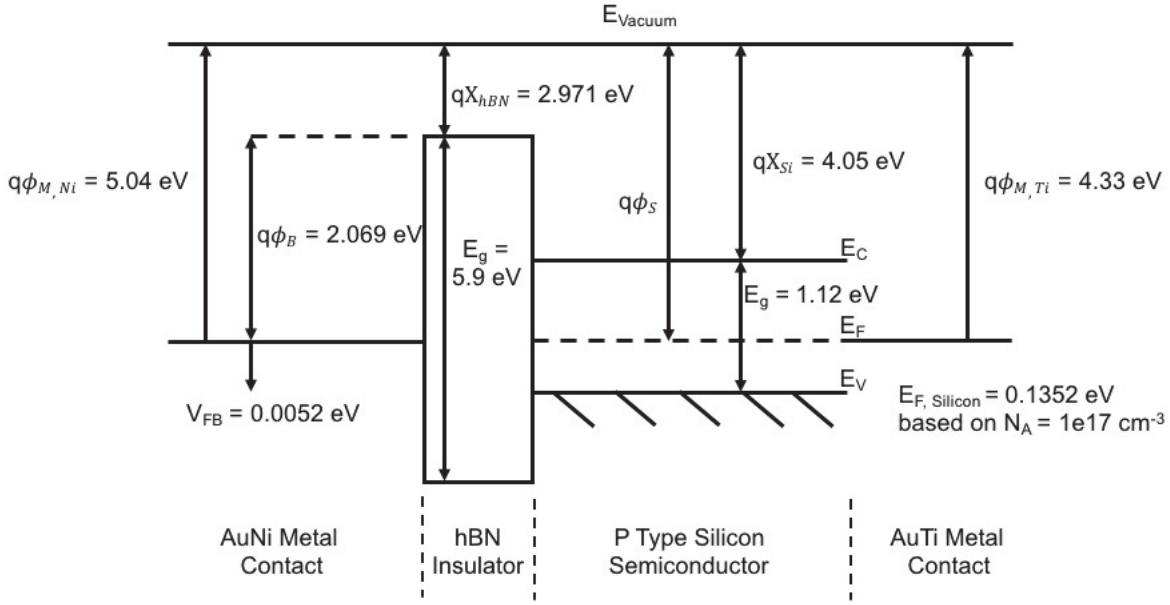

Figure 6. Flat band energy diagram for hBN/silicon MIS device.

From left to right in Figure 6, the various material layers of the MIS device are represented beginning with the nickel metal contact layer that interfaces with the hBN layer. Each material has different properties ultimately affecting the amount of energy required to move an electron from the Fermi level (E_F) of the metal contact, over or through a potential barrier (ϕ_B), and into the conduction band (E_C) of the semiconductor. The Fermi level is a statistical description of the highest energy level an electron occupies within a material. For a metal, the Fermi level is given by the metal work function (ϕ_M) with the work function defined as energy require to eject (remove) an electron from the surface to vacuum level. The metal work function is experimentally measured through the photoelectric effect at room temperature, and is a table lookup value usually regarded as a temperature independent constant. On the other hand, the Fermi level energy for a semiconductor material is dependent on both material temperature and doping level related through equations 2 and 3.

$$E_F = -kT\,ln(\frac{N_A}{n_i}) + E_i \tag{2}$$

$$E_i = \frac{E_g}{2} + \frac{3}{4}\,kT\,ln(\frac{m_p^*}{m_n^*}) \tag{3}$$

In the above equations, E$_i$ represents the intrinsic energy level which is very close to the mid gap energy of the undoped semiconductor with the value ($E_g/2$) used as an approximation, n_i is the intrinsic carrier concentration often set equal to 10^{10} cm^{-3} in room temperature silicon, N_A (cm^{-3}) is the doped acceptor concentration of the semiconductor, $m_\mathrm{p}^* = 0.81$ and $m_\mathrm{n}^* = 1.18$ are the effective hole and electron mass respectively in silicon, E_g is the energy band gap of the semiconductor (1.12 eV representing silicon), and finally T and k represent temperature and Boltzmann's constant. The work function for the silicon then becomes the difference between silicon Fermi energy level and the sum of the silicon electron affinity (χ_{Si}) as shown in equation 4.

$$\phi_S = \chi_{si} + E_g - E_F \tag{4}$$

$$\phi_{MS} = V_{FB} = (\phi_M - \phi_S)\, q \tag{5}$$

Under an ideal state, the flat band energy diagram is obtained when the work function between the metal contact and semiconductor are equal with no applied bias voltage. If the work function of the metal contact and semiconductor differ, the flat band energy diagram is obtained through applying a bias voltage equal to the difference between metal contact and semiconductor as calculated in equation 5. Furthermore, a rectifying contact is formed between the metal and semiconductor when the work function of the metal is smaller than the semiconductor work function ($\phi_M < \phi_S$) in a p type device. This effect is shown in Figure 5 where the current output is higher under a negative bias and smaller under a positive voltage bias.

When the voltage applied to the metal contact is less than the flat band voltage, an accumulation of majority carriers (holes for p type silicon) occurs at the hBN/silicon interface which causes the depletion region to decrease and capacitance to increase. As the voltage applied becomes greater than the flat band voltage, the majority carriers are pushed away from the hBN/silicon interface. Net carrier generation and recombination fall into a state of equilibrium forming a region at the interface that is depleted of carriers known as the “depletion region”. Under an applied voltage much greater than the flat band voltage, inversion occurs as net minority generation increases causing minority carriers to accumulate at the hBN/silicon interface. This is marked by the intrinsic energy level crossing below the Fermi energy level which implies the charge at the hBN/silicon has been inverted as shown in Figure 7.

In an ideal MIS device, the hBN acts as an ideal dielectric which prevents carriers from freely moving between the contact and semiconductor as shown in Figure 7. With current blocked, charge will accumulate at the interface between the insulator and semiconductor and can be measured as capacitance. Capacitance varies as function of applied gate voltage which can be experimentally measured as a C-V curve with data plotted to obtain a curve such as the example shown in Figure 8.

In Figure 8, an ideal and non ideal C-V curve is shown with accumulation, depletion, and inversion regions marked. This ideal C-V curve is consistent with a p-type semiconductor and follows the band diagram explanation described above. From the ideal C-V curve the capacitance of the hBN (C_{ox}) can be obtained when the slope of the curve reaches zero when the device is under strong accumulation [21]. With the capacitance of the hBN, properties such as the permittivity, experimental flat band voltage, and threshold voltage an be obtained through the application of equations 6 to 9. K_{ox} is the dielectric constant of the hBN, ϵ_o is the permittivity of free space, ϵ_S is the permittivity of the semiconductor, λ is the Debye length, A_G is the area of the gate, and t_{ox} is the actual thickness of the hBN layer. The experimental flat band voltage can be extracted using equation 7 to find the flat band capacitance and corresponding voltage.

$$C_{ox} = \frac{K_{ox}\epsilon_o A_G}{t_{ox}} \tag{6}$$

$$C_{FB} = \frac{\frac{C_{ox}\epsilon_S A_G}{\lambda}}{C_{ox} + \frac{\epsilon_S A_G}{\lambda}} \tag{7}$$

$$\lambda = (\frac{\epsilon_S kT}{q^2 N_A})^{0.5} \tag{8}$$

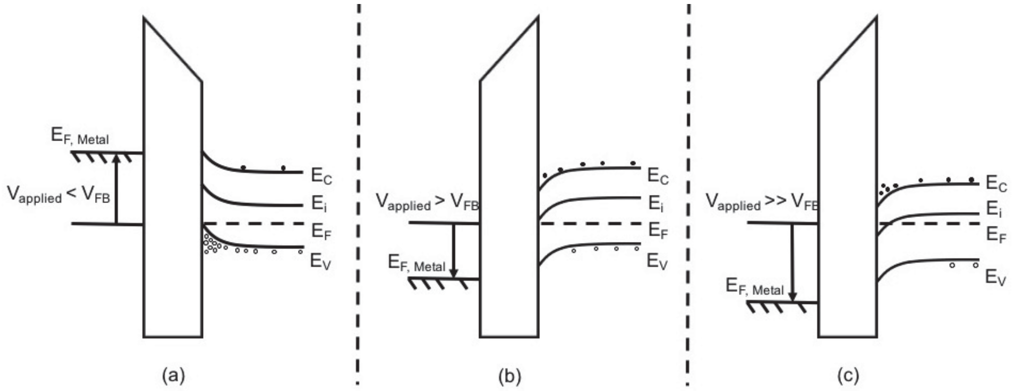

Figure 7. Energy band diagrams for an ideal MIS (p type) device under various applied voltages. (a) Applied voltage is less than the flat band voltage causing majority carriers to accumulate at the hBN/silicon interface. (b) Applied voltage is greater than the flat band voltage; carrier generation and recombination fall into a quasi-state of equilibrium forming a region depleted of carriers at the hBN/silicon interface. (c) Applied voltage is much greater than the flat band voltage causing minority carriers to accumulate at the hBN/silicon layer; forming a region where the net charge is inverted. [20]

$$V_{TH} = [\pm\frac{A_G}{C_{ox}}\sqrt{4\epsilon_S q|N_A|\,|E_F|} + 2E_F] + V_{FB} \tag{9}$$

2.2 Non-Ideal MIS Electronic Theory

Up to this point, theory primarily related to an ideal MIS device has been presented. The non-ideal MIS device follows from the same theory; however, the non-ideal theory better describes known defects in SiO_2 rather than hBN which is a 2D structure under ideal conditions and free of the presence of oxygen and dangling bonds. In the non-ideal state, charge trapping occurs in the dielectric and along the dielectric/semiconductor interface affecting the device response to an applied gate voltage which is undesirable. The four main types of oxide charges are mobile ions (Q_m), oxide trapped charge (Q_{ox}), fixed oxide charge (Q_{f}), and interface trapped charge (Q_{it}) as depicted in Figure 9.

Mobile ions are due to the deposition of ion impurities such as Li^+, K^+, Na^+ and possibly H^+ during thermal and CVD fabrication processes. The presence of positive ionic charge in the dielectric will cause a substantial voltage shift in the

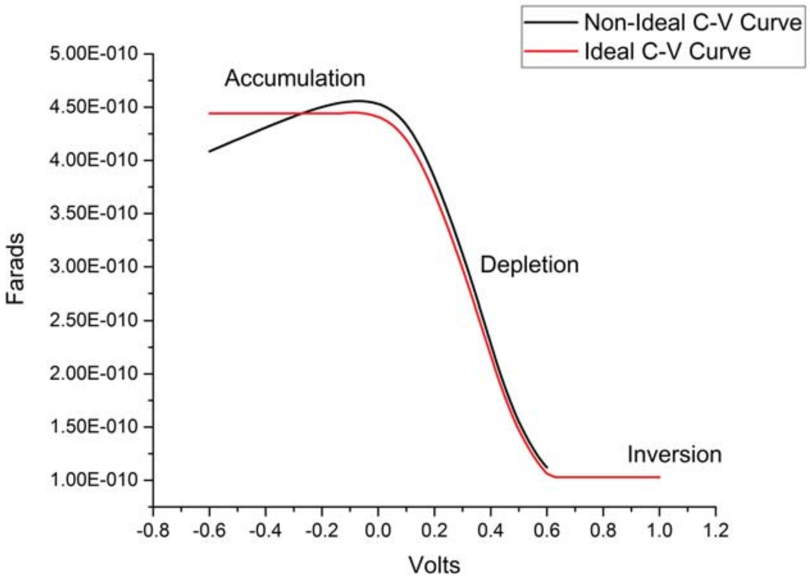

Figure 8. Typical C-V response of a hBN/silicon p-type MIS device.

negative direction as a function of device operating time, with the overall effect represented in equation 10. Furthermore, the mobile ion concentration can be determined through measuring the voltage shift in the C-V curve caused by bias temperature stressing of an MIS device and applying equation 11, where N_m (charge/cm^2 eV) represents the density of mobile ion charges [22].

$$\Delta V_G = -\frac{1}{K_o \epsilon_o} \int_0^{t_{ox}} x\, \rho_{ion}(x)\, dx = -\frac{Q_m}{C_o} = -\frac{Q_m t_{ox}}{K_o \epsilon_o} \tag{10}$$

$$N_m = \frac{K_o \epsilon_o \Delta V}{q\, t_{ox}} = \rho_{ion}(x) \tag{11}$$

Oxide trapped charge associated with defects in the dielectric material, are initially neutral charge centers, and therefore independent of applied gate voltage similar to ionic charge trapping. The oxide traps become positively or negatively charged upon the introduction of electrons and holes into the dielectric under an applied voltage [20]. In insulators such as SiO_2, there are known defects which

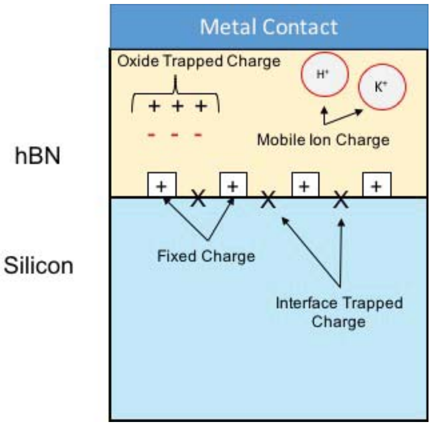

Figure 9. Oxide charge location diagram. [2]

create oxide trapped charge. However, hBN is less likely to be affected by oxide trapped charge as hBN is typically free from the presence of oxygen.

Another method of charging the oxide traps is radiation induced ionization. Again radiation induced charging may produce positive or negative charge traps, with positive traps causing a negative voltage shift and negative traps causing a positive voltage shift. The oxide trapped charge can be determined through high frequency C-V measurements with the traps generally annealed out in a low temperature ($< 500\,^{\circ}$C), nitrogen ambient environment [22]. Equation 12 represents the voltage shift due to oxide trapped charge, and is essentially equal to equation 10.

$$\Delta V_G = -\frac{1}{K_o \epsilon_o} \int_0^{t_{ox}} x\, \rho_{ox}(x)\, dx \;= -\frac{Q_{ox}}{C_o} = -\frac{Q_{ox} t_{ox}}{K_o \epsilon_o} \tag{12}$$

Fixed oxide charges are positive. Immobile charges located at or near the hBN/semiconductor interface, which are unaffected by an applied gate bias. Typically fixed charges are formed due to silicon oxidation during the fabrication process which can be reduced to a minimum through annealing in an inert atmosphere [2]. The theoretical change in gate voltage is shown as equation 13.

$$\Delta V_G = -\frac{Q_F}{C_o} \tag{13}$$

Lastly, interface traps are created through the formation of unsatisfied (dangling bonds) at the interface between the hBN/silicon due to the abrupt termination of the silicon lattice. Those unsatisfied dangling bonds can either form donor or acceptor sites, and charge or discharge as a function of applied bias voltage[2]. Equation 14 represents the voltage shift due to interface traps, with total charge a function of the semiconductor surface potential (ϕ_S).

$$\Delta V_G = -\frac{Q_{it}(\phi_S)}{C_o} \tag{14}$$

The cumulative result of the trap mechanisms described above lead to a shift in the threshold voltage as shown in equations 15 to 17. Furthermore, these methods of charge trapping lead to the formation of additional conduction mechanisms through the dielectric, which are addressed in the subsequent section. In equation 17, the variable K_{ox} is the dielectric constant of the hBN, K_S is the dielectric constant of the silicon, ϵ_o is the permittivity of free space, E_F is fermi energy, $N_A$is the doped acceptor concentration of the semiconductor, and t_{ox} is the actual thickness of the hBN layer.

$$V_{FB} = \phi_{MS} - \frac{Q_f - Q_m - Q_{ox} - Q_{it}}{C_o} \tag{15}$$

$$V_{TH} = V_{TH}^{'} + V_{FB} \tag{16}$$

$$V_{TH}^{'} = 2\,E_F \pm \frac{K_S}{K_{ox}} t_{ox} \sqrt{\frac{4qN_A}{K_S \epsilon_o}(\pm E_F)} \tag{17}$$

2.3 Conduction Paths through a Dielectric

The previous section described the charge trapping mechanisms which cause the dielectric to become a non-ideal insulator. Under those conditions, the dielectric will possess properties of both an insulator and resistor where current will flow through the dielectric material. The mechanisms describing the conduction pathways through the dielectric is the focus of this section with all theory stemming from author Fu-Chien Chiu [23] unless otherwise noted. The conduction mechanisms are broken into two broad groups consisting of electrode limited and bulk limited conduction mechanisms.

2.3.1 Electrode Limited Conduction Mechanisms

Electrode limited mechanisms occur outside the dielectric bulk material and depend on electrical properties at the metal contact and dielectric interface. Electrode limited conduction mechanisms consist of Schottky emission, Fowler Nordheim Tunneling (FNT), direct tunneling, and thermionic field emission (TFE). Under thermionic emission, electrons in the metal contact obtain enough energy by thermal activation to overcome the barrier height (ϕ_B) at the metal/hBN interface. This is the most often observed conduction mechanism in dielectric thin films, especially at high temperature, and is described by equation 18. E is the electric field across the dielectric, A^* is Richardson's constant, m^* is the effective electron mass, ϵ_r the optical dielectric constant, and J is the current density through the dielectric. For hBN, the effective electron mass varies, but a value of $m^* = 0.26$ has been used in other studies [24, 1].

$$J_{TE} = A^* T^2 \, exp(\frac{-q(\phi_B - \sqrt{\frac{qE}{4\pi\epsilon_r\epsilon_o}}}{kT}) \tag{18}$$

When the energy of the incident electron is less than the potential barrier, the electron will be reflected. However, based on quantum mechanics there is a probability the electron wave will penetrate a barrier less than 100 angstrom. FNT occurs when the applied electric field is large enough that the electron will penetrate through the barrier into the conduction band of the dielectric with attributable current density given in equation 19.

$$J_{FNT} = \frac{q^3E^2}{8\pi hq\phi_B} exp(\frac{-8\pi(2qm_T^*)^{0.5}}{3hE}\,\phi_B^{\frac{3}{2}}) \tag{19}$$

$$J_{DirectTunnel} \approx exp\{-\frac{8\pi(q\phi_B)^{\frac{3}{2}}\sqrt{2m_T^*}}{3hq\,|E|}[\frac{3|V|}{2\phi_B}]\} \tag{20}$$

The variable m_T^* is defined as the dielectric tunneling electron effective mass which tends to increase in mass as the thickness of the dielectric decreases. As the dielectric thickness increases beyond 4 nm, the tunneling electron effective mass is assumed to be equal to the electron effective mass. As the dielectric thickness decreases to less than 3.5 nm, the current density resultant from direct tunneling dominates over FNT which is expressed as equation 20. The variable V represents the voltage across the dielectric and E is the electric field across the dielectric. Another possible conduction mechanism is a combination between Schottky emission and tunneling which is known as thermionic field emission. In thermionic field emission, the electrons have an energy greater than the metal contact Fermi level, but less than the energy needed to overcome the dielectric potential barrier (ϕ_B). As a result, electrons that are thermally excited and don't have quite enough energy to achieve thermionic emission, will have a greater probability of tunneling through the dielectric barrier. The current density produced through thermionic field emission is shown as equation 21.

$$J_{TFE} = \frac{q^2\sqrt{m}(kT)^{0.5}E}{8\hbar^2\pi^{\frac{5}{2}}} exp(-\frac{q\phi_B}{kT}) exp(\frac{\hbar^2 q^2 E^2}{24m(kT)^3}) \tag{21}$$

2.3.2 Bulk Limited Conduction Mechanisms

Bulk limited conduction mechanisms occur inside the dielectric bulk material and are directly dependent on the properties of the dielectric with the most important property being trap energy level in the dielectric film. Conduction mechanisms that fall under the broad category of bulk limited include Frenkel-Poole (FP) emission, hopping conduction, ohmic conduction, ionic conduction, and space charge limited conduction.

Frenkel-Poole emission is similar to thermionic emission; however, the electrons are located in traps within the dielectric. Those trapped electrons may be ejected from a trap through thermal excitation. Furthermore, an applied electric field across the dielectric can reduce the coloumbic potential energy barrier in one direction and increase the probability of thermally exciting the electron out of a trap. The current density due to FP emission is shown as equation 22, and is most often observed at high temperature (300-400 K) and under a high electric field ($> 1\,\mathrm{MV/cm}$). The variable N_C represents the density of states in the conduction band of the dielectric, ϕ_T is the trap energy level, ϵ_i is the permittivity of the insulator, and μ is the electron drift mobility in the dielectric.

$$J_{FP} = q\mu N_C E\, exp(\frac{-q(\phi_T - \sqrt{\frac{qE}{\pi\epsilon_i\epsilon_o}}}{kT}) \tag{22}$$

Hopping conduction is due to electrons moving from one trap site to another via tunneling through the dielectric barrier, and corresponds to the direct tunneling electrode limited mechanism. In hopping conduction, the electron energy is lower than the potential barrier between two trap sites, but the electron has a non-negligible probability of tunneling through the barrier. The current density due to hopping conduction is represented in equation 23. The variable a is the mean distance between traps, n represents the electron concentration in the dielectric conduction band, ν is the electron thermal vibration frequency at the trap site, and Ea is the difference between the trap state energy level and the bottom of the dielectric conduction band. Furthermore, hopping conduction provided a well fitted correlation with experimental data under an electric field larger than 0.25 MV/cm [23].

$$J_{Hopping} = qan\nu \, exp(\frac{qaE}{kT} - \frac{Ea}{kT}) \tag{23}$$

Ohmic conduction results from the movement of mobile electrons in the dielectric conduction band and holes in the valence band. At very low voltage, current density and applied electric field show a linear relationship. Although the energy band gap of the hBN is large, there will be a small number of carriers that may be generated through thermal excitation. These thermally excited carriers comprise the ohmic conduction current density with the Fermi level of the dielectric assumed to be close to the mid band gap energy as shown in equation 24. Ohmic conduction may be observed in experimental measurements if no other significant contribution from other conduction mechanisms exist in the dielectric material.

$$J_{Ohmic} = q\mu EN_C \, exp(-\frac{E_g}{2kT}) \tag{24}$$

Space charge limited (SCL) conduction is the injection of electrons from an ohmic contact which occurs at $V < V_{tr}$ where V represents the an applied gate voltage for ohmic conduction and V_{tr} represents the transition gate voltage where begins to occur. If traps are present within the insulator, at V_{tr} the increase density of electrons through the insulator begin to fill available traps, the fermi level begins to move closer towards the conduction band, and a space charge within the insulator starts to form. If the applied voltage continues to increase past V_{tr}, a point will be reached where all the traps become filled and the fermi energy level approaches the bottom of the conduction. The is known as the trap filled limit threshold voltage V_{TFL}. At V_{TFL}, all the traps are filled, a large space charge is formed within the insulator, and electron mobility rather than electron density dominates conduction through the insulator with electron mobility limited by density of space charge build up. Assuming monoenergetic trap sites within the insulator, current density from SCL at the trap filled limit can be determined through equation 25.

$$J_{SCL} = \frac{9\epsilon_i \mu V^2}{8\, t_{ox}^3} \tag{25}$$

Ion conduction is the resultant current due to movement of ions in the dielectric under an applied bias voltage. Equation 26 expresses the current density stemming from ions generated from lattice defects where J_o is a proportional constant and d is the spacing of two nearby defect jump sites. Due to the large mass of ions, ionic conduction is usually not considered in most conventional applications.

$$J_{Ion\, Cond} = J_o\, exp[-(\frac{q\phi_B}{kT} - \frac{Eqd}{2kT})] \tag{26}$$

2.4 Circuit Model

Going back to equation 1, ohm's law is a relationship between current, voltage, and resistance. Section 2.3 described multiple pathways for current conduction through a dielectric, and section 2.2 described the rationale why those current conduction paths exist. This section will tie together theory presented through the use of equivalent circuits, to model the MIS device used in this study. In general, the networking of capacitors and resistors to create a circuit diagram is an accepted method to characterize the electrical behavior of MIS devices [25, 26]. A simple circuit model is presented in Figure 10 representative of a general MIS device.

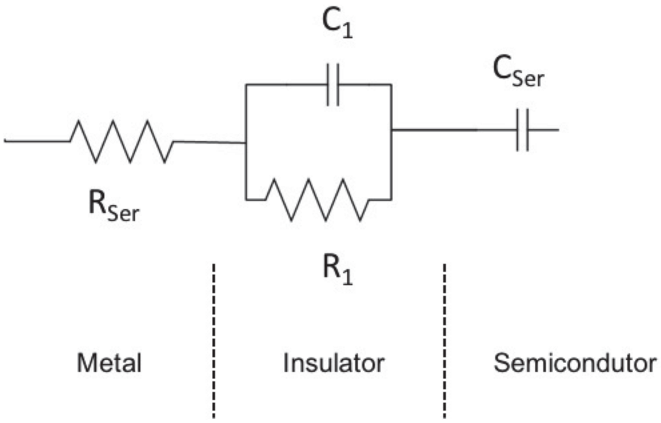

Figure 10. Simple RC circuit model representative of a MIS device.

In Figure 10, R_{Ser} represents any resistance stemming from the metal contact and bulk silicon substrate, R_1 is the cumulative parasitic conduction currents described as a resistance which provide an alternate conduction pathway, C_1 is the capacitance of the hBN, and C_{Ser} the capacitance of the silicon. Analyzing the circuit presented requires the conversion of all nodes to complex resistance known as impedance (Z) represented in equation 27 due to the voltage-time dependence $V(t)$ of the capacitors in the circuit. Impedance is the resistance to alternating current in a complex wire diagram that contains both resistors and capacitors. The conversions from impedance to capacitance and resistance are shown as equations 28 and 29, which are useful in understanding subsequent equations.

$$Z = \frac{V}{I} \tag{27}$$

$$Z_R = R \tag{28}$$

$$Z_C = \frac{1}{Cs} = \frac{1}{C\omega i} = \frac{1}{2C\pi f\, i} \tag{29}$$

To analyze the circuit shown in Figure 10, serial impedances are added together as shown in equation 30 and parallel impedances are added together as admittances (Y) then converted to impedance as shown in equations 31 and 32. The total impedance of the circuit is then represented as shown in equation 33.

$$Z_1 = R_{Ser} + \frac{1}{C_{Ser}s} \tag{30}$$

$$Y_2 = \frac{1}{R_1} + C_1 s \tag{31}$$

$$Z_2 = \frac{1}{Y_2} = \frac{1}{\frac{1}{R_1} + C_1 s} \tag{32}$$

$$Z_{total} = Z_1 + Z_2 = R_{Ser} + \frac{1}{C_{Ser}s} + \frac{1}{\frac{1}{R_1} + C_1 s} \tag{33}$$

From equation 33, it is possible to determine individual values for each capacitor and resistor in the circuit diagram through the use of impedance spectroscopy. Impedance spectroscopy is an experimental method that consists of measuring the total system impedance over a range of frequencies. Under a low frequency, a capacitor acts as an open circuit. As the frequency is increased, the capacitor becomes less resistive and current begins to flow through the capacitor as shown in equation 29. Measured impedance contains both a real component (Re) and imaginary component (jX), which are plotted against each other to produce Figure 11.

$$Z = Re + jX \tag{34}$$

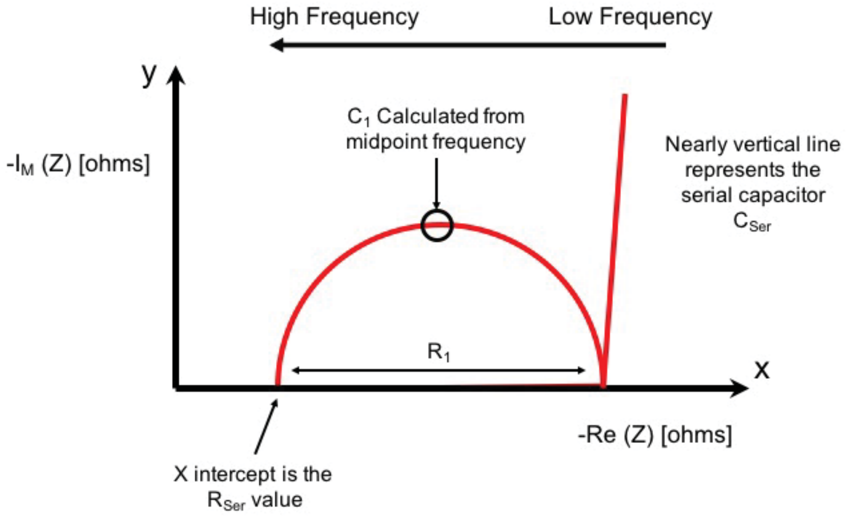

Figure 11. Plot of impedance complex plane.

Figure 11 is commonly known as a complex plane plot or “Nyquist” plot, with the y axis representing the imaginary component in units of ohms and the x axis representing the real component in units of ohms. Typically, the imaginary component has negative values, but is depicted as positive for ease of interpretation. The most prominent features in the plot are the semi-circle and straight line. The semi-circle represents the capacitor (C_1) and resistor (R_1) in parallel as shown in Figure 10. From the semi-circle, a capacitance value for (C_1) can be found through extracting an impedance data point at mid frequency and applying equation 29. Frequency is almost always implied in these plots with a decrease in frequency extending out from the origin [27].

2.5 Radiation Effects on MIS Devices

Incident radiation upon a device can alter the electrical properties of solid-state devices and integrated circuits through either ionizing or non-ionizing interactions dependent upon the type of radiation. For this experiment, the two types of incident radiation used were ions and gamma rays. Heavy ions are ionizing radiation that undergo kinetic interactions with atoms causing displacement defect formation. Defect formation can occur as a cascade event, a local cluster of defects, or many point defects scattered through the material, depending upon the total kinetic energy imparted by the incident radiation. After the scattering event, disordered regions within the material will attempt to “anneal” returning to their previous state. Annealing is material temperature dependent and often categorized as either short term or long term annealing. Short term annealing occurs within seconds to minutes after a defect is produced. Remaining defects will continue to reorder for periods as long as a year or more, which is known as long-term annealing.

The migration of point defects and defect clusters as well as additional clustering or dissolution of the clusters that occur during annealing are categorized as radiation damage effects. The rearrangement of atoms may alter material and device electrical properties, with one or more of the following events occurring when defect states are created in the band gap: 1) thermal generation of electron-hole pairs; 2) recombination of electron-hole pairs; 3) temporary trapping of carriers; 4) compensation of donors or acceptors by radiation induced centers; 5) tunneling of carriers through a potential barrier; 6) increased density of scattering centers due to radiation induced defects; 7) type conversion due to displacement damage induced carrier removal; and 8) radiation induced defects in the band gap, which enhance the effectiveness of thermally generated carriers [28].

Gamma rays are a form of ionizing radiation that interact with a material to eject electrons via the photoelectric effect, Compton scattering, or pair production depending on the energy of the gamma ray. The primary effect of ionizing radiation interactions is the generation of electron-hole pairs in the material. These additional electron hole pairs can affect MIS device operation through the formation of additional oxide traps and interface traps at the insulator/semiconductor junction. Under a positive bias, electrons are swept out of the dielectric, leaving behind a positive fixed charge that results in a negative voltage shift. Over time, recombination will occur neutralizing the fixed positive charge, with holes migrating slower than electrons.

The main observable radiation effects in this experiment will occur from the additional creation/passivation of oxide and interface traps as well as increased density of scattering centers from defect formation. The creation and passivation of oxide and interface traps can occur through either ionizing or non-ionizing radiation with the traps causing lateral shifts in the I-V and C-V measurements. In contrast, heavy ions will cause defect formations in the device which will affect material resistance; most likely resulting in vertical shifts of the I-V and C-V measurements as current and capacitance change.

III. Experiment and Procedures

An experimental approach was used to determine the radiation induced resistance change of the hBN in the MIS device with all measurements taken with the Keithley 4200 Semiconductor Characterization System. This approach consisted of a pre-characterization, irradiation, and post characterization process.

3.1 Pre/Post Device Measurement and Characterization

Pre-characterization consisted of first screening the MIS devices through conducting an I-V sweep with the Keithley 4200 used in conjunction with a probe station. Devices were unaffixed to any type of packaging, and placed directly on the probe station stage for measurement. Samples were then photographed to aid with identifying good devices and record keeping. Once a sample was deemed usable, the sample was silver epoxied onto a flatpack and heated to 150 ^{0}C for 15 minutes to cure the epoxy. Figure 12 depicts a prepared flatpack.

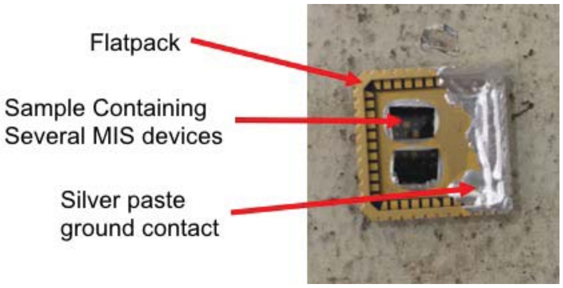

Figure 12. Prepared hBN MIS device sample for measurement and irradiation.

After affixing the sample to a flatpack, I-V, C-V, and impedance measurements were collected. Both I-V and C-V measurements were taken in voltage steps equal to the sweep range divided by 301 steps. For I-V measurements, the measurement hold time was set to 0 seconds and delay between successive sweeps set to 1 second. The C-V measurement hold time was set to 0.5 seconds, delay time between successive sweeps set to 1 second, with a parallel model capacitance used in all measurements to attain a capacitance and conductance measurement[21]. The measured capacitance value was then adjusted to compensate for effects of series resistance in the device using equations 35 through 37 where the variable G represents the measured conductance, C represents the measured capacitance, and f represents the frequency at which the capacitance measurement was taken [29]. All capacitance data shown in the analysis section are already adjusted through the use of these equations.

$$R_{Ser} = \frac{\left(\frac{G}{2\pi fC}\right)^2}{\left[1+\left(\frac{G}{2\pi fC}\right)^2\right]G} \tag{35}$$

$$a_R = G - \left(G^2 + (2\pi fC)^2\right) R_{ser} \tag{36}$$

$$C_{adjusted} = \frac{\left(G^2 + (2\pi fC)^2\right) C}{a_R^2 + (2\pi fC)^2} \tag{37}$$

Impedance measurements were taken across the maximum frequency range of the Keithley 4200 from 1,000 - 1×10^7 Hz in 37 independent predefined points with voltage bias held constant. Up to 10 I-V measurements were taken simultaneously and then averaged to yield a final measurement, while a single C-V and impedance measurement was used to characterize the device due to the amount of time required to acquire one measurement.

Upon completion of initial measurements, the best devices were chosen for wire bonding and preparation for in situ measurements. Wire bonding was accomplished by either AFRL or the AFIT clean room electronics lab. After devices were wire bonded, the same measurement process described above was repeated to determine whether or not the wire bonding process affected the device. Following experimentation, the same measurement process and measurement settings were used for post device characterization measurements after device irradiation.

3.2 Ion Irradiation Procedures

Ion irradiation took place at the Sandia National Laboratories (SNL) Ion Beam Laboratory where hBN MIS devices were irradiated with 4.5 MeV silicon ions at fluences ranging between $1 \times 10^9 - 2.13 \times 10^{13}\,\text{ions/cm}^2$. All samples were packaged on flatpacks as shown in Figure 12, and placed on a pinout shown in Figure 13 to obtain in situ measurements during irradiation. Prior to tearing down and packing lab equipment at AFIT labs for shipment to Sandia, a final set of measurements were taken with the flat pack inserted into the pinout shown in Figure 13 to note any anomalous fluctuations in I-V, C-V, and impedance measurements due to the experimental setup. However, no significant changes in any of the measurements were found.

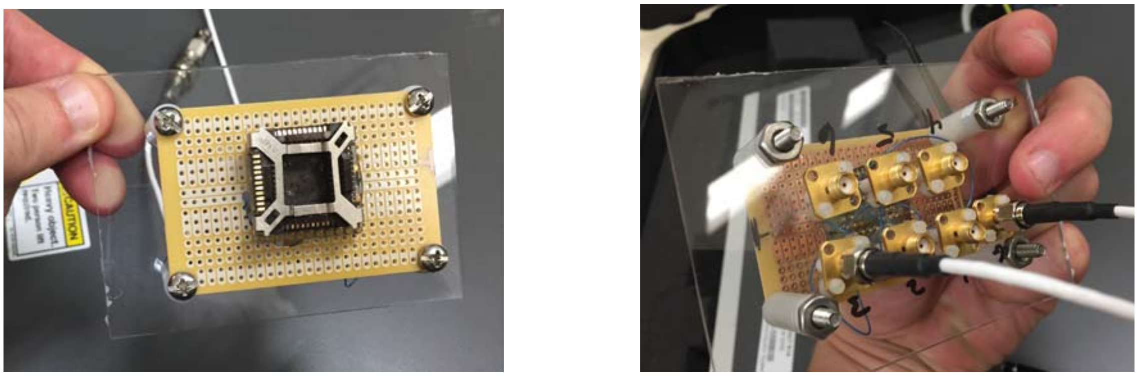

(a) Front (b) Back

Figure 13. Graphic of hBN flatpack experimental mount for ion beam in situ measurements.

Upon arrival at the ion beam laboratory, setup consisted of a methodical process to ensure electrical continuity and prevention of mis-wiring devices. The experimental setup was initiated by checking the pinout shown in Figure 13 to ensure correct wiring layout. Next the flatpack was inserted into the pinout, and measurements were taken with the Keithley 4200 to ensure the devices were functioning properly prior to insertion into the chamber. Finally with the flatpack mounted in the pinout, the entire pinout mount was attached to the stage for insertion into the chamber as shown in Figure 14. With the pinout mount attached to the stage, I-V measurements were taken following any major manipulation of the ion chamber such as closing the door and following chamber pump down to eliminate potential of collecting poor quality data at the start of ion irradiation. The first measurements were collected after pump down occurred at approximately 1×10^{-6} torr, with final chamber pressure equalizing between $6 \times 10^{-6} - 8 \times 10^{-6}$ torr.

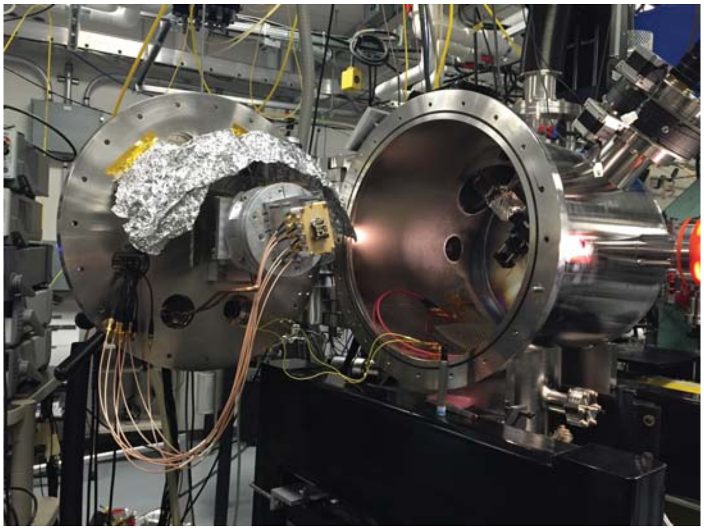

Figure 14. Ion beam experimental setup shown with sample mounted.

During irradiation, the procedure consisted of pulsing the beam at a given flux until a total desired fluence was achieved. This was done to limit heating of the sample, which could potentially cause annealing. After the desired total fluence was achieved, I-V, C-V, and impedance measurements were taken sequentially. No measurement was taken and contacts were grounded while the device was in the process of being exposed to the ion beam. Information pertaining to the radiation history and ion beam settings for samples studied are located in appendix B.

The rationale for choosing 4.5 MeV silicon ions was to achieve significant displacement damage in the hBN while ensuring the Bragg peak occurred deep in the bulk silicon substrate of the device. SRIM simulations were used to calculate the deposition depth with the result shown in Figure 15.

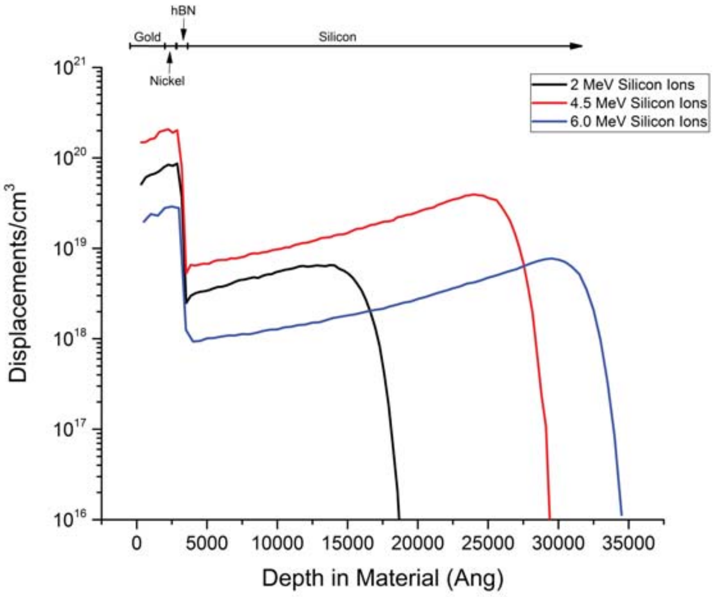

Figure 15. Comparison study of SRIM determined volumetric displacement damage for 2 MeV, 4.5 MeV, and 6 MeV silicon ions. The MIS device modeled in SRIM consisted of layers of gold (300 nm in depth), nickel (20 nm in depth), hBN (12 nm in depth), and silicon (3168 nm in depth) shown left to right in the graph.

3.3 Gamma Irradiation Procedures

Gamma irradiation took place at the Ohio State University Nuclear Research Laboratory (OSU-NRL) facility using a Co-60 source. Prior to irradiation, all samples were placed on flat packs shown in Figure 12, pre-characterized through I-V, C-V, and impedance measurements, and then wrapped in tin foil shown in Figure 16. Samples were wrapped in tin foil to ground the sample and prevent static discharge from occurring through the device. As an additional precaution, a large spot of silver paste (Figure 12) was added to permanently ground the bottom of the pack to the rim to ensure grounding once wrapped in tin foil. The prepared foil pack shown in Figure 16b was attached to the rig for insertion into a 6” dry tube for gamma irradiation. Prior to insertion, proper grounding was confirmed with a multimeter. The entire sample was lowered into the source, and left in place for 97 continuous hours of exposure achieving a total gamma dose of 3.1 Mrad(Si). After removal of the foil pack from the dry tube, the samples were immediately transported back to AFIT for measurement.

(a) Individual flat packs wrapped in foil

(b) Foil pack attached to rig for insertion into Co-60 source

Figure 16. Gamma irradiation experimental setup.

3.4 Circuit Analysis

Direct detection of individual conduction mechanism contributions is extremely difficult. To determine which conduction mechanisms correlated best with measured I-V data, functional fitting of conduction mechanisms to measured I-V data was used to approximate several mechanisms. This approximation relied on current density proportionality equations as shown in Table 1 (derived by Sze [20]). The proportionality equations shown in the column labeled “General Functional Fit” in Table 1 are representative of the full theoretical equations, except constants are grouped into a generic pre-factor. The equation pre-factor controls the overall magnitude of the fitted curve, which is only important to obtain a line of best fit. As a result, the variables left within the proportionality equations are independent variables such as bias voltage (V), which drive the shape of the fitted line. The column labeled “Refined Functional Fit” in Table 1 are a refinement to the general functional fit equations which mathematically expand generic variables and place constraints on certain electrical and material properties. The equations shown in the column labeled “Refined Functional Fit” of Table 1 for thermionic emission and space charge limited conduction are the full theoretical equation as discussed in section 2.3.

To fit the equations shown in Table 1 to experimental I-V measurements, a MATLAB script was created to standardize the process. Line fitting was first attempted with the equations shown within the column labeled “General Functional Fit” of Table 1. After that first fit, a second fit was attempted with the equations shown within the column labeled “Refined Functional Fit” of Table 1. Before attempting to fit the above equations to the experimentally measured I-V data, the

Table 1. Current density proportionality equations.

Process	General Functional Fit (1st order approximation)	Refined Functional Fit (2nd order approximation)
Tunneling	$J_{Tunneling} \propto V_i^2 exp(\frac{-b}{V_i})$	$J_{Tunneling} \propto E_i^2 exp\left(-\frac{4\sqrt{2m^*}(q\phi_B)^{(\frac{3}{2})}}{3q\hbar E_i}\right)$
Thermionic Emission	$J_{Thermionic\,Emission} \propto T^2 exp(\frac{q}{kT}(a\sqrt{V_i} - \phi_B))$	$J_{Thermionic\,Emission} = A^* T^2 exp(\frac{q}{kT}(\phi_B - \sqrt{\frac{qE_i}{4\pi\epsilon_i}}))$
Frenkel - Poole	$J_{Frenkel-Poole} \propto V_i^2 exp(\frac{q}{kT}(a\sqrt{V_i} - \phi_B))$	$J_{Frenkel-Poole} \propto E_i^2 exp(\frac{q}{kT}(\phi_B - \sqrt{\frac{qE_i}{\pi\epsilon_i}}))$
Ohmic	$J_{Ohmic} \propto V_i exp(\frac{-c}{T})$	$J_{Ohmic} \propto E_i exp(\frac{-Ea}{kT})$
Space Charge Limited	$J_{SCL} \propto V_i^2$	$J_{SCL} = \frac{9\epsilon_i \mu V^2}{8\, t_{ox}}$

MATLAB script first determined the electric field across the insulator through an iterative calculation of theoretical surface potentials at the hBN/silicon interface (ψ_{s}). After determining ψ_s, the voltage across the hBN insulator was calculated with equation 38.

$$V_i = V_{gate} - \psi_s - V_{Series\,Resistance} \tag{38}$$

In equation 38, the variable V_{gate} represents the applied gate voltage, and V_i represents the voltage drop across the insulator. To account for non-ideal voltage drops across the device, the variable $V_{Series\,Resistance}$ was added to equation 38 to represent the voltage potential across the front and back contacts. The values for the series resistance were calculated from the impedance analysis shown in the previous section.

With V_i, a set of five iterative routines were created to represent each of the five conduction mechanisms described by equations shown in Table 1. Each of the routines were design to determine an exact value for the pre-factor that provided a line of best fit to the experimental data through a half step iteration method. The statistical measurement R^2 which indicates goodness of fit was used to quantify the result and rank order conduction from most to least dominant.

The algorithm discussed above only focused on determining a correlation through the shape of the fitted line compared to the data. The next step was to further refine the conduction mechanism that best correlated to the measured data through both correct shape and magnitude of the fitted line to the measured I-V data; considered an absolute fit for the purposes of this document. To achieve an absolute fit, conduction mechanisms that provided the best correlation to the measured I-V data from functional fitting were selected. Then each conduction mechanism was individually fitted to the measured I-V data using a similar algorithm described above for functional fitting with values for independent variables selected to optimize a line of best fit.

To determine the hBN resistance, impedance spectroscopy measurements interpreted through Complex Nonlinear Least Squares (CNLS) fitting software was used to extract values for the various circuit components shown in Figure 17.

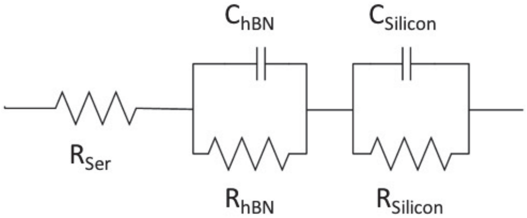

Figure 17. MIS device equivalent circuit represented by a network of capacitors and resistors.

Figure 17, depicts the basic circuit diagram of the MIS device. The series resistor R_{Ser} represents all of the external resistances not associated with hBN or silicon depletion region resistance. The two parallel sub-circuits represent the hBN and silicon with each layer possessing an associated capacitance and resistance. The resistance represents the leakage current pathway through the device described by the conduction mechanisms in the theory section. Under a large enough negative voltage, the depletion region at the silicon/hBN interface shrinks in size, so the measured resistance can be mostly attributed to the hBN due to the voltage drop occurring primarily across the insulator [23, 21].

IV. Results and Analysis

4.1 Chapter Overview

This chapter will define the average hBN MIS device performance parameters, and then discuss individual device results associated with the ion and gamma irradiations.

4.2 General Device Population Performance Parameters

Given the limited number of devices that yielded in-situ measurements, understanding the general population of MIS device electrical characteristic trends was critical to understanding how well the response of the irradiated devices represented that of the population. Characterizing general device performance was accomplished by using a random sample of devices that had not exhibited dielectric breakdown prior to irradiation. All measurements were normalized to account for varying pad size of each device. After normalizing the measurement, an average of all measurements was taken with the standard deviation determined through the use of Origin Lab graphing software. Figures 18 and 19 represent the sample population current and capacitance response as a function of voltage with the sample population consisting of five 2 nm and five 12 nm devices.

In Figures 18 and 19, the solid lines indicate the mean of five 12 nm and five 2 nm devices with corresponding color error bars indicating sample population variability. The larger error bar for the 12 nm sample compared to the 2 nm sample in Figure 18 is expected as the growth thickness of the 12 nm hBN layer was more variable due to process constraints of the CVD growth technique. Otherwise, general current and capacitance response general trends are in line with absolute hBN thickness differences between samples and provide an expected range of values.

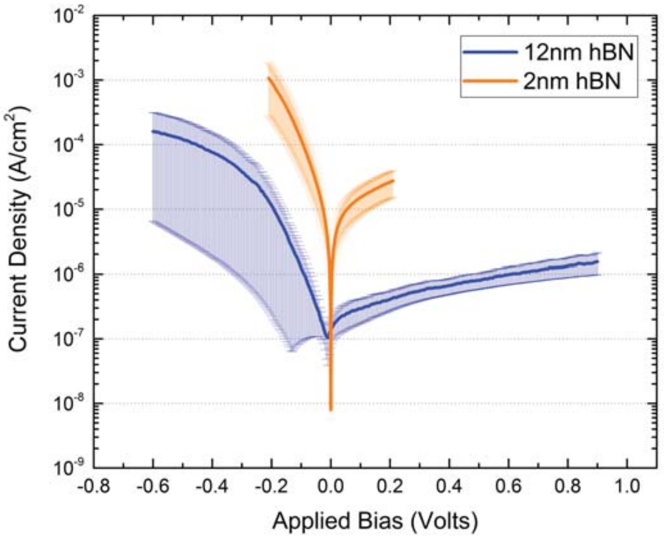

Figure 18. Average current density as a function of voltage for several 2 nm and 12 nm devices representative of the typical population.

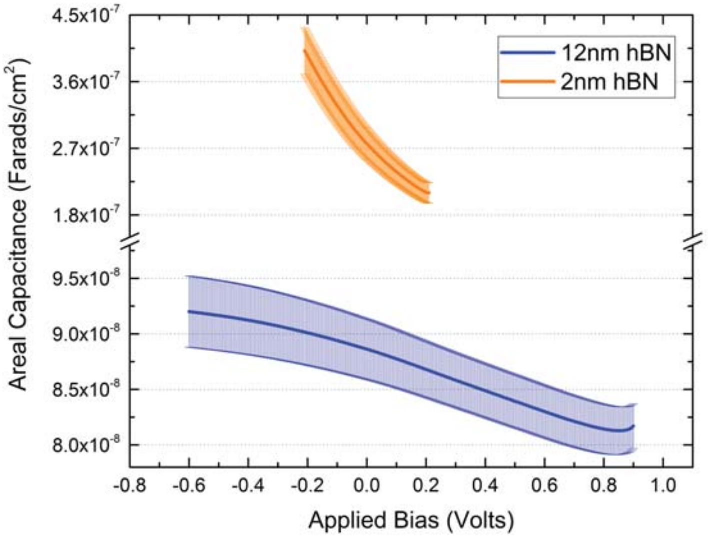

Figure 19. Average areal capacitance as a function of voltage measurements for several 2 nm and 12 nm devices representative of the typical population.

4.3 Device Response to Ion Irradiation

Several 2 nm and 12 nm samples were exposed to 4.5 MeV silicon ion irradiation to observe how displacement defects affected the electrical characteristics of the hBN MIS device. From those several samples, two samples yielded quality measurements attributed to radiation induced effects with all other sample results removed from this analysis due to experimental procedure error or dielectric breakdown unrelated to radiation effects. The two samples consisted of 2 nm and 12 nm samples labeled samples BN52715B_13C and BN72915_13C respectively. The 12 nm sample had a series of 21 sets of I-V, C-V, and impedance measures after 21 varying ion fluence doses. The 2 nm sample had a series of 7 sets of I-V, C-V, and impedance measures after 7 varying ion fluence doses. Both samples are compared through equivalent ion fluences shown in table 2. The overall result from the analysis of ion irradiation indicated that the resistivity of the hBN remained constant without any detectable change until a hBN thickness dependent total fluence threshold was reached. Upon crossing the threshold total fluence, the measured hBN resistance had a sharp decrease coinciding with I-V measurements indicating hard dielectric breakdown. This result will be explained in depth below, beginning with I-V data analysis.

Table 2. Comparison of total ion fluence deposited into 2 nm and 12 nm samples to show equivalent total fluence at selected intervals.

Total Ion Fluence Deposited At: (ions/cm^2)	BN52715B 13C 2 nm Sample	BN72915 13C 12 nm Sample
Chamber Pump Down	0	0
Post Radiation Shot 1	5.02×10^{10}	5.06×10^{10}
Post Radiation Shot 2	1.00×10^{11}	1.30×10^{11}
Post Radiation Shot 3	5.98×10^{11}	4.83×10^{11}
Post Radiation Shot 4	1.10×10^{12}	1.43×10^{12}
Post Radiation Shot 5	6.07×10^{12}	5.20×10^{12}
Post Radiation Shot 6	1.12×10^{13}	1.05×10^{13}
Post Radiation Shot 7	2.13×10^{13}	2.13×10^{13}

4.3.1 I-V Analysis

I-V analysis of the 2 nm and 12 nm samples showed similar electrical response as a function of total ion fluence with measurements shown in Figures 20 and 21. As total fluence increased, both devices exhibited minimal fluctuations in current under negative bias which is a preliminary indication that the resistance of the hBN insulator initially remained unaffected. As the total fluence reached and crossed the threshold fluence value of $1.10 \times 10^{12}\,\text{ions/cm}^2$ for the 2 nm sample and $5.20 \times 10^{12}\,\text{ions/cm}^2$ for the 12 nm sample, a substantial increase in current response was measured in both devices. Those threshold values mark the beginning of hard dielectric breakdown and are further substantiated through C-V measurement and I-V curve fitting analysis. After passing threshold fluence, the 2 nm sample showed an immediate breakdown response. Furthermore, each successive I-V measurement for the 2 nm sample after breakdown showed a dominant ohmic current conduction mechanism discussed in detail below. Breakdown in the 12 nm sample was more gradual with the threshold fluence coinciding with an elevated increase in current under negative bias. Even though there was a rise in current at a total fluence $5.20 \times 10^{12}\,\text{ions/cm}^2$ in the 12 nm sample, C-V measurement analysis showed that the device had not yet experienced breakdown at this point. Increasing fluence $5.20 \times 10^{12}\,\text{ions/cm}^2$ resulted in 12 nm device breakdown, with following I-V measurements showing a substantial increase in current under negative bias.

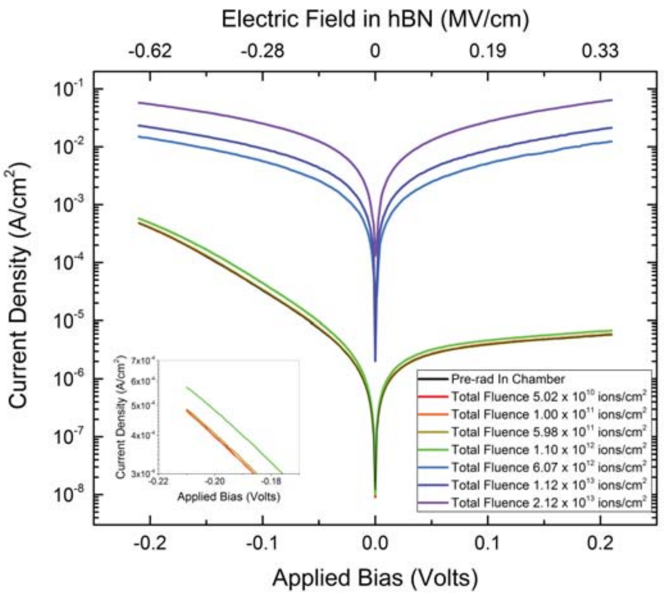

Figure 20. 2 nm hBN device current density as a function of ion fluence and applied bias. The inset graph provides an expanded view of the early radiation I-V measurements under negative voltage to show minor changes.

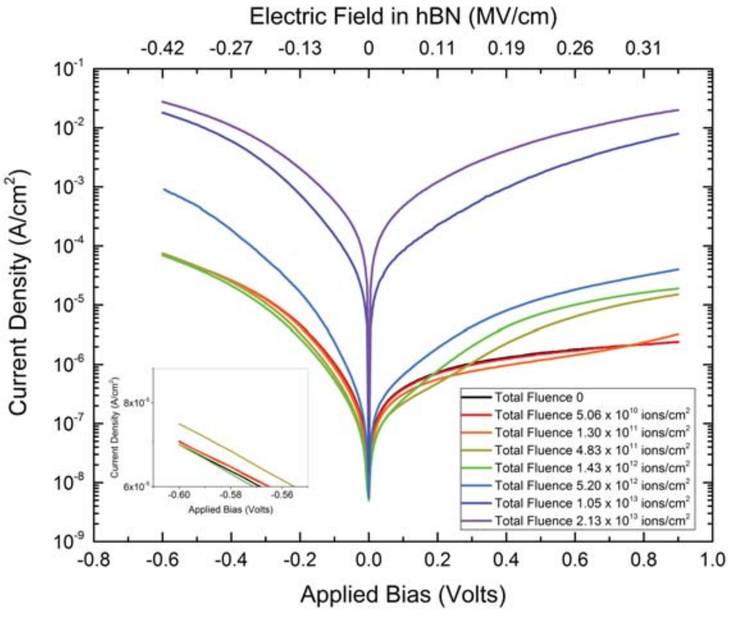

Figure 21. 12 nm hBN device current density as a function of ion fluence and applied bias. The inset graph provides an expanded view of the early radiation I-V measurements under negative voltage to show minor changes.

4.3.2 C-V Analysis

In general, I-V measurements for both devices indicate the resistance of the hBN insulator remains unaffected until a threshold fluence is achieved. However, as demonstrated in the C-V measurements, ion radiation had an observable affect on the device capacitance with increasing fluence that began as soon as the sample was irradiated. Figures 22 and 23 show capacitance measurements as a function of applied voltage for both the 2 nm and 12 nm samples, which indicates a linear decrease with total ion fluence. All capacitance measurements displayed in the figures were taken at a frequency of 1 MHz, so all capacitance measurements are regarded as high frequency. As the total ion fluence approaches and surpasses the threshold fluence, device breakdown is observed in the C-V measurements in the formation of concave up C-V curves. Interpretation of C-V measurements prior to device breakdown is meaningful as maximum capacitance corresponds to carrier accumulation under negative bias for high frequency C-V measurements. C-V measurements taken after device breakdown become more difficult to interpret because the capacitance meter becomes inaccurate at high levels of current.

Analysis of the C-V measurements prior to device breakdown indicate the decrease in capacitance is due to carrier removal. The carrier concentration following each ion fluence deposition was calculated from the C-V measurement using equation 39. In equation 39, the variable A represents the metal contact area, and $K_s\epsilon_0$ represents the permittivity of silicon. The results for carrier concentration are shown in table 3, and present a reduction in carrier concentration as fluence increased. This interpretation is supported by SRIM calculations which show the peak initial volumetric displacement as $10^{15} - 10^{18}$ displacements/cm^3 for the given fluences shown in Figure 15. Upon device breakdown, the calculated values for carrier concentration in both samples become unreliable as the C-V measurement is unreliable past breakdown.

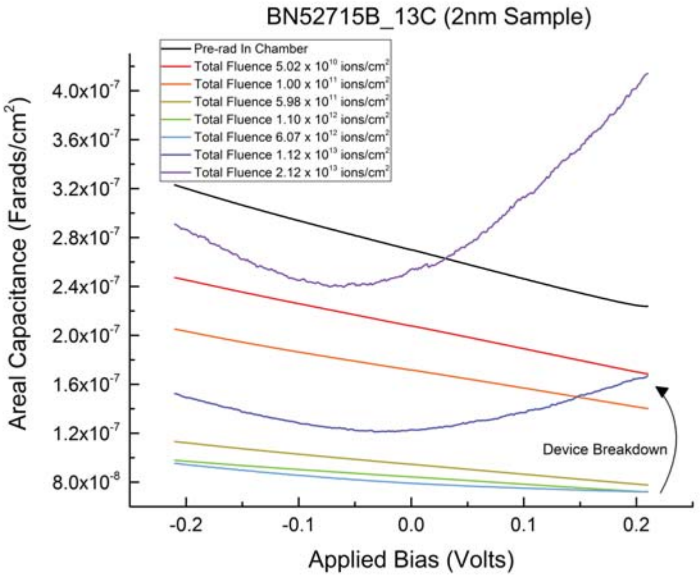

Figure 22. 2 nm hBN device areal capacitance as a function of ion fluence and applied bias.

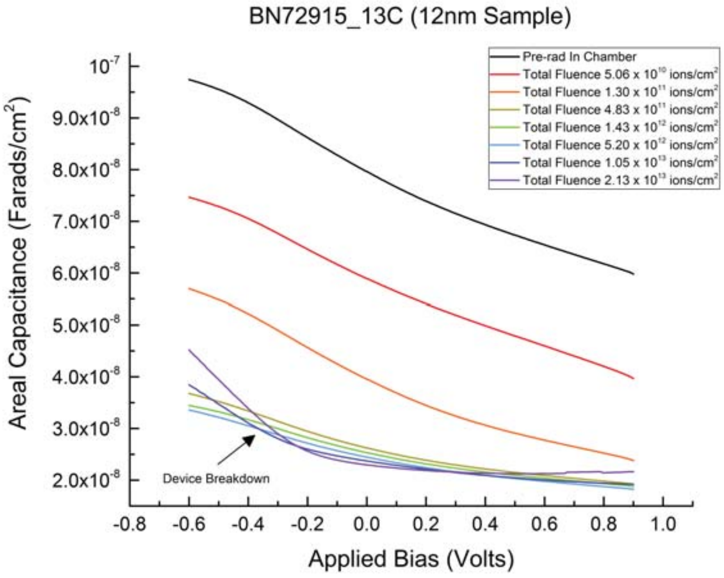

Figure 23. 12 nm hBN device areal capacitance as a function of ion fluence and applied bias.

$$N_A = \frac{2}{q\, K_s\, \epsilon_o\, A^2\, d(1/C^2)/dV} \tag{39}$$

Table 3. Experimentally calculated silicon hole concentration as a function of total ion fluence.

Silicon Hole Concentration At: ($1/\mathrm{cm}^3$)	BN52715B 13C 2 nm Sample	BN72915 13C 12 nm Sample
Chamber Pump Down	3.75×10^{17}	9.31×10^{16}
Post Radiation Shot 1	2.33×10^{17}	3.62×10^{16}
Post Radiation Shot 2	1.65×10^{17}	1.04×10^{16}
Post Radiation Shot 3	5.22×10^{16}	8.87×10^{15}
Post Radiation Shot 4	5.73×10^{16}	8.89×10^{15}
Post Radiation Shot 5	4.98×10^{16}	8.28×10^{15}
Post Radiation Shot 6	9.98×10^{16}	9.48×10^{15}
Post Radiation Shot 7	1.37×10^{17}	9.48×10^{15}

From equation 39, information relating to flat band voltage can be extracted through differential analysis of the capacitance measurements in the form $1/\mathrm{C}^2$ with respect to change in voltage. When $1/\mathrm{C}^2$ is plotted against gate voltage, the change in the slope of $1/\mathrm{C}^2$ marks a transition point between carrier accumulation and depletion regions with the transition gate voltage denoted as the measured flat band voltage. A problem associated with this method is precisely measuring the transition point, so the second derivative is used to locate a more precise flat band voltage value. However, taking the second derivative of $1/\mathrm{C}^2$ results in noise that makes determining any single peak value difficult, so a 5-10 point Savitzky-Golay smoothing algorithm was applied which preserved peak value data while filtering random noise. The result of this method yielded several detectable peaks, with the largest peak amplitude assessed to mark the experimentally measured flat band voltage [30, 31]. Figures 24 - 26 show the experimental results of this method.

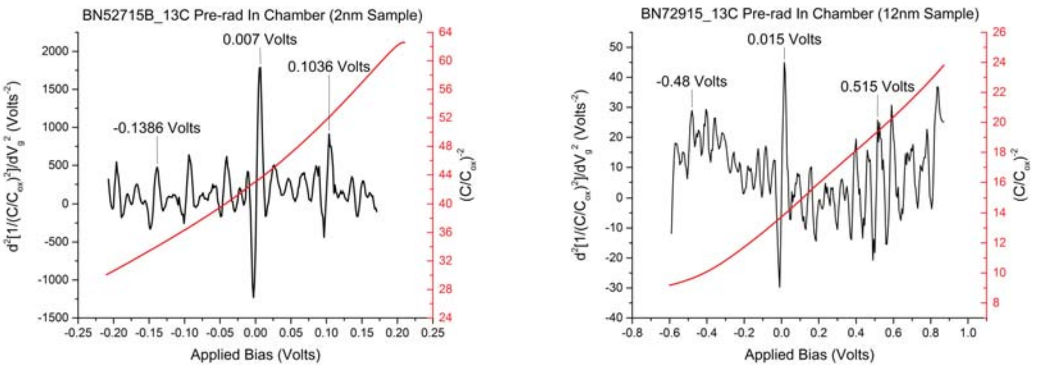

(a) 2 nm hBN sample pre-radiation (b) 12 nm hBN sample pre-radiation

Figure 24. Flat band voltage of pre-radiated device characterization using $d^2(1/C^2)/dV^2$ **method.**

Figure 24 shows the pre-irradiation experimentally derived flat band voltage from capacitance measurements for both the 2 nm and 12 nm samples. The right axis on all the graphs show the data for $1/(C/C_{ox})^2$ prior to differentiation. The capacitance measurement is divided by the insulator (oxide) capacitance which is especially important when the measured maximum oxide capacitance taken at accumulation varies. For all of the data presented, the theoretical oxide capacitance was used since the measured C-V curve only represents a portion of the total capacitance curve. This is because the measured maximum capacitance at accumulation bias is a factor of 3-5 lower than the theoretical capacitance as shown in Table 4. Furthermore, the applied gate voltage range was conservatively constrained to limit the induction of an electric field across the hBN insulator exceeding electrical breakdown material properties. Therefore all reported values stemming from capacitance measurements are relative rather than absolute.

Table 4. Capacitance comparison between theoretical expected values and measured values taken at accumulation from C-V measurements prior to ion irradiation.

Sample	Theoretical Capacitance (pF)	C-V Measured Capacitance (pF)
BN52715B_13C (2 nm)	869.3	158.5
BN72915_13C (12 nm)	578.5	191.3

The left axis in Figure 24 shows the second derivative of $1/(C/C_{ox})^2$ with the Savitzky-Golay smoothing algorithm applied. After smoothing the data, a single maximum amplitude peak is easily identifiable for both the 2 nm and 12 nm sample. Both peaks in the plotted data could potentially be the absolute measured flat band voltage as the theoretical calculated flat band voltage is 0.0052 volts shown in Figure 6. Several other peaks are labeled in the graphs as reference points to illustrate nearly undetectable flat band shifts in either sample as devices were irradiated.

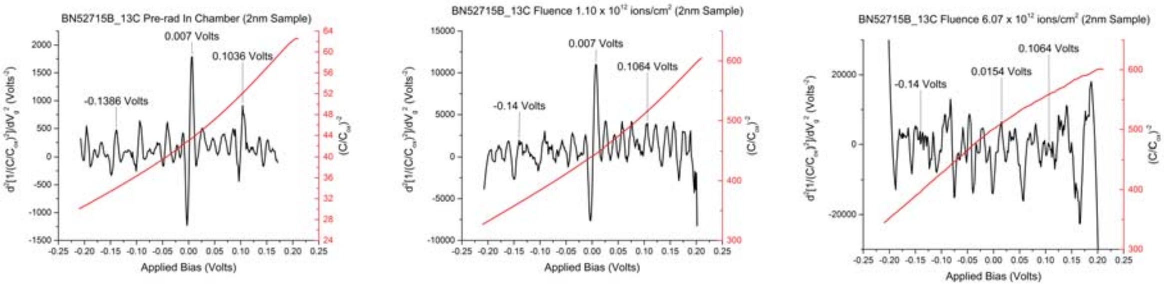

(a) At pump down (b) Prior to threshold fluence (c) After threshold fluence

Figure 25. 2 nm hBN flat band voltage characterization using $d^2(1/C^2)/dV^2$ method to show no flat band voltage shift and detect breakdown threshold fluence.

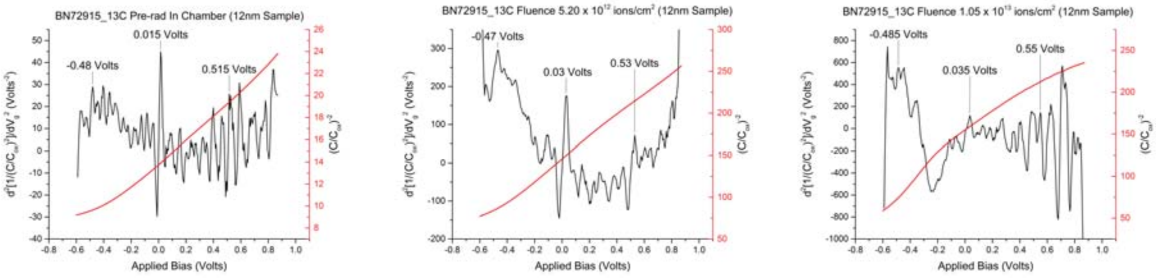

(a) At pump down (b) Prior to threshold fluence (c) After threshold fluence

Figure 26. 12 nm hBN flat band voltage characterization using $\mathrm{d}^2(1/\mathrm{C}^2)/\mathrm{dV}^2$ method to show no flat band voltage shift and detect breakdown threshold fluence.

Figures 25 and 26 correspond to the 2 nm and 12 nm samples respectively which compare measurements before, at, and after threshold fluence indicated by I-V measurements. In both samples, the maximum amplitude peak shown in the pre-irradiation measurements is still detectable, but other peaks are more pronounced in amplitude especially in regards to the 12 nm sample. This does not necessarily indicate a flat band voltage shift as the peaks were clearly visible and existed in the pre-irradiation measurements. However, the creation of interface traps at the hBN/silicon is likely since both the 2 nm and 12 nm samples show a slight elongation along the x-axis which is consistent with theory regarding elongation of C-V curves [2].

Another key finding from the $1/C^2$ second derivative method is the production of a repeatable signature delineating an operable device from one affected by breakdown. For both Figures 25 and 26, the sub figures “b” show the measured data at threshold fluence while the sub figures “c” show the data after total ion fluence surpassed threshold. After threshold fluence is surpassed, the most notable change that occurs is the disappearance of the peak located at near zero along the x-axis along with several other minor changes to other peak locations. The disappearance of the peak located near zero volts is due to the upward bowing of the $1/C^2$ line, thus altering the location of the inflection point. Therefore, this method was used to substantiate conclusions made about threshold ion fluence values of $1.10 \times 10^{12}$and 5.20×10^{12} ions/cm^2 for the 2 nm and 12 nm samples respectively. However, due to ion fluence step size it is only possible to conclude device breakdown and any associated phenomena occurred within a fluence range.

4.3.3 Impedance Analysis

Analysis of I-V and C-V measurements yielded the following results: (1) hBN resistance remained mostly unchanged until a total fluence of 1.10×10^{12} ions/cm^2 for the 2 nm sample and 5.20×10^{12} ions/cm^2 for the 12 nm sample were surpassed; (2) the total measured capacitance for both samples showed a decrease due to carrier removal in the depletion region prior to threshold ion fluence; and (3) almost no change in flat band voltage as a function of total ion fluence was noted. These results are important reference points used to aid in the analysis of impedance measurements and ensure the results are consistent with the solid state device impedance spectroscopy application caveats outlined by MacDonald[27].

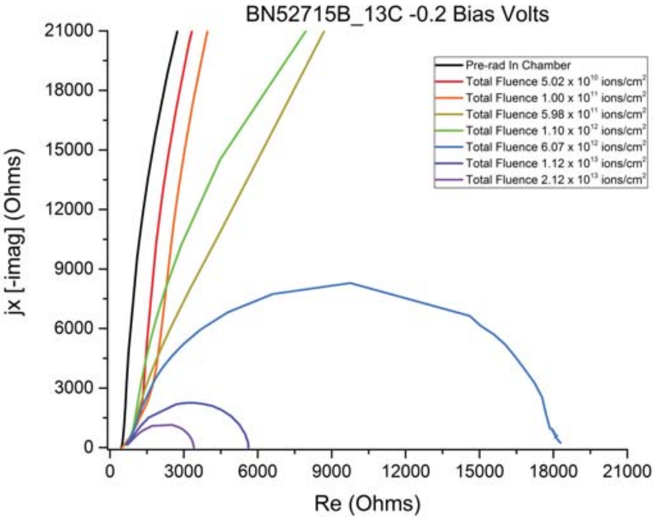

Figure 27. 2 nm hBN impedance measurement as a function of ion fluence.

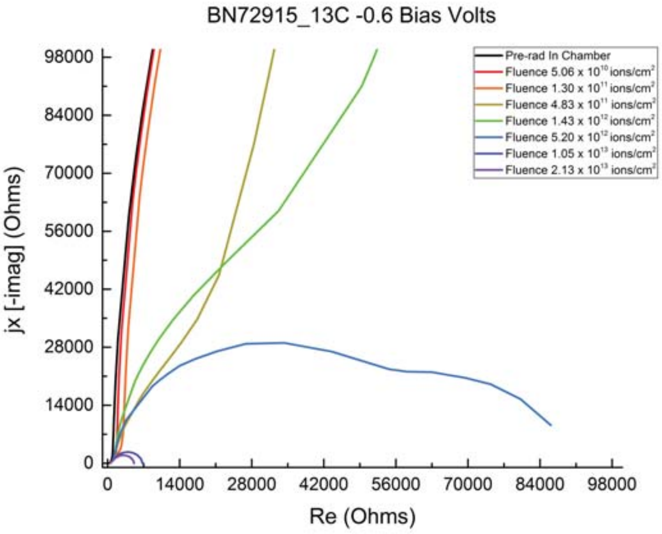

Figure 28. 12 nm hBN impedance measurement as a function of ion fluence.

Figures 27 and 28 show impedance measurements as a function of ion fluence while holding the gate bias fixed at -0.2 volts and -0.6 volts for the 2 nm and 12 nm samples respectively. The gate bias was fixed at -0.2 and -0.6 volts for the 2 nm and 12 nm sample respectively. Those values were selected because they were the maximum negative voltage applied, and the contribution of depletion region resistance to the overall device resistance is smallest under a negative bias compared to a positive bias for p-type silicon.

In both Figures 27 and 28, the plotted data associated with measurements taken at a lower total ion fluence begin as nearly vertical lines and then collapse to form decreasing concentric semicircles as total fluence increased. The decreasing concentric semicircles as total fluence increased indicated a simultaneous decrease in hBN resistance and capacitance. However, the vertical lines measured at a lower total fluence are a portion of the total impedance measurements and are assumed to form a larger semi-circle when the imaginary and real components of impedance are plotted. The frequency range limitation of the Keithley 4200 SCS prevents measurements below 1,000 Hz. Based upon impedance theory laid out in Section 2.4, if measurements could be taken below 1,000 Hz, the plotted data would continue in a positive direction along the x-axis, and a larger semi-circle would be expected. The inability to obtain frequency measurements below 1,000 Hz makes it difficult to extract absolute valued parameters for the resistance and capacitance of the hBN. However, the Complex Nonlinear Least Squares (CNLS) program developed by MacDonald is able to extrapolate a set of parameters for the hBN based on available measurements thus providing relative values to detect a change. The complete application of this method is discussed by MacDonald [32, 27], with the summary of results for the 2 nm and 12 nm samples shown in Figures 29 and 30.

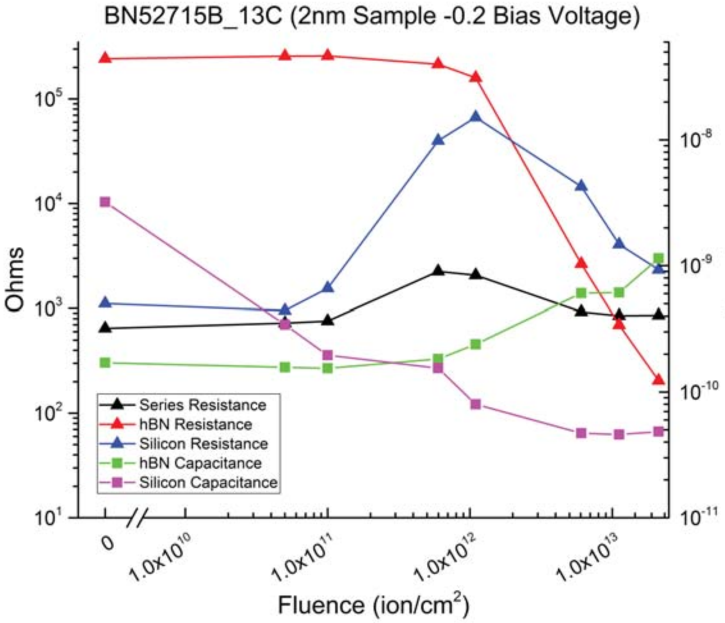

Figure 29. 2 nm discrete circuit node values derived through complex non-linear fitting of measured impedance data.

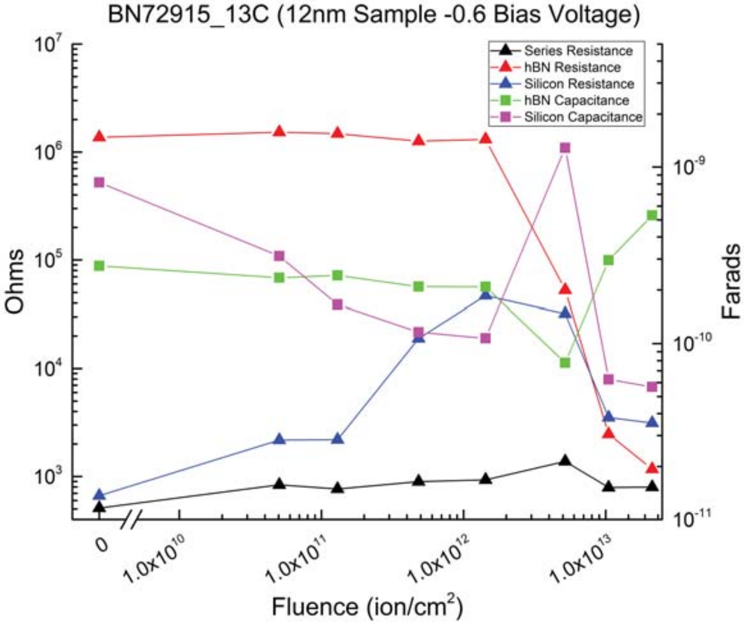

Figure 30. 12 nm discrete circuit node values derived through complex non-linear fitting of measured impedance data.

Figures 29 and 30 plot the CNLS solutions given the circuit diagram shown in Figure 17 and impedance measurements from Figures 27 and 28. The plots show both resistance and capacitance values overlaid with corresponding scales on the left and right y-axis. In both the 2 nm and 12 nm samples, the resistance and capacitance of the hBN insulator remain mostly constant, and the silicon capacitance decreases due to carrier removal until threshold ion fluence is reached. At threshold ion fluence, a decrease in the hBN resistance appears along with a decrease in the silicon junction resistance. The increase in silicon resistance is interpreted as being caused from displacement damage in the silicon due to ions that disrupt the uniform lattice structure in the silicon. The decrease in the hBN resistance is due to increased conduction through the insulator caused by some defect mechanism resultant from ion displacement damage. This phenomena will be further explained in later sections.

Other features noted in Figures 29 and 30 are changes in the hBN capacitance as a function of total fluence. That change in hBN capacitance is believed to be artificial due to the fact the thickness and material properties are unlikely to change when irradiated at fluence levels used for this experiment. Measured capacitance values are consistently lower than theoretical values as shown in Table 4, and this discrepancy is still unexplained. Furthermore, all capacitance measurements taken after the threshold fluence where device breakdown occurs are unreliable. Tables 5 and 6 below show the actual values for each data point in Figures 29 and 30 along with associated error and average total error.

Table 5. Impedance fitting CNLS results for 2 nm sample under gate bias voltage of -0.2 volts.

Total Ion Fluence	Series Resistance		hBN Resistance		Silicon Resistance		hBN Capacitance		Silicon Capacitance		Average Deviation
ions/cm^2	Ohms	Error +/-	Ohms	Error +/-	Ohms	Error +/-	pF	Error +/-	pF	Error +/-	
0	646	124	242380	711	1109	800	171	1.25	3200	1100	0.2531
5.02×10^{10}	726	323	256390	648	951	387	157	0.58	342	175	0.2738
1.00×10^{11}	759	171	257780	362	1550	216	155	0.33	196	66.5	0.1416
5.98×10^{11}	2243	319	214470	1889	39844	2112	183	3.86	155	5.24	0.0518
1.10×10^{12}	2060	325	159270	1646	66702	1824	240	6.04	79.9	1.60	0.0482
6.07×10^{12}	924	29	2642	87	14496	77	605	14.6	47.1	0.37	0.0204
1.12×10^{13}	851	21	670	49	4062	43	612	19.8	45.9	0.76	0.0309
2.13×10^{13}	859	22	205	52	2332	47	1143	94.6	48.5	1.50	0.0828

Table 6. Impedance fitting CNLS results for 12 nm sample under gate bias voltage of -0.6 volts.

Total Ion Fluence	Series Resistance		hBN Resistance		Silicon Resistance		hBN Capacitance		Silicon Capacitance		Average Deviation
ions/cm^2	Ohms	Error +/-	Ohms	Error +/-	Ohms	Error +/-	pF	Error +/-	pF	Error +/-	
0	511	30	1.369E6	139600	664	106	274	8.50	817	164	0.1104
5.06×10^{10}	838	49	1.523E6	199640	2178	275	235	78.6	312	10	0.1366
1.30×10^{11}	766	28	1.478E6	110560	2196	126	242	6.43	164	5.88	0.0464
4.83×10^{11}	897	42	1.260E6	161620	18998	1536	209	8.98	116	4.99	0.0684
1.43×10^{12}	931	39	1.310E6	195390	46980	3532	209	10	107	3.94	0.0701
5.20×10^{12}	1378	115	52835	440	32103	436	78	0.67	1285	42	0.0294
1.05×10^{13}	791	47	2466.3	115	3517	211	295	1.13	63	3.35	0.0445
2.13×10^{13}	799	41	1172.5	61	3134	130	532	33	57	2.56	0.0506

The parameter values and associated errors presented in the Table 5 and 6 were calculated using the CNLS program. The standard deviation shown in the far right columns represents the total average error of all data parameters calculated at a given total fluence. MacDonald points out that any average deviation greater than 0.03 yields a poorly fitted line to the measured impedance data [32]. In general, both the 2 nm and 12 nm samples fit deviation start out large and decrease as a function of fluence due to a decrease in the hBN resistance. As the hBN resistance decreases, smaller semicircles form because the measurement falls within the operating range of the Keithley 4200. As a result, at early fluence incomplete impedance measurements were taken which account for greater error in the CNLS fitting. At greater fluence, the average deviation decreases to within about a factor of 2 of the recommended deviation for a good fit. Therefore, comparing measured total capacitance from actual C-V measurements to the total calculated capacitance from the impedance fit determined parameters shown in the tables above was used to further validate the impedance fitted results. This comparison is shown below in Figures 31 and 32.

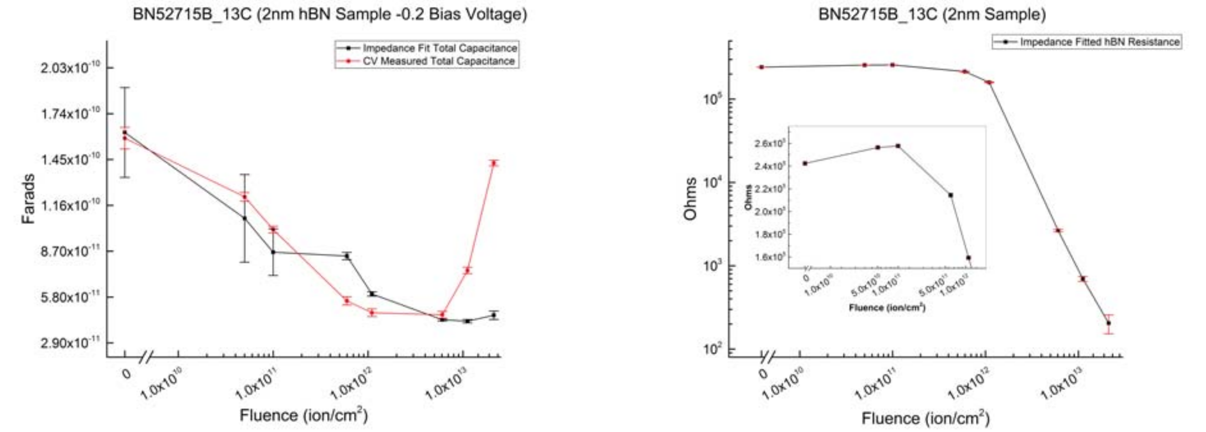

(a) 2 nm hBN impedance fitted total capacitance compared to measured total capacitance.

(b) 2 nm hBN relative resistance as a function of fluence determined through fitted impedance measurements.

Figure 31. Analysis of 2 nm hBN complex non-linear fitting to obtained 2 nm hBN relative resistance as a function of fluence.

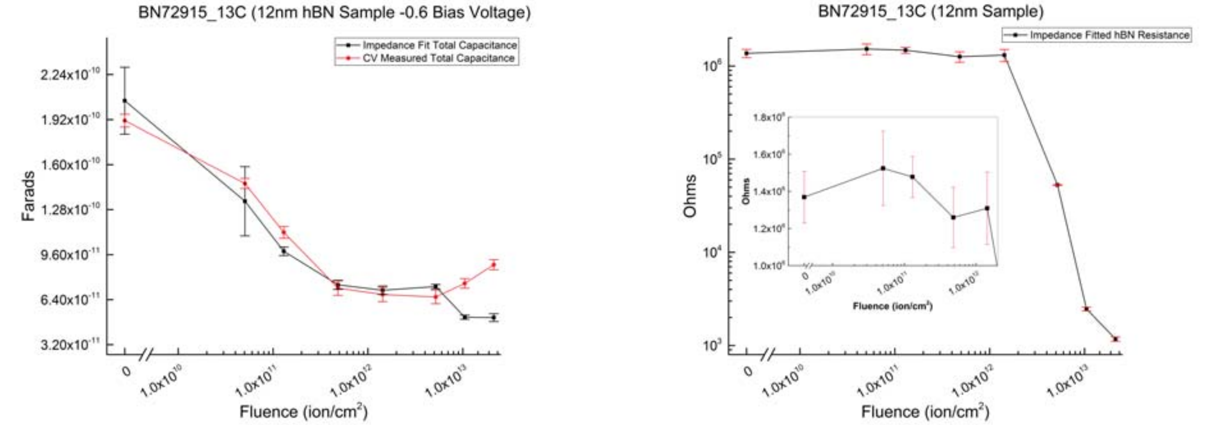

(a) 12 nm hBN impedance fitted total capacitance compared to measured total capacitance.

(b) 12 nm hBN relative resistance as a function of fluence determined through fitted impedance measurements.

Figure 32. Analysis of 12 nm hBN complex non-linear fitting to obtained 2 nm hBN relative resistance as a function of fluence.

In Figures 31a and 32a, the total capacitance obtained from C-V measurements and impedance fit determined parameters are compared. To determine the total capacitance extracted from the impedance fit parameters, equation 40 was used to calculate a total capacitance value from the combined hBN and silicon capacitance values shown in Tables 5 and 6. Overall, the impedance fitted and measured C-V total capacitance are in close agreement as shown by the error bars with the exception when the device undergoes breakdown. Therefore, it seems reasonable to accept the remaining impedance fitted parameters along with the relative approximations of the hBN resistance shown in Figures 31b and 32b.

$$C_{total} = \frac{C_{hBN}\,C_{Silicon}}{C_{hBN} + C_{Silicon}} \tag{40}$$

Once threshold fluence is surpassed, the hBN experiences a dramatic decrease in resistance by approximately two orders of magnitude from initial measured value based on experimental calculations. Any increase in total fluence beyond threshold, appears to result in a linear decrease in hBN resistance as a function of fluence. The defect mechanism is hypothesized to correlate to a threshold fluence/insulator thickness dependent formation of critical density of displacement defects which percolate to form permanent conduction paths through the insulator. While there may be intermediate stages of hBN resistance stability between initial measurements and permanent conduction path formation through the hBN occurring after threshold, intermittent stability in resistance was undetectable in this experiment due to the large step size of imparted ion fluence between measurements. This result is summarized in Figures 33 and 34.

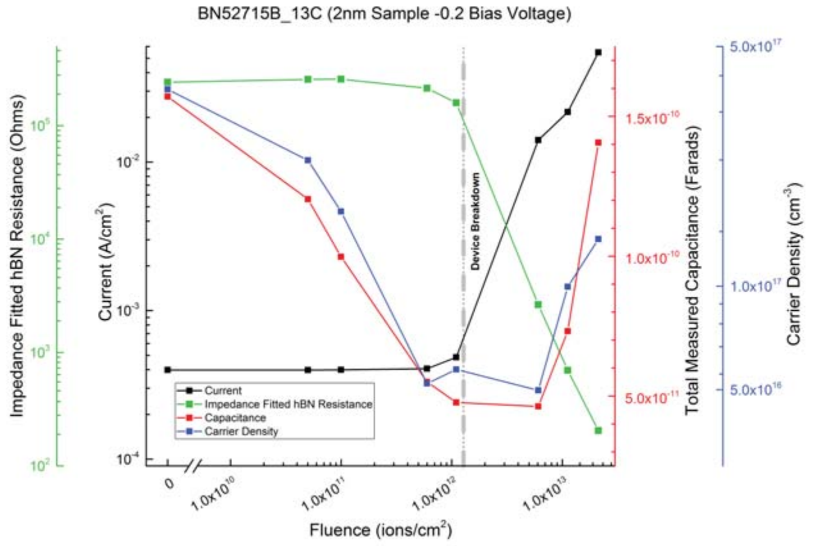

Figure 33. 2 nm hBN ion irradiation result summary indicating hBN resistance remains unaffected until a threshold fluence is achieved.

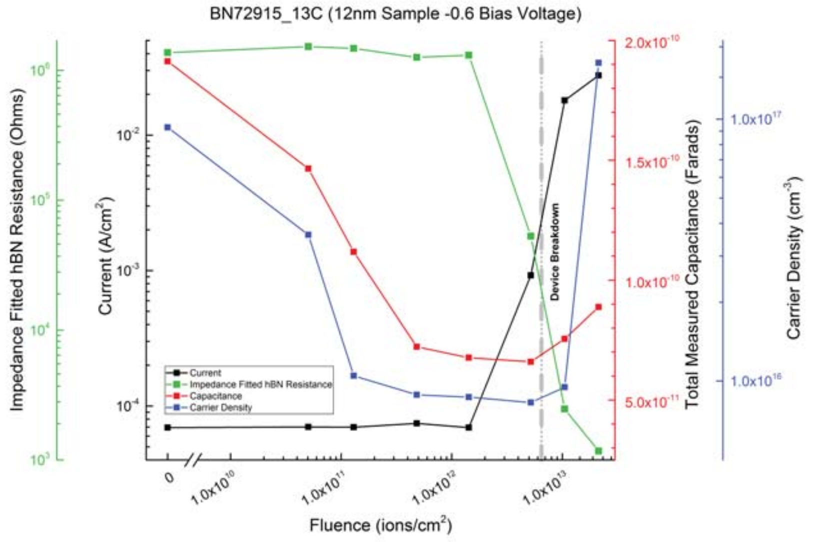

Figure 34. 2 nm hBN ion irradiation result summary indicating hBN resistance remains unaffected until a threshold fluence is achieved.

4.3.4 I-V Data Fitting to Determine Dominant Conduction Mechanisms

To determine the conduction mechanism associated with the dielectric breakdown, conduction mechanism functional fitting was used to determine an approximate solution. In general, this approximation method relied on fitting current density proportionality equations, shown in Table 1, to measured I-V data. Conduction mechanisms that showed the strongest correlation through a statistical R^2 fit were then highlighted as the most likely to account for overall current contribution through the hBN. The method is further described in section 3.4 with the calculated ideal electric field through the hBN for ion irradiated samples BN52715B_13C and BN72915_13C shown below in Figure 35.

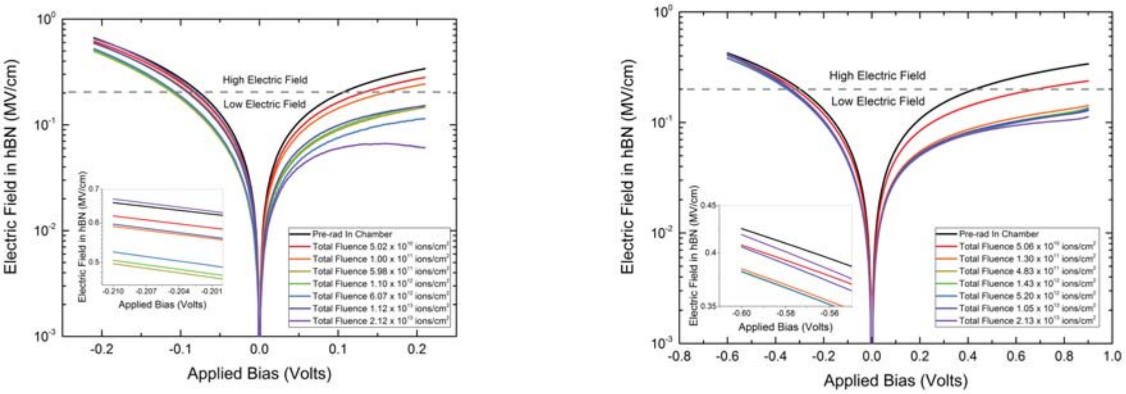

(a) Sample BN52715B_13C (2 nm hBN).

(b) Sample BN72915_13C (12 nm hBN).

Figure 35. Calculated ideal electric field in hBN. The inset graph for both samples provide an expanded view of electric field changes in the hBN under negative voltage to show minor changes.

Figure 35 shows the conversion of the applied gate voltage to the applied electric field across the hBN as a function of ion fluence for both the 2nm and 12nm samples. The variation in electric field across the hBN, calculated with equation 38, is due to the change in carrier concentration within the silicon that affects the surface potential (ψ_S) and change in series resistance as a function of radiation shown in Tables 5 and 6. Under a negative applied bias, the change in electric field across the hBN is relatively small in both the 2 nm and 12 nm samples. Regardless, a change in electric field as a function of fluence was accounted for in the fitting of conduction mechanism equations. The delineation between a high and low electric field was made by selecting an arbitrary electric field value of 0.2 MV/cm which was uniformly applied to both the 2 nm and 12 nm samples. Though imprecise, the value of 0.2 MV/cm was selected based on preliminary modeling of tunneling conduction where the theoretical fitted line showed a sharp departure from measured I-V data at approximately 0.2 MV/cm. This coincided with general theory where tunneling conduction current is primarily dominant at under higher electric fields [23].

Next, the calculated electric field across the hBN shown in Figure 35 was used to fit conduction mechanisms to experimentally measured I-V data. There are two sets of conduction fitting results for both the 2 nm and 12 nm which are labeled as a "General Functional Fit" and "Refined Functional Fit". The difference between the general and refined functional fit is related to the form of the equation used to model the conduction mechanism as shown above in Table 1. The primary purpose for comparison of the general and refined functional fit results is to justify the elimination of conduction mechanisms as a conduction mechanism equation used progresses from generalized form towards the actual theoretical equation form. The conduction mechanism fitting obtained from the general functional fit is shown in Figures 36 and 37.

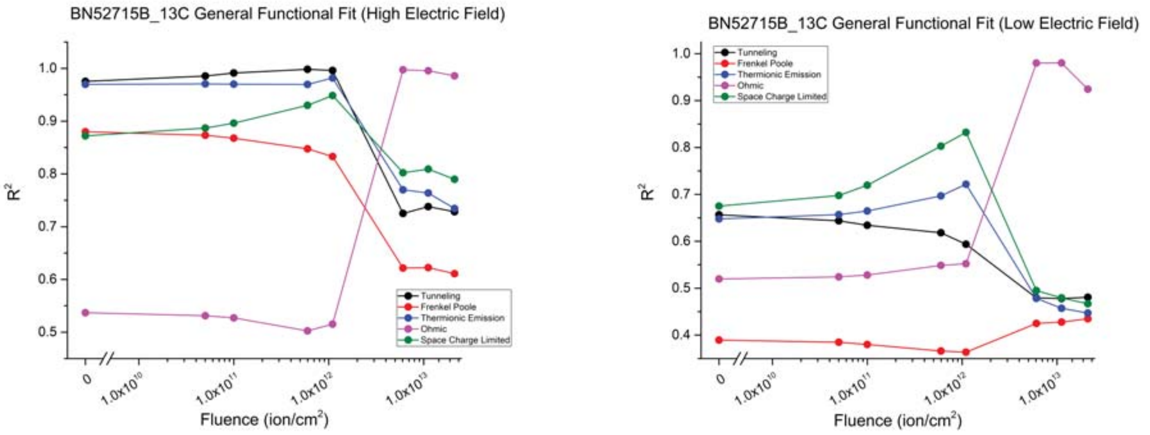

(a) 2 nm sample conduction mechanism general fitting sample under high electric field.

(b) 2 nm sample conduction mechanism general fitting sample under low electric field.

Figure 36. Conduction mechanism general functional fitting for 2 nm sample exposed to ion radiation.

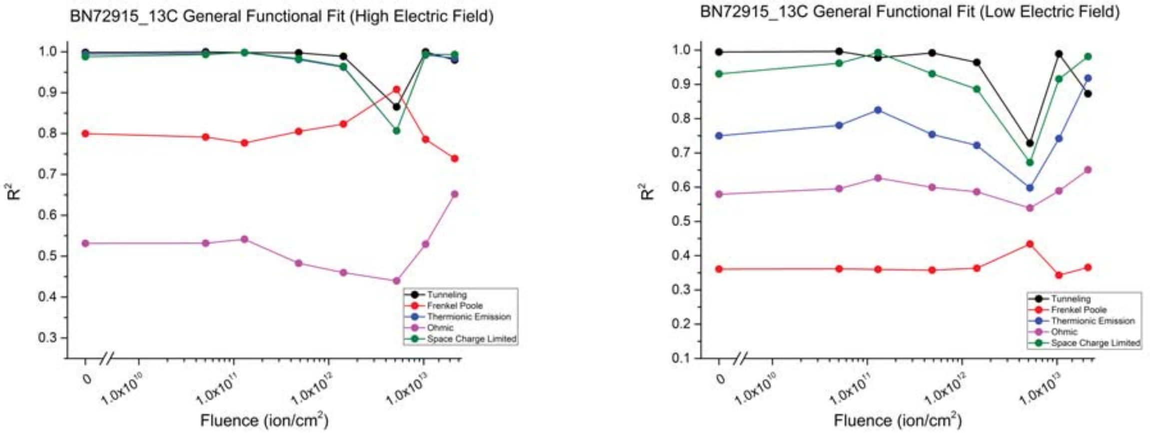

(a) 12 nm sample conduction mechanism general fitting sample under high electric field.

(b) 12 nm sample conduction mechanism general fitting sample under low electric field.

Figure 37. Conduction mechanism general functional fitting for 12 nm sample exposed to ion radiation.

Conduction mechanism fitting under high electric field across the hBN will be analyzed first which is shown in Figures 36a and 37a. Figures 36a and 37a show similarities in device electrical behavior prior to irradiation where neither show a strong dependance on ohmic conduction. Another similarity in the device electrical behavior is the good fit to two different conduction mechanisms that could individually or separately account for current flow through the hBN prior to irradiation. In the 2 nm sample, tunneling and thermionic emission appear to be possible dominant conduction mechanisms prior to irradiation. The 12 nm sample displayed the same dominant conduction mechanisms of tunneling and thermionic emission, but the space charge limited conduction mechanism also fit those data as well. Tunneling and thermionic emission are both electrode limited conduction mechanisms which were implied in section 1.4 to be the dominant current conduction processes prior to device irradiation.

Upon reaching threshold ion fluence, each sample shows a distinguishable change in conduction mechanism contribution order of dominance. The 2 nm sample appears to be dominated by ohmic conduction past threshold fluence whereas the 12 nm sample shows an increase in Frenkel-Poole conduction. The dominant ohmic conduction behavior shown in the 2 nm sample after threshold fluence is a reasonable result given the thinness of the hBN film. The conduction mechanisms associated with the 12 nm sample are more convoluted with no single mechanism governing current through the hBN after reaching threshold fluence.

Under a low electric field prior to irradiation, current conduction in both the 2 nm and 12 nm samples was best fit by space limited charge, tunneling, and thermionic emission mechanisms. This result obtained under a low electric field is similar to result obtained under a high electric field apart from variations in the measured goodness of fit (R^2). In contrast to the general fitting under a high electric field, Frenkel-Poole conduction mechanism fit was determined to have the lowest correlation to the measured data under a low electric field in both samples. Poor Frenkel-Poole conduction fit under low electric field is a well established phenomena [23] that help to validate the conduction mechanism fit algorithm and results presented.

Following the general functional fit of conduction mechanisms to measured I-V data, a refined function fit was implemented. The refinement to the conduction mechanism fit used equations listed in Table 1, along with specific device variable values shown in Table 7. The specific device variables shown in Table 7 were held constant with explanation of variable values developed in sections 1.1.1, 2.1, and 2.3.1. The conduction mechanism fitting obtained from the refined functional fit is shown in Figures 38 and 39.

Table 7. Device and hBN material variable values used for conduction mechanism refined functional fitting.

Variable	Value
Dielectric Permittivity (ϵ_i)	$4\,\epsilon_o$
Dielectric Potential Barrier (ϕ_B)	2.069 eV
Effective Electron Mass ($m*$)	0.26

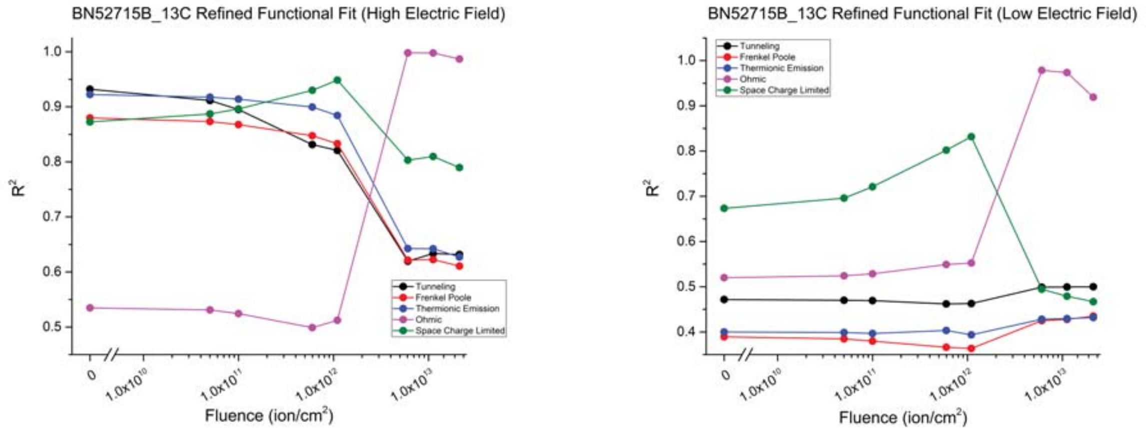

(a) 2 nm sample conduction mechanism refined fitting sample under high electric field.

(b) 2 nm sample conduction mechanism refined fitting sample under low electric field.

Figure 38. Conduction mechanism refined functional fitting for 2 nm sample exposed to ion radiation.

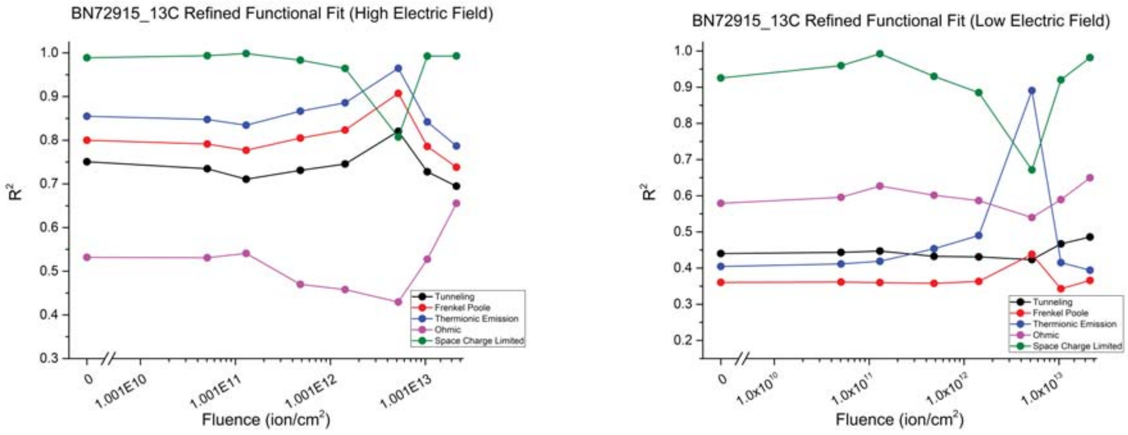

(a) 12 nm sample conduction mechanism refined fitting sample under high electric field.

(b) 12 nm sample conduction mechanism refined fitting sample under low electric field.

Figure 39. Conduction mechanism refined functional fitting for 12 nm sample exposed to ion radiation.

Compared to the general fitting results shown in Figures 36 and 37, the refined fitting results shown in Figures 38 and 39 possess many of the same similarities. One of the differences between the general and refined conduction fitting is the emergence of the space charge limited conduction mechanisms being the most dominant in the 12 nm sample under high electric field and in both samples under a low electric field. Given the assumed polycrystalline structure of the hBN discussed in section 1.1.2, the above result is plausible because other studies have reported the dominance of space charge limited conduction within materials such as polycrystalline LaO$_3$[23]. Additionally, the refined fitting results show the potential to deconvolve and potentially identify the one or two dominate conduction mechanisms as the the full theoretical conduction mechanism equations are used to the fit the experimental I-V data. This is evident when comparing Figures 37a and 39a.

The problem with the refined functional fitting results discussed above is there are a wide range of possible variable value combinations that could provide an equal fitted line to the experimental data. Because the hBN samples used in this study are produced through a research fabrication process, there is limited data on these kind of devices to compare the above fitted results against. The conduction mechanism refined functional fit used in this study did not attempt to achieve an optimized fit through a variable parameterization study. Even if the a parameterization study was conducted within the present study, many of the conduction mechanism equations shown throughout this document contain multiple unknown variables within a single equation; preventing a particular solution from being reached.

4.3.5 Summary of Ion Irradiation Results

In situ I-V, C-V and Impedance measurements were collected from a single 2 nm and 12 nm hBN sample. Information from the three different measurements was then used as cross validation to draw the following conclusions: (1) hBN resistance remained mostly unchanged until a total fluence of $1.10 \times 10^{12}\,\text{ions/cm}^2$ for the 2 nm sample and $5.20 \times 10^{12}\,\text{ions/cm}^2$ for the 12 nm sample were surpassed; (2) prior to threshold fluence, the measured hBN resistance of the 2 nm sample was approximated at $2.5 \times 10^5\,\Omega$ or $6.13 \times 10^8\,\Omega - cm$, and the measured hBN resistance of the 12 nm sample was approximated at $1.4 \times 10^6\,\Omega$ or $2.22 \times 10^9\,\Omega - cm$ (3) the total measured capacitance for both samples showed a decrease due to carrier removal in the depletion region prior to threshold ion fluence; and (4) there was no detectable lateral shift or elongation in C-V curve as a function of ion fluence which potentially indicates a negligible flat band voltage shift.

Finally, an attempt to characterize the cause of the hard dielectric breakdown after threshold fluence was made through line fitting of the experimental I-V data. Established theoretical conduction mechanism equations were fitted against collected I-V data to determine individual current contributions of conduction mechanisms and how those current contributions changed at the threshold fluence marking hard dielectric breakdown. Prior to irradiation, conduction mechanism fitting indicated tunneling and thermionic emission in the 2 nm sample and space charge limited conduction in the 12 nm sample under a high electric field, and space charge limited conduction under a low electric field for both samples. At threshold fluence, the contributions to current appeared to occur from primarily from ohmic conduction within the 2 nm sample; while the 12 nm sample showed an increase in current through a combination in thermionic emission and Frenkel-Poole conduction. Due to the limitations discussed in the previous section, the conduction fitting results are inconclusive, but the observations outlined above appear reasonable when compared to other reported studies and accepted theory. Therefore, it remains plausible that the onset of hard dielectric breakdown corresponds to an increase in bulk limited current conduction mediated by displacement defects.

Based on theses results, a potential hypothesis is threshold fluence corresponds to thickness dependent critical density of displacement defects. Furthermore, preliminary measurements indicate hBN is relatively radiation harden as the MIS devices irradiated with 4.5 MeV silicon ions showed minimal increased current flow until a threshold fluence was reached. This threshold fluence is converted into a proton fluence shown in Table 8 with the calculation procedure shown in appendix A.

Table 8. 4.5 MeV silicon ion fluence conversion to a 1 MeV proton equivalent damage ion fluence.

hBN Thickness (nm)	4.5 MeV silicon ion fluence ions/cm^2	1 MeV proton equivalent damage ion fluence ions/cm^2 (hBN)	1 MeV proton equivalent damage ion fluence ions/cm^2 (Si)
2	1.10×10^{12}	2.96×10^{14}	3.11×10^{14}
12	5.20×10^{12}	1.88×10^{15}	1.97×10^{15}

4.4 Device Response to Gamma Irradiation

The overall result from the analysis of gamma irradiation indicated an increase in measured resistance after a gamma dose of 3.1 Mrad. The measured increase in hBN resistance post gamma radiation is supported by I-V measurements which show a general decrease in measured current. C-V analysis indicated no significant flat band voltage shift as well as no significant change in hole concentration within the silicon. Although more pronounced, the increase in measured hBN resistance following gamma irradiation is similar to early ion radiation measurements which also show a slight increase in hBN resistance prior to ion threshold fluence.

4.4.1 I-V and C-V Analysis

Figures 40 and 41 show I-V and C-V data for a 2 nm and 12 nm device before and after gamma irradiation. The devices shown had pre-rad characteristics that closely matched the two devices exposed to ion radiation. I-V, C-V, and impedance data for all other devices is plotted in appendix C. I-V analysis of the 2 nm and 12 nm samples showed similar electrical responses as a function of gamma dose with measurements shown in Figures 40a and 41a. After gamma irradiation, both the 2 nm and 12 nm devices exhibited a general decrease in current in both positive and negative bias regions. The decrease in current is different from I-V measurements obtained from ion irradiation. Device response to ion radiation showed minimal current fluctuations under negative bias and broad increases in current under positive bias as function of increasing ion fluence. In contrast, device response to gamma irradiation showed broad decrease in current under both positive and negative bias. Furthermore, an increase in the measured hBN resistance, inferred from impedance spectroscopy, was noted following gamma irradiation which will be discussed in the next section. This phenomenon was evident in nearly all of the gamma irradiated samples.

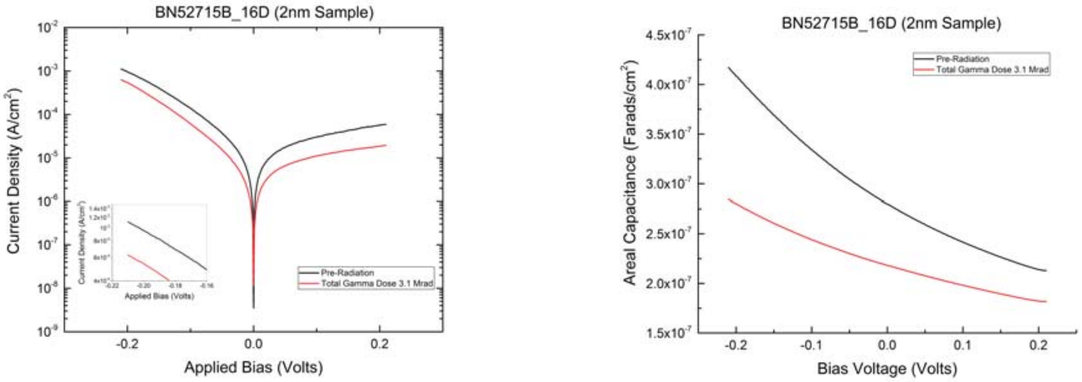

(a) Current density (b) Areal capacitance

Figure 40. Sample BN52715B_16D current density and areal capacitance as a function of gamma dose and voltage. The inset graph in sub-figure (a) provides an expanded view of I-V measurements under negative voltage to show minor changes.

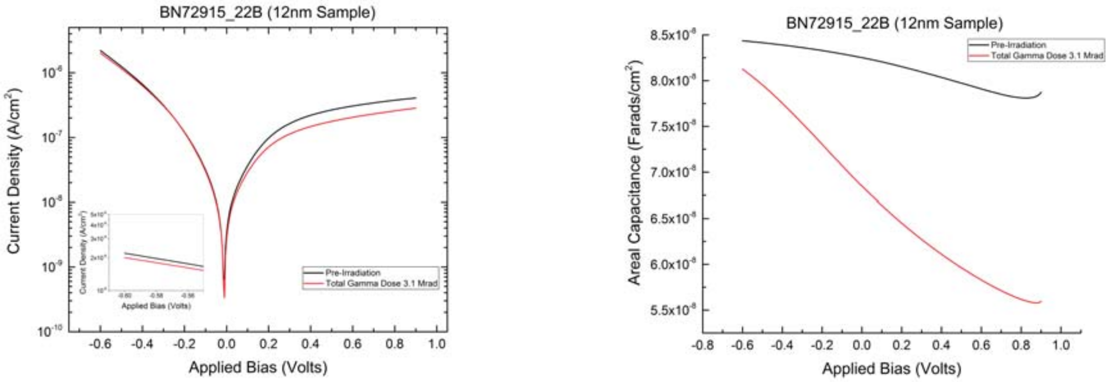

(a) Current density (b) Areal capacitance

Figure 41. Sample BN72915_22B current density and areal capacitance as a function of gamma dose and voltage. The inset graph in sub-figure (a) provides an expanded view of I-V measurements under negative voltage to show minor changes.

The corresponding C-V measurements for the 2 nm and 12 nm samples are shown in Figures 40b and 41b. Unlike the C-V measurements taken for the ion irradiated samples which showed a uniform decrease in capacitance as a function of fluence, the gamma irradiated devices showed a non-uniform decrease in capacitance. The non-uniform decrease in capacitance could not be explained through carrier removal or flat band voltage shift. The silicon hole concentration of all samples was determined through applying equation 39 to the C-V measurements collected before and after gamma radiation with result shown in Tables 9 and 10. Although the 12 nm samples showed larger fluctuations in hole concentration following gamma irradiation, the change in silicon hole concentration is relatively small and unlikely to account for the changes in capacitance or current density.

Table 9. 2 nm experimentally calculated silicon hole concentration as a function of gamma fluence.

Sample	Pre-Irradiation ($1/cm^3$)	Post Irradiation ($1/cm^3$)
BN52715B_16B	3.59×10^{17}	3.43×10^{17}
BN52715B_16C	3.38×10^{17}	3.71×10^{17}
BN52715B_16D	2.96×10^{17}	2.88×10^{17}
BN52715B_16E	2.34×10^{17}	2.40×10^{17}
BN52715B_16F	2.17×10^{17}	2.12×10^{17}

Table 10. 12 nm experimentally calculated silicon hole concentration as a function of gamma fluence.

Sample	Pre-Radiation ($1/cm^3$)	Post Radiation ($1/cm^3$)
BN72915_10B	3.03×10^{17}	3.16×10^{17}
BN72915_22B	5.30×10^{17}	9.73×10^{16}
BN72915_22D	3.89×10^{17}	5.03×10^{17}

Figures 42 and 43 show the differential analysis of the capacitance measurements in the form $1/C^2$ to determine experimental flat band voltage. A detailed description of this method is provided above in section 4.3. Comparing pre and post gamma radiation second derivative plots of $1/C^2$, several distinguishable peaks are visible with the largest occurring at 0.007 volts for the 2 nm sample and 0.02 volts for the 12 nm sample. These peaks most likely correspond to the experimentally calculated flat band voltage, and shift slightly following irradiation. However, the difference between pre and post radiation flat band voltage matches the voltage sweep step size (ΔV) for both the 2 nm and 12 nm samples. As an example, the 12 nm sample showed a voltage shift of 0.005 volts ($0.025\text{V} - 0.02\text{V} = 0.005\text{V} = \text{V}_{\text{FB Shift}}$) which is exactly equal to the voltage sweep step size ($\Delta\text{V} = 0.005\text{V}$). Therefore, a very small flat band voltage shift may be present, but the discretized voltage steps used are not small enough to precisely measure the change.

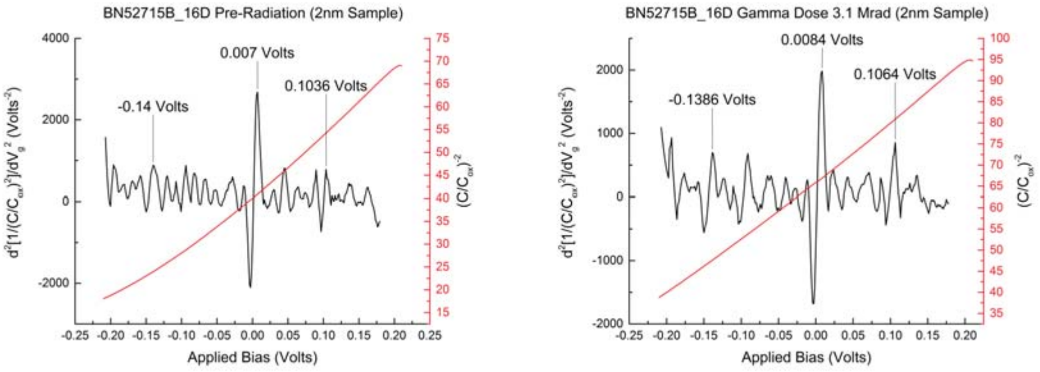

(a) Pre-Radiation (b) Post Radiation

Figure 42. Sample BN52715B_16D hBN flat band voltage characterization using $d^2(1/C^2)/dV^2$ method to detect flat band voltage shift and dielectric breakdown.

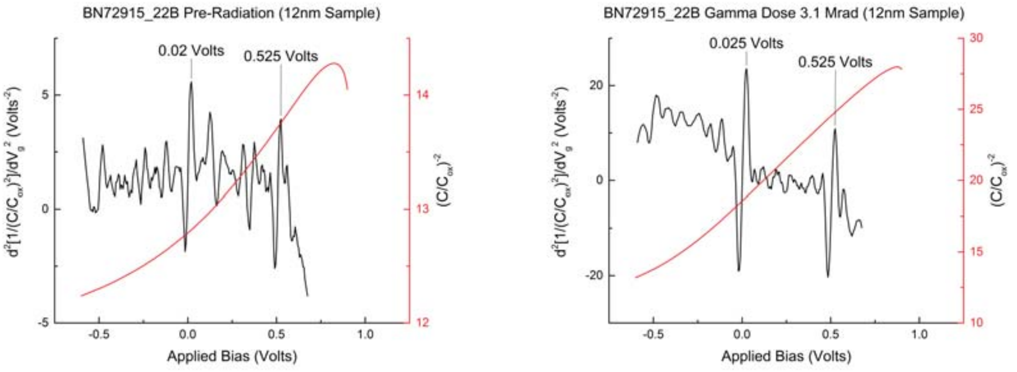

(a) Pre-Radiation (b) Post Radiation

Figure 43. Sample BN72915_22B hBN flat band voltage characterization using $d^2(1/C^2)/dV^2$ method to detect flat band voltage shift and dielectric breakdown.

4.4.2 Impedance Analysis

Impedance analysis of the gamma irradiated samples showed a relatively small increase in hBN resistance compared to the initial measurements. This phenomenon correlates to the broad decrease in current previously shown in Figures 40a and 41a. The impedance measurements as a function of gamma dose for the 2 nm and 12 nm samples are shown in Figure 44. From the impedance measurements, CNLS fitting was used to determine values for the equivalent circuit shown in Figure 17 with results reported in Tables 11 and 12. The key finding from the impedance measurements is that the resistance of the hBN showed a slight increase following gamma irradiation.

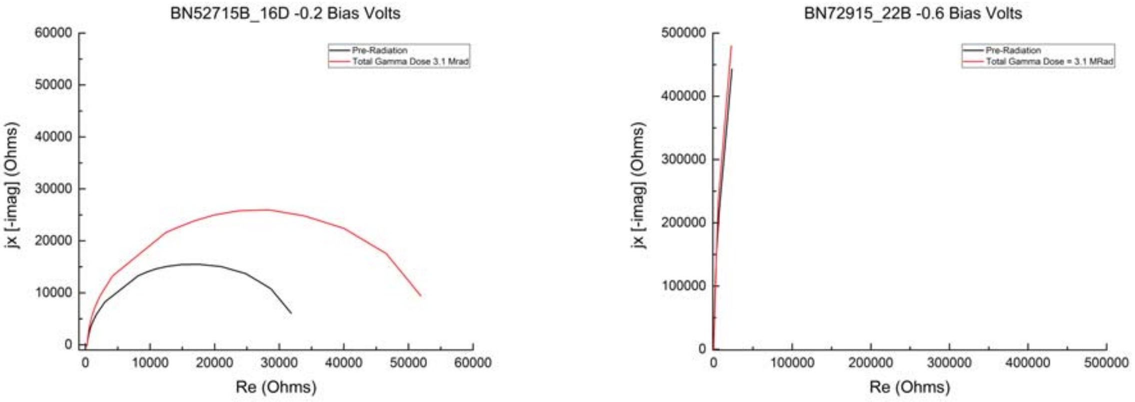

(a) Sample BN52715B_16D

(b) Sample BN72915_22B

Figure 44. Sample BN52715B_16D and BN72915_22B plotted impedance as a function of gamma dose.

Table 11. Impedance fitting CNLS results for 2 nm sample under gate bias voltage of -0.2 volts.

Total Gamma Dose	Series Resistance		hBN Resistance		Silicon Resistance		hBN Capacitance		Silicon Capacitance		Average Deviation
Mrad	Ohms	Error +/-	Ohms	Error +/-	Ohms	Error +/-	pF	Error +/-	pF	Error +/-	
0	305	19	27073	1253	5617	1281	1248	8.66	2612	345	0.107
3.1	286	27	47631	2452	5467	2493	675	5.01	2759	778	0.192

Table 12. Impedance fitting CNLS results for 12 nm sample under gate bias voltage of -0.6 volts.

Total Gamma Dose	Series Resistance		hBN Resistance		Silicon Resistance		hBN Capacitance		Silicon Capacitance		Average Deviation
Mrad	Ohms	Error +/-	Ohms	Error +/-	Ohms	Error +/-	pF	Error +/-	pF	Error +/-	
0	164	73	8.69×10^6	144100	641	133	360	0.23	7322	3324	0.225
3.1	111	67	1.044×10^7	550900	415	284	335	0.63	2185	4343	0.666

4.4.3 I-V Data Fitting to Determine Dominant Conduction Mechanisms

The same fitting technique discussed in sections 3.4 and 4.3.4 were applied to experimental I-V measurements for samples exposed to gamma radiation. The results for samples BN52715B_16D and BN72915_22B are shown below in tables 13 and 14.

Table 13. Conduction mechanism refined functional fitting for sample BN52715B_16D (2 nm) exposed to gamma radiation. Values within the tables represent the goodness of fit (R^2).

Conduction Mechanism	Pre-Radiation (Gamma Dose 0 Mrad) Refined Functional Fit		Post Radiation (Gamma Dose 3.1 Mrad) Refined Functional Fit	
	High Electric Field	Low Electric Field	High Electric Field	Low Electric Field
Tunneling	0.8813	0.4890	0.9144	0.4840
Frenkel Poole	0.7589	0.4042	0.7881	0.3994
Thermionic Emission	0.7902	0.4049	0.8219	0.4003
Ohmic	0.6688	0.5508	0.6209	0.5356
Space Charge Limited	0.9935	0.8244	0.9707	0.9471

Table 14. Conduction mechanism refined functional fitting for sample BN72915_22B (12 nm) exposed to gamma radiation. Values within the tables represent the goodness of fit (R^2).

Conduction Mechanism	Pre-radiation (Gamma Dose 0 Mrad) Refined Functional Fit		Post radiation (Gamma Dose 3.1 Mrad) Refined Functional Fit	
	High Electric Field	Low Electric Field	High Electric Field	Low Electric Field
Tunneling	0.8291	0.4363	0.7933	0.4332
Frenkel Poole	0.8683	0.3767	0.8471	0.3733
Thermionic Emission	0.9224	0.4323	0.9041	0.4281
Ohmic	0.4814	0.5480	0.4717	0.5686
Space Charge Limited	0.9069	0.7879	0.9400	0.8812

Prior to irradiation, conduction mechanism fitting indicated dominance of space charge limited in the 2 nm sample and thermionic emission in the 12 nm sample under a high electric field, and space charge limited conduction under a low electric field for both samples. This result is dissimilar to conduction mechanism fitting result obtained from the ion irradiated samples under a high electric field. For the un-irradiated ion 2 nm sample, tunneling and thermionic emission appeared more dominant in the un-irradiated ion sample compared to the sample used for gamma irradiation. For the un-irradiated ion 12 nm sample, space charge limited conduction appeared more dominant in the un-irradiated ion sample. Following irradiation with a total gamma dose of 3.1 Mrad(Si), both the 2 nm and 12 nm showed space charge limited as the dominant conduction mechanism under a low and high electric field.

Overall, the gamma irradiation conduction mechanism results by themselves did show a close correlation of several conduction mechanisms that contribute to the total current flow through the hBN; demonstrating the potential to deconvolve the most dominate conduction process through the hBN. Also, the minimal correlation of ohmic conduction to experimental measurements does support the finding that the hBN resistance increases following gamma irradiation. However, the difference in dominant conduction mechanism results between identical un-irradiated samples is an issue. This variability could stem from measurement error or incompatible application of ideal theory to describe experimental results. Another explanation is the variability in the MIS devices used in this study discussed in section 1.1.2, highlighting the need for a larger population of samples to obtain statistical evidence. Furthermore, the issue with variability between sample measurements becomes compounded when only a pre-radiation and post-radiation measurement was collected on the gamma irradiated samples compared to the multiple in situ measurements collected on the ion irradiated samples.

4.4.4 Summary of Gamma Irradiation Results

I-V, C-V and Impedance in situ measurements were collected from several 2 nm and 12 nm hBN sample. Information from the three different measurements were then used as cross validation to draw the following conclusions: (1) following a gamma dose of 3.1Mrad(Si), both the 2 nm and 12 nm devices exhibited a general decrease in current under both positive and negative bias regions with no evidence of a hard dielectric breakdown; (2) prior to gamma irradiation, the measured hBN resistance of the 2 nm sample was approximated at $27,000\,\Omega$ or $2.65 \times 10^{8}\,\Omega - cm$, and the measured hBN resistance of the 12 nm sample was approximated at $8.69 \times 10^{6}\,\Omega$ or $3.21 \times 10^{10}\,\Omega - cm$ (3) the total measured capacitance for both samples showed a decrease; and (4) there was no detectable lateral shift or elongation in C-V curve as a function of ion fluence which potentially indicates a negligible flat band voltage shift.

Finally, established theoretical conduction mechanism equations were fitted against collected I-V data to determine individual current contributions of conduction mechanisms and how those current contributions changed as a function of gamma dose. Prior to irradiation, conduction mechanism fitting indicated dominance of space charge limited in the 2 nm sample and thermionic emission in the 12 nm sample under a high electric field, and space charge limited conduction under a low electric field for both samples. Following post irradiation with a total gamma dose of 3.1 Mrad(Si), both the 2 nm and 12 nm showed space charge limited as the dominant conduction mechanism under a low and high electric field. Compared with the ion irradiated conduction mechanism fitting results, the gamma conduction mechanism fitting results further highlight their speculative nature with the need for further refinement and larger sample size to produce a better result.

V. Conclusions

5.1 Conclusions of Research

The hBN thin films produced for this study were found to be relatively radiation hard to both displacement damage and total ionizing dose. MIS devices irradiated with 4.5 MeV silicon ions showed no significant resistivity decrease to a threshold fluence of 1×10^{12} ions/cm^2 for the 2 nm sample and 5×10^{12} ions/cm^2 for the 12 nm sample. These 4.5 MeV silicon ion fluences correspond to displacement damage equivalent 1 MeV proton fluences of 3×10^{14} and 2×10^{15} protons/cm^2, respectively. Ion irradiation threshold fluence appeared to correspond to a thickness dependent critical density of displacement defects because the ion fluence needed to cause hard dielectric breakdown was approximately inversely proportional to the thickness of the hBN film. There was no evidence of a radiation induced C-V shift associated with the presence of persistent trapped charge. However, given the level of leakage current exhibited by the devices in this study, the effects of persistent trapped charge may not have been discernible.

An attempt was made to identify conduction mechanisms contributing to increased current density across the hBN dielectric. Conduction mechanism fitting of the I-V data showed some evidence of a transition from electrode limited conduction mechanisms to bulk limited conduction mechanisms at threshold ion fluence in both the 2 nm and 12 nm hBN samples. However, pre-irradiation conduction mechanism fitting results were not consistent across a broader selection of samples. Due to the limitations presented, the conduction fitting results are inconclusive, but the observations outlined in this study appear reasonable when compared to other reported studies and accepted theory. Therefore, it remains plausible that the onset of hard dielectric breakdown corresponds to an increase in bulk limited current conduction mediated by displacement defects, but the I-V fitting results presented in this study are tentative pending further investigation.

5.2 Future Work

Because the hBN samples used in this study are produced through a research fabrication process, there is limited data to compare the I-V fitting results against. Temperature dependent I-V measurements should be taken and compared to the room temperature conduction mechanism fitting results discussed in this document. The temperature dependence of the considered conduction mechanisms is generally well understood [23].

Furthermore, additional refinements to the conduction mechanism fitting algorithm used in this study are required. This study did not attempt to achieve a final optimized fit through a variable parameterization study. Many of the conduction mechanism equations shown throughout this document contain multiple unknown variables within a single equation; thereby, preventing a particular solution from being reached. To reduce the number of unknown variables, it is necessary to identify the hBN material properties that could be measured with resources and time available. Some measured hBN material properties that would be useful in improving the results contained within this study include hBN permittivity, electron mobility, and average electron activation energy from trap sites within the hBN. Another useful measurement would be to experimentally map the actual band structure diagram of the interface between the hBN and metal contact as well as the interface between the hBN and substrate material.

Appendix A. SRIM Silicon Ion to Proton Conversion Procedure

The general program setup and procedures for how to run the Stopping and Range of Ions in Matter (SRIM) program is outlined in the publication by James Ziegler [33]. The purpose of this appendix is to discuss in detail how to convert a 4.5 MeV silicon ion fluence to a 1 MeV proton fluence. The first step is to conduct a general SRIM simulation to calculate the ion deposition depth and volumetric displacement damage which shown in Figure 45.

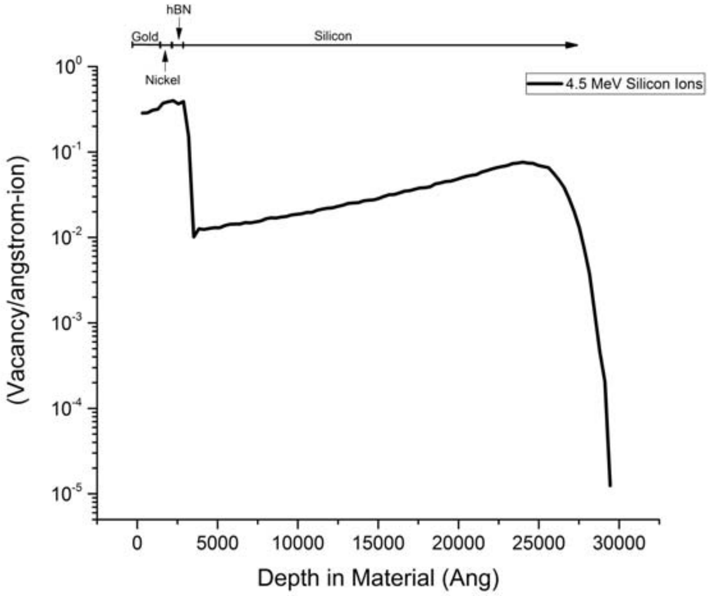

Figure 45. SRIM determined displacement per ion for 4.5 MeV silicon ions across a 12 nm hBN device. The MIS device modeled in SRIM consisted of layers of gold (300 nm in depth), nickel (20 nm in depth), hBN (12 nm in depth), and silicon (3168 nm in depth) shown left to right in the graph.

Figure 45 represents the the typical SRIM output of total damage events shown along the y axis as a function of depth in the material. Furthermore, Figure 45 is representative of both a 2 nm and 12 nm hBN device because the addition of 10 nm of hBN to the overall device material depth has negligible impact on the location of the Bragg peak. From Figure 45, the volumetric displacement can be determined through equation 41. The variable F represents the actual total experimental fluence imparted through the device, V_{ion} is the number of vacancies per angstrom-ion obtained from Figure 45, and V_{vol} is the total number of vacancies per unit volume for a given fluence. The fluence values used in the proton conversion are 1.10×10^{12} and 5.20×10^{12} ions/cm^2 which correspond the threshold fluence in the 2 nm and 12 nm hBN sample respectively.

$$F\left(\frac{\text{ions}}{\text{cm}^2}\right) \times V_{ion}\left(\frac{\text{Vacancy}}{\text{Angstrom} - \text{ion}}\right) \times 10^8\left(\frac{\text{Angstrom}}{\text{cm}}\right) = V_{vol}\left(\frac{\text{Vacancy}}{\text{cm}^3}\right) \quad (41)$$

Next, two more SRIM calculations are conducted for both the 2 nm and 12 nm hBN samples, limiting the region of interest to cover only the nickel/hBN/silicon layer interfaces. This is done to increase the number of “bins” allocated to the hBN layer and reduce the amount of error through increased sampling. The result of this SRIM calculation is shown in Figure 46.

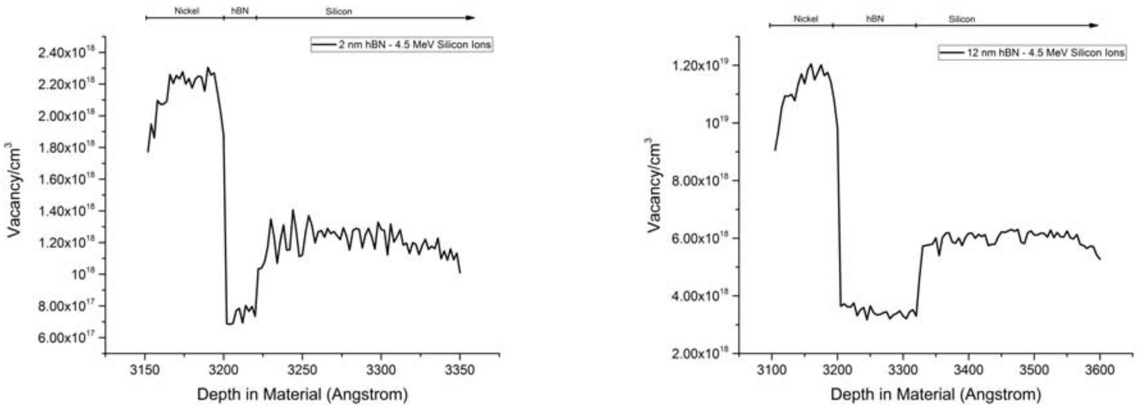

(a) 2 nm hBN sample.

(b) 12 nm hBN sample.

Figure 46. SRIM determined volumetric displacement for 4.5 MeV silicon ions across a 2 nm and 12 nm hBN device. The MIS device modeled in SRIM consisted of layers of gold (300 nm in depth), nickel (20 nm in depth), hBN (2 nm or 12 nm in depth), and silicon (3168 nm in depth) shown left to right in the graph. 25,000 particles were run in SRIM using monolayer collision steps to generate these plots

From Figure 46, an average volumetric displacement value is determine through taking the mean of values confined to a particular material type and the limited region of interest used in the SRIM calculation. The average is used due to avoid selecting a single point due to the noise within the calculations. The average volumetric displacement calculation is shown in Figure 47 with tabulated values shown in Table 15.

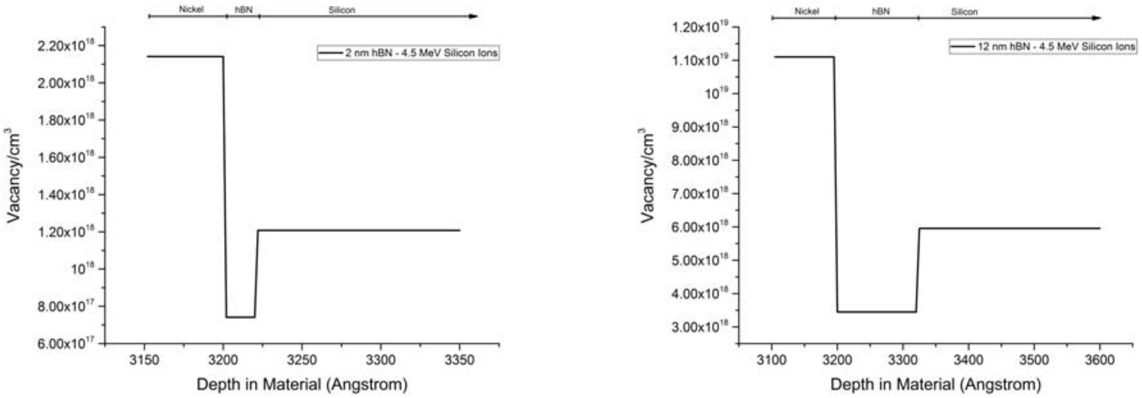

(a) 2 nm hBN sample.

(b) 12 nm hBN sample.

Figure 47. Average volumetric displacement for 4.5 MeV silicon ions across a 2 nm and 12 nm hBN device. The MIS device modeled in SRIM consisted of layers of gold (300 nm in depth), nickel (20 nm in depth), hBN (2 nm or 12 nm in depth), and silicon (3168 nm in depth) shown left to right in the graph.

Table 15. Average volumetric displacement values for 4.5 MeV silicon ions across a 2 nm and 12 nm hBN device.

Material	2 nm hBN	12 nm hBN
	$\frac{\text{Vacancy}}{\text{cm}^3}$	$\frac{\text{Vacancy}}{\text{cm}^3}$
Nickel	2.14×10^{18}	1.11×10^{19}
hBN	7.41×10^{17}	3.45×10^{18}
Silicon	1.21×10^{18}	5.96×10^{18}

The values in Table 15 represent the absolute number of displacements per volume caused from the experimental ion fluence. To convert a 4.5 MeV silicon ion fluence to a 1 MeV proton fluence, the values in Table 15 along with rearrangement of equation 41 shown as equation 42.

$$\frac{V_{vol}\left(\frac{\text{Vacancy}}{\text{cm}^3}\right)}{V_{ion}\left(\frac{\text{Vacancy}}{-\text{ion}}\right)\times 10^8\left(\frac{}{\text{cm}}\right)} = F\left(\frac{\text{ions}}{\text{cm}^2}\right) \tag{42}$$

The remaining unknown variable is V_{ion} which can be determined computationally through SRIM by using the same material geometry and 1 MeV protons. The same procedure and reasoning used to create Figures 46 and 47 discussed above was used to create Figures 48 and 49.

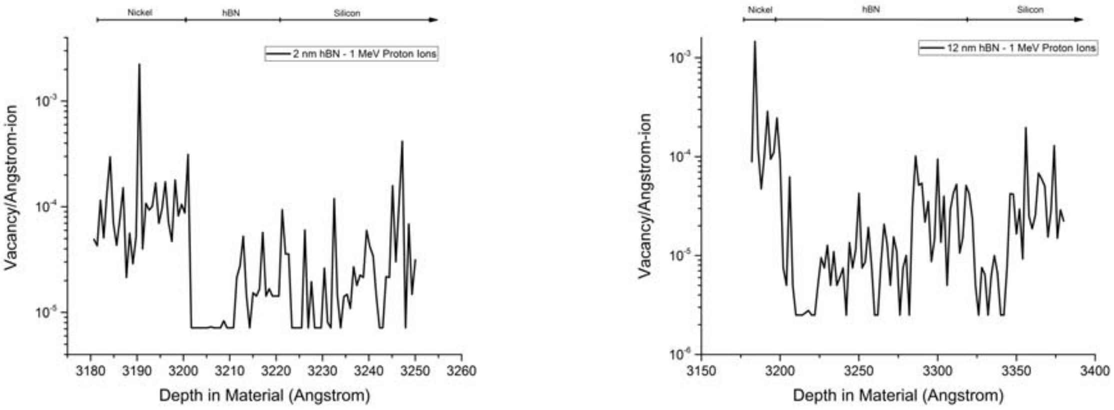

(a) 2 nm hBN sample.

(b) 12 nm hBN sample.

Figure 48. SRIM determined displacement per ion for 1 MeV protons across a 2 nm and 12 nm hBN device. The MIS device modeled in SRIM consisted of layers of gold (300 nm in depth), nickel (20 nm in depth), hBN (2 nm or 12 nm in depth), and silicon (3168 nm in depth) shown left to right in the graph. 200,000 particles were run in SRIM using quick calculation of damage to generate these plots

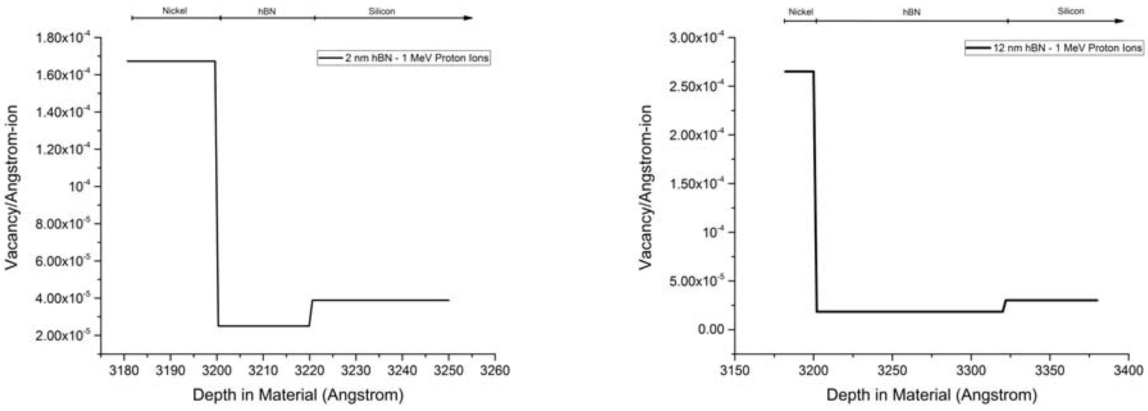

(a) 2 nm hBN sample.

(b) 12 nm hBN sample.

Figure 49. Average determined displacement per ion for 1 MeV protons across a 2 nm and 12 nm hBN device. The MIS device modeled in SRIM consisted of layers of gold (300 nm in depth), nickel (20 nm in depth), hBN (2 nm or 12 nm in depth), and silicon (3168 nm in depth) shown left to right in the graph.

Table 16. Average determined displacement per ion values for 1 MeV protons across a 2 nm and 12 nm hBN device.

Material	2 nm hBN	12 nm hBN
	$\frac{\text{Vacancy}}{\text{Å}-\text{ion}}$	$\frac{\text{Vacancy}}{\text{Å}-\text{ion}}$
Nickel	1.67×10^{-4}	2.65×10^{-4}
hBN	2.50×10^{-5}	1.84×10^{-5}
Silicon	3.88×10^{-5}	3.02×10^{-5}

The values shown in Table 16 represent $V_{ion,}$. A 1 MeV ion fluence can finally be calculated using the values from Tables 15 and 16 along with equation 42. The overall conversion result is shown in Table 17

Table 17. 4.5 MeV silicon ion fluence conversion to a 1 MeV proton fluence.

hBN Thickness (nm)	4.5 MeV silicon ion fluence ions/cm^2	1 MeV proton equivalent damage ion fluence ions/cm^2 (hBN)	1 MeV proton equivalent damage ion fluence ions/cm^2 (Si)
2	1.10×10^{12}	2.96×10^{14}	3.11×10^{14}
12	5.20×10^{12}	1.88×10^{15}	1.97×10^{15}

Appendix B. Ion Irradiation Beam Fluence Shot Settings

Table 18. Sample BN72915_13C (12 nm) ion beam settings per shot.

Measurement	Total Fluence Deposited (ions/cm^2)	Fluence per Pulse (ions/cm^2)	Pulse Length (μsec)
Ion Radiation Shot 1	1.00×10^9	1.01×10^9	32
Ion Radiation Shot 2	2.00×10^9	1.01×10^9	32
Ion Radiation Shot 3	4.20×10^9	1.01×10^9	32
Ion Radiation Shot 4	6.42×10^9	1.01×10^9	32
Ion Radiation Shot 5	1.05×10^{10}	1.01×10^9	32
Ion Radiation Shot 6	1.46×10^{10}	1.01×10^9	32
Ion Radiation Shot 7	3.06×10^{10}	1.01×10^9	32
Ion Radiation Shot 8	5.06×10^{10}	1.01×10^9	32
Ion Radiation Shot 9	9.03×10^{10}	1.01×10^9	32
Ion Radiation Shot 10	1.30×10^{11}	1.01×10^9	32
Ion Radiation Shot 11	1.70×10^{11}	1.01×10^9	32
Ion Radiation Shot 12	2.09×10^{11}	1.01×10^9	32
Ion Radiation Shot 13	2.48×10^{11}	1.01×10^9	32
Ion Radiation Shot 14	3.27×10^{11}	1.01×10^9	32
Ion Radiation Shot 15	4.83×10^{11}	1.01×10^9	32
Ion Radiation Shot 16	7.97×10^{11}	1.01×10^9	32
Ion Radiation Shot 17	1.43×10^{12}	1.01×10^9	32
Ion Radiation Shot 18	2.70×10^{12}	1.01×10^9	32
Ion Radiation Shot 19	5.20×10^{12}	1.01×10^9	32
Ion Radiation Shot 20	1.05×10^{13}	4.00×10^9	110
Ion Radiation Shot 21	2.13×10^{13}	4.00×10^9	110

Table 19. Sample BN52715B_13C (2 nm) ion beam settings per shot.

Measurement	Total Fluence Deposited (ions/cm^2)	Fluence per Pulse (ions/cm^2)	Pulse Length (μsec)
Ion Radiation Shot 1	5.02×10^{10}	1.96×10^9	90
Ion Radiation Shot 2	1.00×10^{11}	1.96×10^9	90
Ion Radiation Shot 3	5.98×10^{11}	1.96×10^9	90
Ion Radiation Shot 4	1.10×10^{12}	1.96×10^9	90
Ion Radiation Shot 5	6.07×10^{12}	1.96×10^9	90
Ion Radiation Shot 6	1.12×10^{13}	1.96×10^9	90
Ion Radiation Shot 7	2.13×10^{13}	1.96×10^9	90

Appendix C. Gamma Irradiation Data

C.1 Sample BN52715B_16B Results

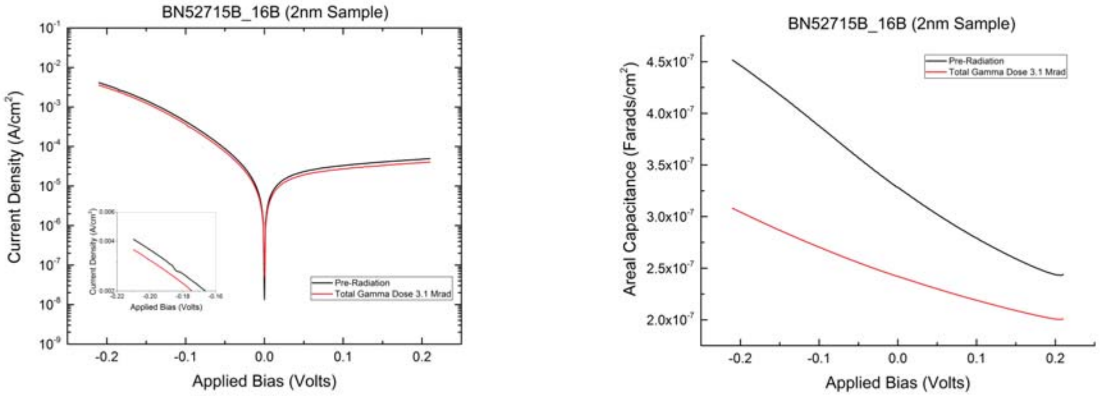

(a) I-V Plot

(b) C-V Plot

Figure 50. Sample BN52715B_16B normalized current and capacitance as a function of gamma dose and voltage. The inset graph in sub-figure (a) provides an expanded view of I-V measurements under negative voltage to show minor changes.

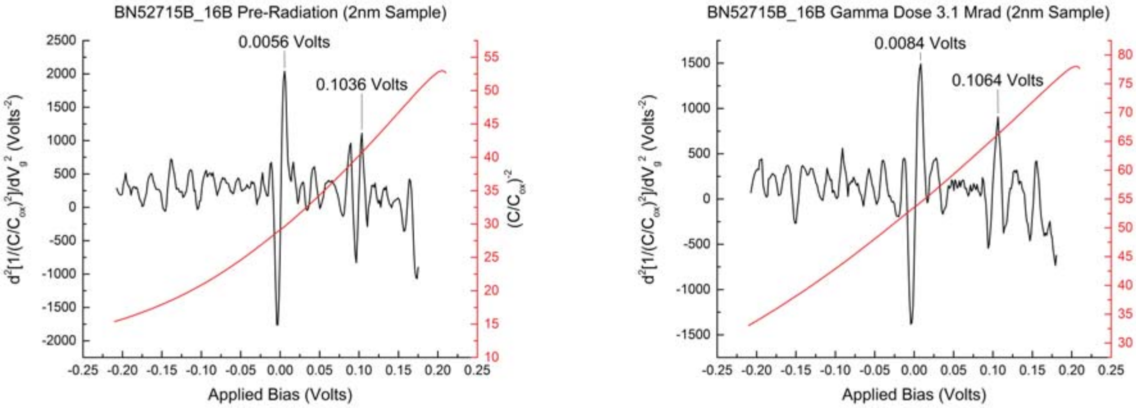

(a) Pre-Radiation

(b) Post Radiation

Figure 51. Sample BN52715B_16B hBN flat band voltage characterization using $d^2(1/C^2)/dV^2$ method to show no flat band voltage shift and detect breakdown.

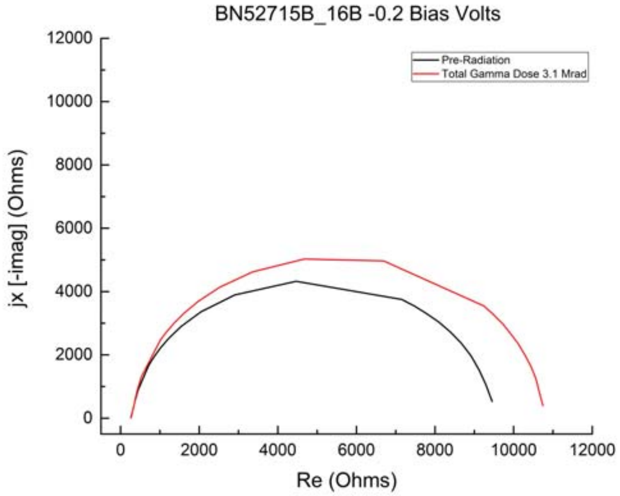

Figure 52. Sample BN52715B_16B impedance as a function of gamma dose under an applied gate bias of -0.2 volts.

Table 20. Conduction mechanism refined functional fitting for sample BN52715B_16B (2 nm) exposed to gamma radiation. Values within the tables represent the goodness of fit (R^2).

Conduction Mechanism	Pre-Radiation (Gamma Dose 0 Mrad) Refined Functional Fit		Post Radiation (Gamma Dose 3.1 Mrad) Refined Functional Fit	
	High Electric Field	Low Electric Field	High Electric Field	Low Electric Field
Tunneling	0.8676	0.4765	0.8672	0.4743
Frenkel Poole	0.8125	0.3754	0.8132	0.3756
Thermionic Emission	0.8550	0.3816	0.8560	0.3823
Ohmic	0.5726	0.5316	0.5732	0.5305
Space Charge Limited	0.9618	0.7915	0.9609	0.7803

C.2 Sample BN52715B_16C Results

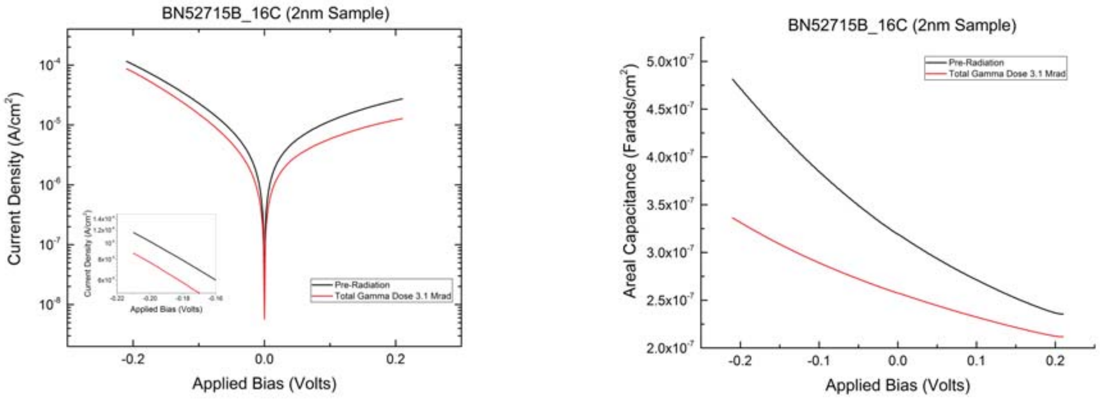

(a) I-V Plot

(b) C-V Plot

Figure 53. Sample BN52715B_16C normalized current and capacitance as a function of gamma dose and voltage. The inset graph in sub-figure (a) provides an expanded view of I-V measurements under negative voltage to show minor changes.

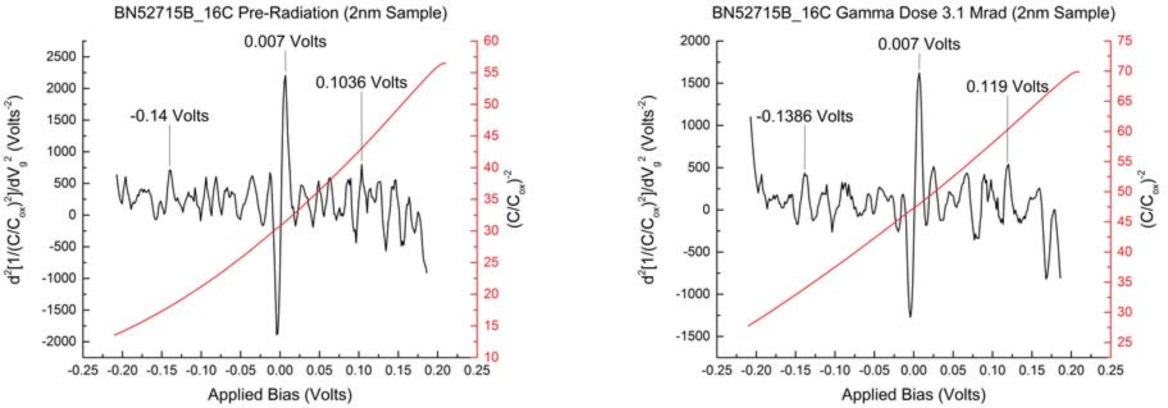

(a) Pre-Radiation

(b) Post Radiation

Figure 54. Sample BN52715B_16C hBN flat band voltage characterization using $d^2(1/C^2)/dV^2$ method to show no flat band voltage shift and detect breakdown.

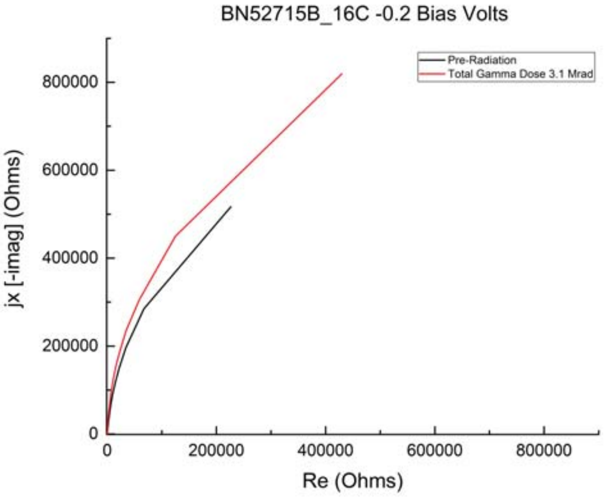

Figure 55. Sample BN52715B_16C impedance as a function of gamma dose under an applied gate bias of -0.2 volts.

Table 21. Conduction mechanism refined functional fitting for sample BN52715B_16C (2 nm) exposed to gamma radiation. Values within the tables represent the goodness of fit (R^2).

Conduction Mechanism	Pre-Radiation (Gamma Dose 0 Mrad) Refined Functional Fit		Post Radiation (Gamma Dose 3.1 Mrad) Refined Functional Fit	
	High Electric Field	Low Electric Field	High Electric Field	Low Electric Field
Tunneling	0.8151	0.4907	0.8408	0.4878
Frenkel Poole	0.7091	0.4166	0.7250	0.4133
Thermionic Emission	0.7345	0.4169	0.7523	0.4137
Ohmic	0.8002	0.6418	0.7516	0.6002
Space Charge Limited	0.9872	0.5087	0.9962	0.5521

C.3 Sample BN52715B_16D Results

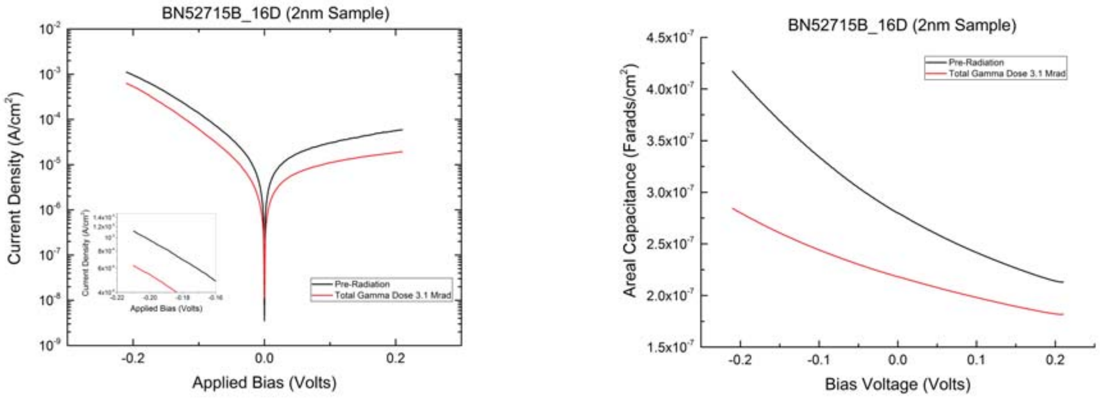

(a) I-V Plot

(b) C-V Plot

Figure 56. Sample BN52715B_16D normalized current and capacitance as a function of gamma dose and voltage. The inset graph in sub-figure (a) provides an expanded view of I-V measurements under negative voltage to show minor changes.

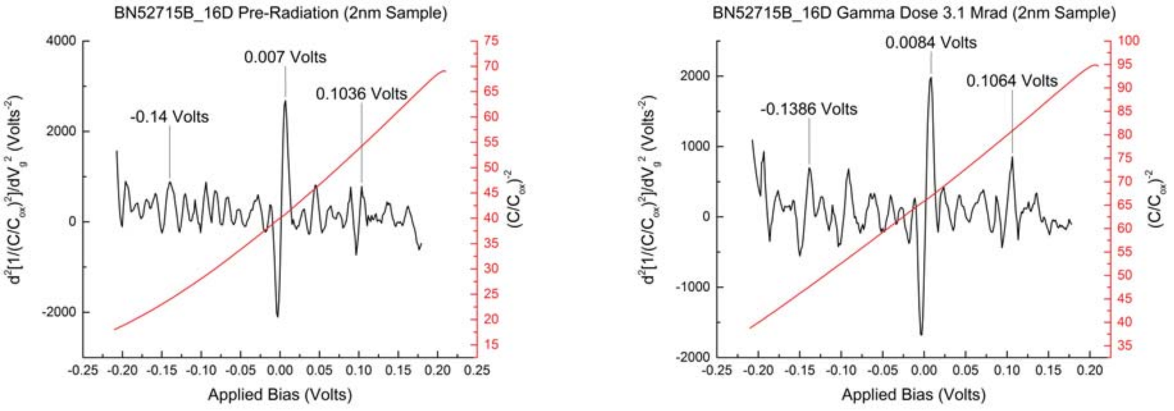

(a) Pre-Radiation

(b) Post Radiation

Figure 57. Sample BN52715B_16D hBN flat band voltage characterization using $d^2(1/C^2)/dV^2$ method to show no flat band voltage shift and detect breakdown.

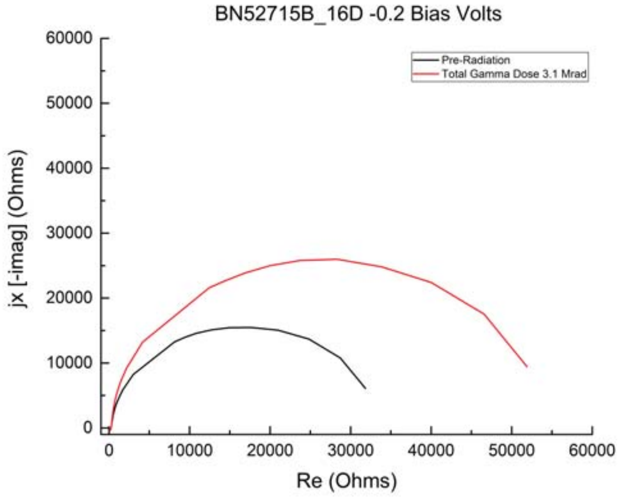

Figure 58. Sample BN52715B_16D impedance as a function of gamma dose under an applied gate bias of -0.2 volts.

Table 22. Conduction mechanism refined functional fitting for sample BN52715B_16D (2 nm) exposed to gamma radiation. Values within the tables represent the goodness of fit (R^2).

Conduction Mechanism	Pre-Radiation (Gamma Dose 0 Mrad) Refined Functional Fit		Post Radiation (Gamma Dose 3.1 Mrad) Refined Functional Fit	
	High Electric Field	Low Electric Field	High Electric Field	Low Electric Field
Tunneling	0.8813	0.4890	0.9144	0.4840
Frenkel Poole	0.7589	0.4042	0.7881	0.3994
Thermionic Emission	0.7902	0.4049	0.8219	0.4003
Ohmic	0.6688	0.5508	0.6209	0.5356
Space Charge Limited	0.9935	0.8244	0.9707	0.9471

C.4 Sample BN52715B_16E Results

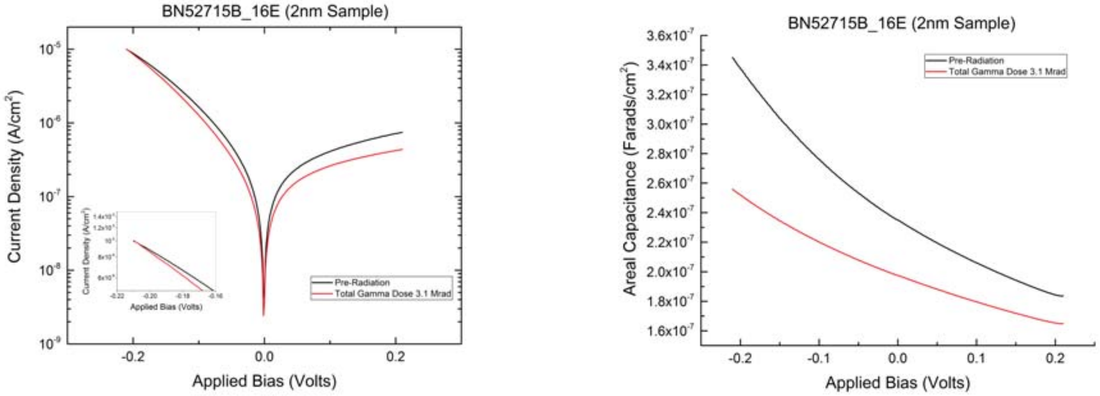

(a) I-V Plot

(b) C-V Plot

Figure 59. Sample BN52715B_16E normalized current and capacitance as a function of gamma dose and voltage. The inset graph in sub-figure (a) provides an expanded view of I-V measurements under negative voltage to show minor changes.

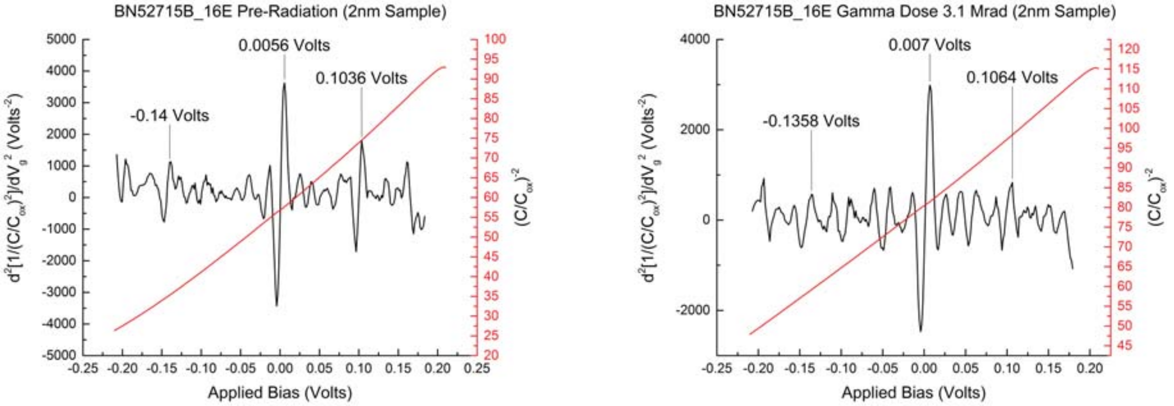

(a) Pre-Radiation

(b) Post Radiation

Figure 60. Sample BN52715B_16E hBN flat band voltage characterization using $d^2(1/C^2)/dV^2$ method to show no flat band voltage shift and detect breakdown.

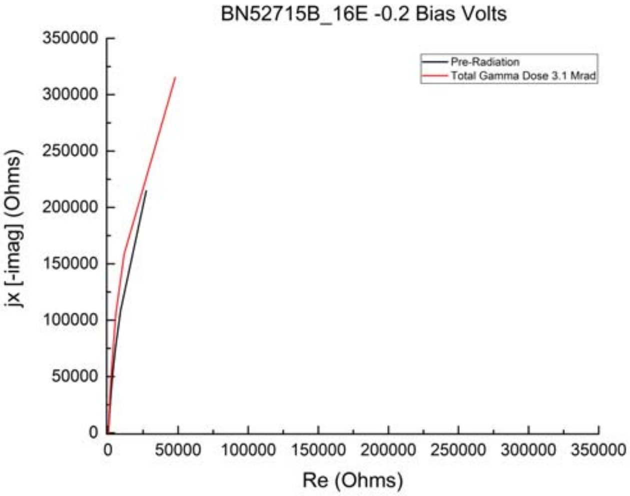

Figure 61. Sample BN52715B_16E impedance as a function of gamma dose under an applied gate bias of -0.2 volts.

Table 23. Conduction mechanism refined functional fitting for sample BN52715B_16E (2 nm) exposed to gamma radiation. Values within the tables represent the goodness of fit (R^2).

Conduction Mechanism	Pre-Radiation (Gamma Dose 0 Mrad) Refined Functional Fit		Post Radiation (Gamma Dose 3.1 Mrad) Refined Functional Fit	
	High Electric Field	Low Electric Field	High Electric Field	Low Electric Field
Tunneling	0.8275	0.4799	0.8704	0.4764
Frenkel Poole	0.7245	0.4023	0.7586	0.3984
Thermionic Emission	0.7531	0.4029	0.7902	0.3992
Ohmic	0.7460	0.5913	0.6712	0.5590
Space Charge Limited	0.9967	0.6199	0.9951	0.8099

C.5 Sample BN52715B_16F Results

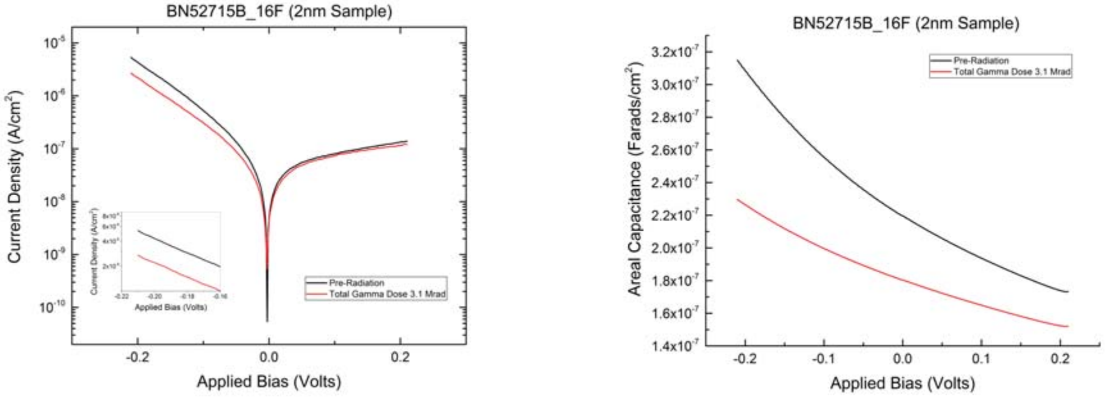

(a) I-V Plot

(b) C-V Plot

Figure 62. Sample BN52715B_16F normalized current and capacitance as a function of gamma dose and voltage. The inset graph in sub-figure (a) provides an expanded view of I-V measurements under negative voltage to show minor changes.

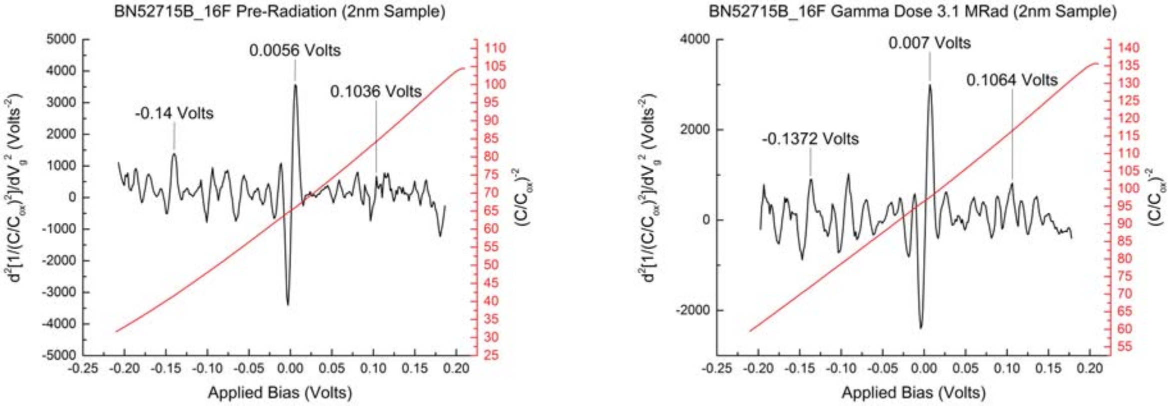

(a) Pre-Radiation

(b) Post Radiation

Figure 63. Sample BN52715B_16F hBN flat band voltage characterization using $d^2(1/C^2)/dV^2$ method to show no flat band voltage shift and detect breakdown.

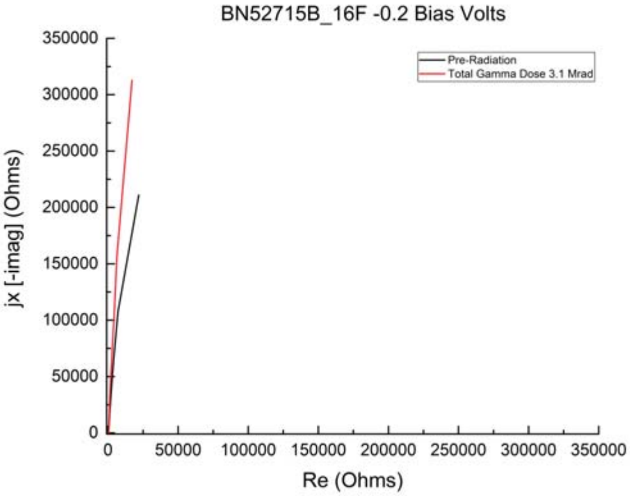

Figure 64. ample BN52715B_16F impedance as a function of gamma dose under an applied gate bias of -0.2 volts.

Table 24. Conduction mechanism refined functional fitting for sample BN52715B_16F (2 nm) exposed to gamma radiation. Values within the tables represent the goodness of fit (R^2).

Conduction Mechanism	Pre-Radiation (Gamma Dose 0 Mrad) Refined Functional Fit		Post Radiation (Gamma Dose 3.1 Mrad) Refined Functional Fit	
	High Electric Field	Low Electric Field	High Electric Field	Low Electric Field
Tunneling	0.9029	0.4684	0.8908	0.4754
Frenkel Poole	0.7944	0.3868	0.7861	0.3940
Thermionic Emission	0.8279	0.3877	0.8189	0.3947
Ohmic	0.6240	0.5454	0.6418	0.5623
Space Charge Limited	0.9734	0.9472	0.9801	0.7797

C.6 Sample BN72915_10B Results

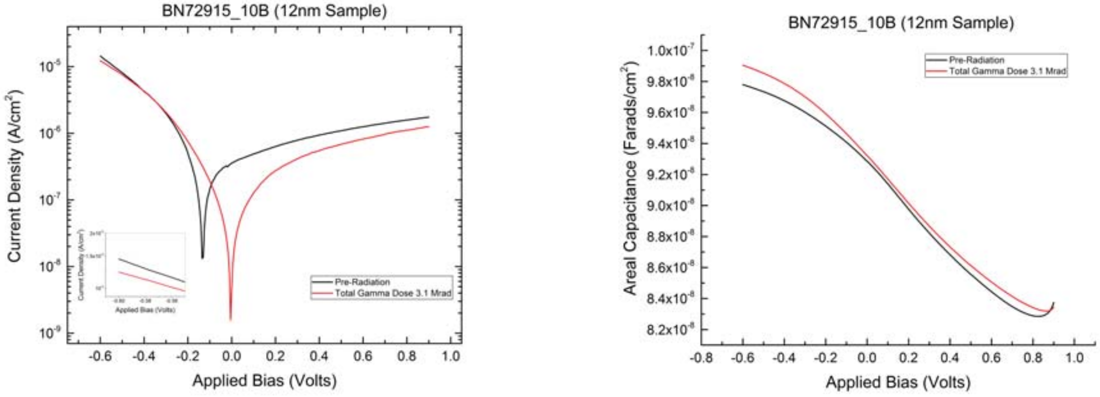

(a) I-V Plot

(b) C-V Plot

Figure 65. Sample BN72915_10B normalized current and capacitance as a function of gamma dose and voltage. The inset graph in sub-figure (a) provides an expanded view of I-V measurements under negative voltage to show minor changes.

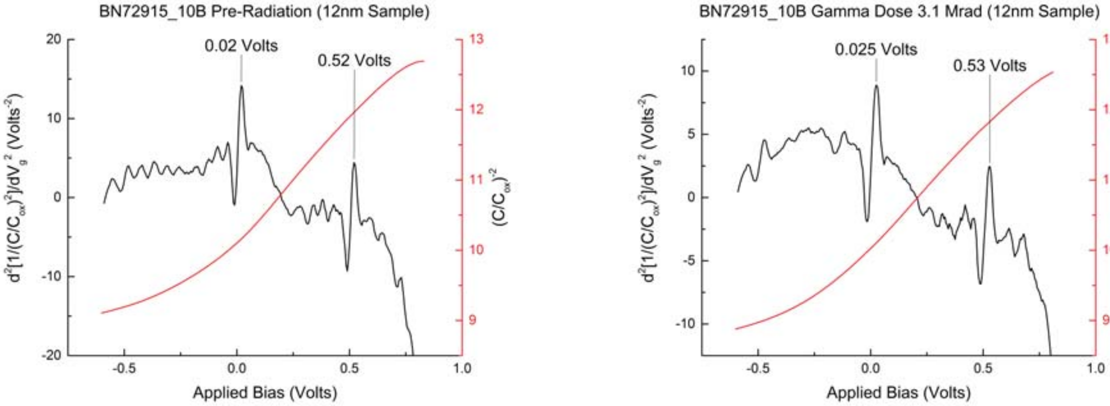

(a) Pre-Radiation

(b) Post Radiation

Figure 66. Sample BN72915_10B hBN flat band voltage characterization using $d^2(1/C^2)/dV^2$ method to show no flat band voltage shift and detect breakdown.

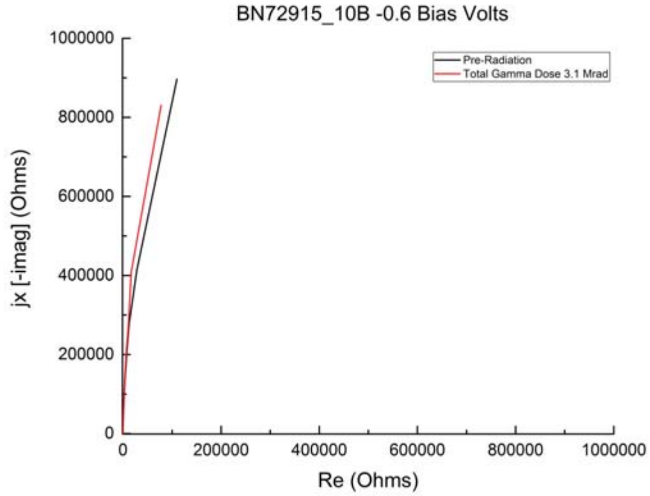

Figure 67. Sample BN72915_10B impedance as a function of gamma dose under an applied gate bias of -0.6 volts.

Table 25. Conduction mechanism refined functional fitting for sample BN72915_10B (12 nm) exposed to gamma radiation. Values within the tables represent the goodness of fit (R^2).

Conduction Mechanism	Pre-Radiation (Gamma Dose 0 Mrad) Refined Functional Fit		Post Radiation (Gamma Dose 3.1 Mrad) Refined Functional Fit	
	High Electric Field	Low Electric Field	High Electric Field	Low Electric Field
Tunneling	0.8231	0.3642	0.7870	0.4366
Frenkel Poole	0.8671	0.3823	0.8280	0.3700
Thermionic Emission	0.9219	0.4614	0.8831	0.4174
Ohmic	0.4868	0.5273	0.5054	0.5581
Space Charge Limited	0.9103	0.6658	0.9625	0.8439

C.7 Sample BN72915_22B Results

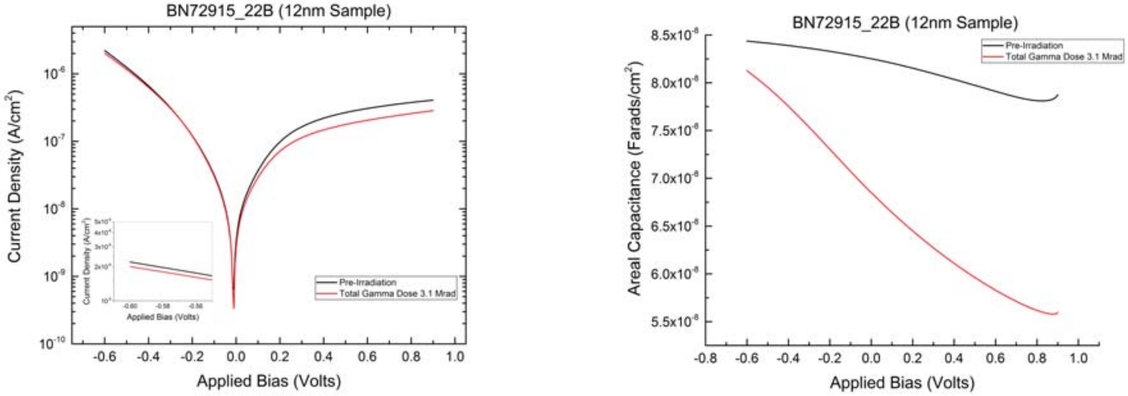

(a) I-V Plot

(b) C-V Plot

Figure 68. Sample BN72915_22B normalized current and capacitance as a function of gamma dose and voltage. The inset graph in sub-figure (a) provides an expanded view of I-V measurements under negative voltage to show minor changes.

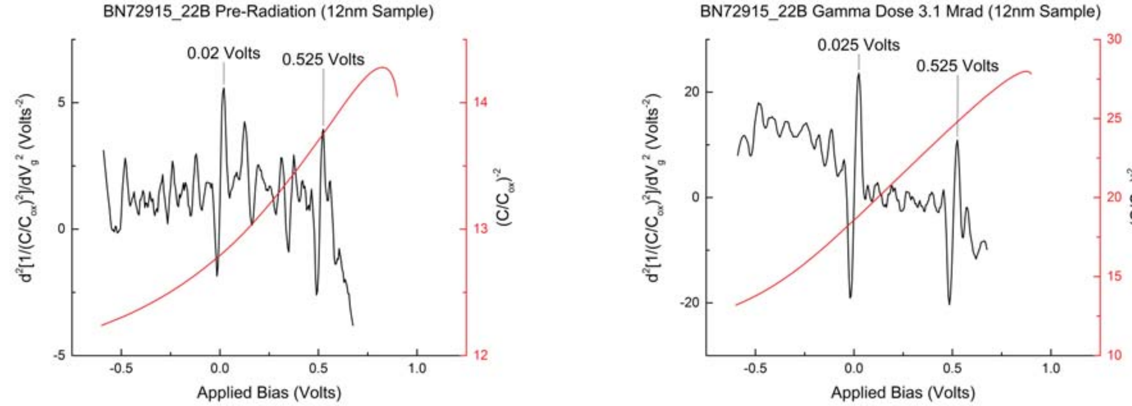

(a) Pre-Radiation

(b) Post Radiation

Figure 69. Sample BN72915_22B hBN flat band voltage characterization using $d^2(1/C^2)/dV^2$ method to show no flat band voltage shift and detect breakdown.

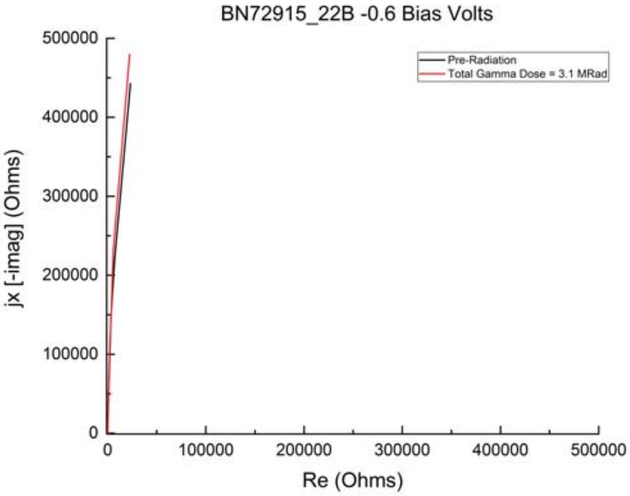

Figure 70. Sample BN72915_22B impedance as a function of gamma dose under an applied gate bias of -0.6 volts.

Table 26. Conduction mechanism refined functional fitting for sample BN72915_22B (12 nm) exposed to gamma radiation. Values within the tables represent the goodness of fit (R^2).

Conduction Mechanism	Pre-Radiation (Gamma Dose 0 Mrad) Refined Functional Fit		Post Radiation (Gamma Dose 3.1 Mrad) Refined Functional Fit	
	High Electric Field	Low Electric Field	High Electric Field	Low Electric Field
Tunneling	0.8291	0.4363	0.7933	0.4332
Frenkel Poole	0.8683	0.3767	0.8471	0.3733
Thermionic Emission	0.9224	0.4323	0.9041	0.4281
Ohmic	0.4814	0.5480	0.4717	0.5686
Space Charge Limited	0.9069	0.7879	0.9400	0.8812

C.8 Sample BN72915_22D Results

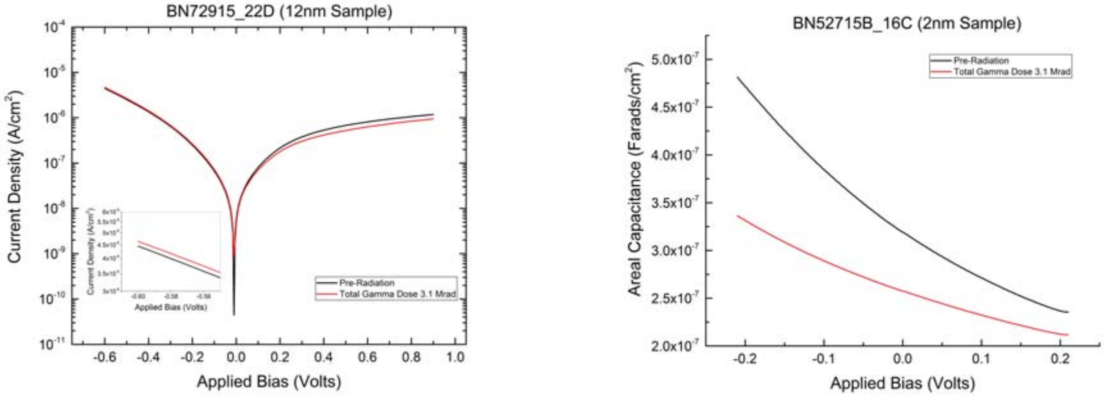

(a) I-V Plot

(b) C-V Plot

Figure 71. Sample BN72915_22D normalized current and capacitance as a function of gamma dose and voltage. The inset graph in sub-figure (a) provides an expanded view of I-V measurements under negative voltage to show minor changes.

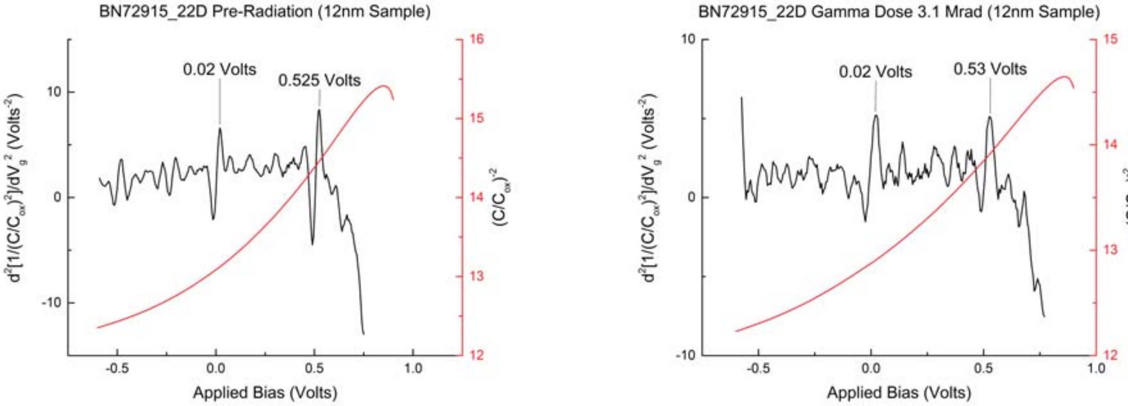

(a) Pre-Radiation

(b) Post Radiation

Figure 72. Sample BN52715B_16C hBN flat band voltage characterization using $d^2(1/C^2)/dV^2$ method to show no flat band voltage shift and detect breakdown.

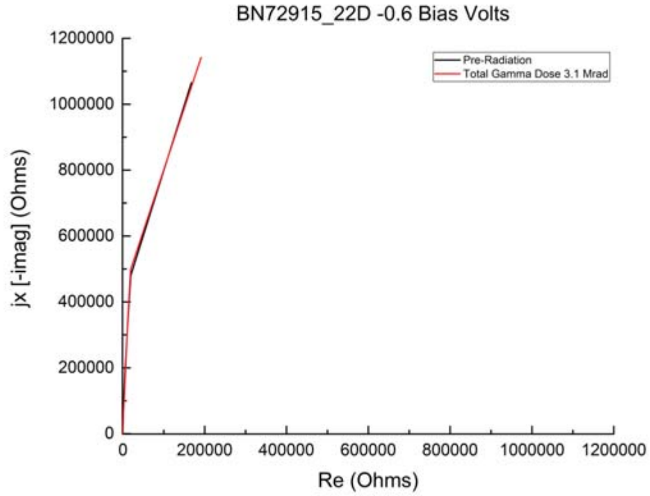

Figure 73. Sample BN72915_22D impedance as a function of gamma dose under an applied gate bias of -0.6 volts.

Table 27. Conduction mechanism refined functional fitting for sample BN72915_22D (12 nm) exposed to gamma radiation. Values within the tables represent the goodness of fit (R^2).

Conduction Mechanism	Pre-Radiation (Gamma Dose 0 Mrad) Refined Functional Fit		Post Radiation (Gamma Dose 3.1 Mrad) Refined Functional Fit	
	High Electric Field	Low Electric Field	High Electric Field	Low Electric Field
Tunneling	0.8224	0.4403	0.8239	0.4382
Frenkel Poole	0.8642	0.3782	0.8636	0.3798
Thermionic Emission	0.9188	0.4312	0.9177	0.4324
Ohmic	0.4847	0.5497	0.4847	0.5496
Space Charge Limited	0.9163	0.8016	0.9150	0.8009

C.9 Summary of Results

Table 28. Measured hBN resistance obtained through CNLS impedance fitting for 2 nm and 12 nm samples irradiated from a Co-60 source

Sample	Pre-Radiation			Post Radiation		
	Ohms	Error +/-	STD	Ohms	Error +/-	STD
BN52715B_16B	8183	272	0.033	10313	35	0.0034
BN52715B_16C	1.419E6	6566	0.0046	1.975E6	26847	0.0136
BN52715B_16D	27073	1253	0.0463	47631	2452	0.0515
BN52715B_16BE	1.878E6	9656	0.0051	2.164E6	13457	0.0062
BN52715B_16F	2.364E6	625685	0.0109	6.375E6	101100	0.0159
BN72915_10B	8.243E6	553900	0.0672	9.10E6	159500	0.0175
BN72915_22B	8.69E6	144100	0.0166	1.044E7	550900	0.0528
BN72915_22D	Error too large to obtain a meaningful value					

Bibliography

1. B. Barnett, "Ionizing and Non-Ionizing Radiation Effects in Thin Layer Hexagonal Boron Nitride (AFIT-ENP-MS-15-M-099)," Master's thesis, Air Force Institute of Technology (AFIT), 3 2015.

2. R. F. Pierret, *Semiconductor Device Fundementals.* Addison-Wesley Publishing Company, 1996.

3. I. Meric, C. R. Dean, N. Petrone, L. Wang, J. Hone, P. Kim, and K. L. Shepard, "Graphene Field-Effect Transistors Based on Boron Nitride Dielectrics," *Proc. IEEE*, vol. 101, no. 7, pp. 1609–1619, 7 2013.

4. S. A. Francis, J. C. Petrosky, J. W. McClory, and C. D. Cress, "Effects of Proton and X-ray Irradiation on Graphene Field-Effect Transistors with Thin Gate Dielectrics," *IEEE Trans. Nucl. Sci.*, vol. 61, no. 6, pp. 3010–3017, 12 2014.

5. H. Hirai, H. Tsuchiya, Y. Kamakura, N. Mori, and M. Ogawa, "Electron Mobility Calculation for Graphene on Substrates," *Journal of Applied Physics*, vol. 116, 2014.

6. Q. S. Paduano, M. Snure, J. Bondy, and T. W. C. Zens, "Self-terminating Growth in Hexagonal Boron Nitride by Metal Organic Chemical Vapor Deposition," *Appl. Phys. Express*, vol. 7, no. 7, p. 071004, 6 2014.

7. P. Sutter, J. Lahiri, P. Zahl, B. Wang, and E. Sutter, "Scalable Synthesis of Uniform Few-Layer Hexagonal Boron Nitride Dielectric Films," *Nano Letters*, no. 13, pp. 276–281, 2013.

8. Y. Hattori, T. Taniguchi, K. Watanabe, and K. Nagashio, "Layer-by-layer dielectric breakdown of hexagonal boron nitride." *ACS Nano*, vol. 9, no. 1, pp. 916–21, 1 2015.

9. B. He, M. Qui, M. F. Yuen, and W. J. Zhang, "Electrical Properties and Electronic Structure of Si Implanted hBN Films," *Applied Physics Letters*, vol. 105, 7 2014.

10. L. Ci, L. Song, C. Jin, D. Jariwala, D. Wu, Y. Li, A. Srivastava, Z. F. Wang, K. Storr, L. Balicas, F. Liu, and P. M. Ajayan, "Atomic Layers of Hybridized Boron Nitride and Graphene Domains," *Nature Materials*, vol. 9, no. 5, pp. 430–435, 2 2010.

11. C. Steinborn, M. Herrmann, U. Keitel, A. Schönecker, J. Räthel, D. Rafaja, and J. Eichler, "Correlation between microstructure and electrical resistivity of hexagonal boron nitride ceramics," *Journal of the European Ceramic Society*, vol. 33, no. 6, pp. 1225–1235, 6 2013.

12. G. Shi, Z. Liu, Y. Gong, W. Gao, B. Li, J. Kono, J. Lou, R. Vajtai, P. Sharma, and P. Ajayan, "Boron Nitride - Graphene Nanocapacitor and the Origins of Anomalous Size Dependent Increase of Capacitance," *Nano Letters*, vol. 14, pp. 1739–1744, 2014.

13. J. Li, S. Majety, R. Dahal, W. P. Zhao, J. Y. Lin, and H. X. Jiang, "Dielectric strength, optical absorption, and deep ultraviolet detectors of hexagonal boron nitride epilayers," *Applied Physics Letters*, vol. 101, 10 2012.

14. A. Nag, K. Raidongia, K. P. S. S. Hembram, R. Datta, U. V. Waghmare, and C. N. R. Rao, "Graphene analogues of BN: novel synthesis and properties." *ACS Nano*, vol. 4, no. 3, pp. 1539–44, 3 2010.

15. T. C. Doan, S. Majety, S. Grenadier, J. Li, J. Y. Lin, and H. X. Jiang, "Hexagonal Boron Nitride Thin Film Thermal Neutron Detectors with High Energy Resolution of the Reaction Products," *Nuclear Instruments and Methods in Physics Research Section A: Accelerators, Spectrometers, Detectors and Associated Equipment*, vol. 783, pp. 121–127, 5 2015.

16. L. Song, L. Ci, H. Lu, P. B. Sorokin, C. Jin, J. Ni, A. G. Kvashnin, D. G. Kvashnin, J. Lou, B. I. Yakobson, and P. M. Ajayan, "Large scale growth and characterization of atomic hexagonal boron nitride layers." *Nano Lett*, vol. 10, no. 8, pp. 3209–15, 8 2010.

17. M. S. O. Madelung, U. Rössler, Ed., *Group IV Elements, IV-IV and III-V Compounds. Part a - Lattice Properties.* Springer Berlin Heidelberg, 2001.

18. C. R. Dean, A. F. Young, I. Meric, C. Lee, L. Wang, S. Sorgenfrei, K. Watanabe, T. Taniguchi, P. Kim, K. L. Shepard, and J. Hone, "Boron Nitride Substrates for High-Quality Graphene Electronics," *Nature Nanotech*, vol. 5, no. 10, pp. 722–726, 8 2010.

19. O. Özdemir, M. Anutgan, T. Aliyeva-Anutgan, s. Atlgan, and B. Katrcolu, "Instability phenomenon originated from the disordered layer of the plasma-deposited BN film/c-Si interface assessed through the MIS structure by admittance measurement," *Semiconductor Science and Technology*, vol. 23, no. 2, p. 025006, 1 2008.

20. S. Sze and K. K. Ng, *Physics of Semiconductor Devices.* Wiley Interscience, 2007.

21. K. Instruments, "Gate Dielectric Capacitance-Voltage Characterization Using the Model 4200 Semiconductor Characterization System," *Keithley Application Note Series*, no. 2239, 2006.

22. C. Morosanu, *Thin Film By Chemical Vapour Deposition.* Elsevier, 1990.

23. F.-C. Chiu, "A Review on Conduction Mechanisms in Dielectric Films," *Advances in Materials Science and Engineering*, vol. 2014, pp. 1–18, 2014.

24. G.-H. Lee, Y.-J. Yu, C. Lee, C. Dean, K. L. Shepard, P. Kim, and J. Hone, "Electron tunneling through atomically flat and ultrathin hexagonal boron nitride," *Appl. Phys. Lett.*, vol. 99, no. 24, p. 243114, 2011.

25. Y. Barsukov and J. R. MacDonald, "Electrochemical Impedance Spectroscopy," *Characterization of Materials*, 2012.

26. M. Brotzmann, H.-G. Gehrke, U. Vetter, and H. Hofsass, "Modeling the diode characteristics of boron nitride-silicon carbide heterojunctions," *Applied Physics Letters*, no. 97, 2010.

27. J. R. M. Evgenij Barsoukov, Ed., *Impedance Spectroscopy Theory, Experiment, and Applications (2nd Ed).* Wiley Interscience, 2005.

28. J. R. Srour, C. J. Marshall, and P. W. Marshall, "Review of displacement damage effects in silicon devices," *IEEE Trans. Nucl. Sci.*, vol. 50, no. 3, pp. 653–670, 6 2003.

29. K. Instruments, "C-V Characterization of MOS Capacitors Using the Model 4200-SCS Semiconductor Characterization System," *Keithley Application Note Series*, 2007.

30. D. K. Schroder, "Direct and Rapid Method for Determining Flatband Voltage from Non-Equilibrium Capacitance Voltage Data," *Proceedings of the Symposium on Diagnostic Techniques for Semiconductor Materials and Devices*, 1992.

31. D. K. Schroder, *Semiconductor Material and Device Characterization.* Wiley Interscience, 2006.

32. J. R. MacDonald, *Complex Nonlinear Least Squares (CNLS) Immittance, Inversion, and Simulation Fitting Programs LEVM/LEVMW Manual*, June 2013.

33. J. F. Ziegler, *SRIM: The Stopping and Range of Ions in Matter.* On demand printing by LuLu.com, 2015.

REPORT DOCUMENTATION PAGE	*Form Approved* *OMB No. 0704–0188*

1. REPORT DATE (DD–MM–YYYY) 24-03-2016	2. REPORT TYPE Master's Thesis	3. DATES COVERED *(From — To)* September 2014 - March 2016

4. TITLE AND SUBTITLE Radiation Effects in Thin Film Hexagonal Boron Nitride	5a. CONTRACT NUMBER 5b. GRANT NUMBER 5c. PROGRAM ELEMENT NUMBER
6. AUTHOR(S) Kaminski, Nathaniel M, CPT, USA	5d. PROJECT NUMBER 5e. TASK NUMBER 5f. WORK UNIT NUMBER
7. PERFORMING ORGANIZATION NAME(S) AND ADDRESS(ES) Air Force Institute of Technology Graduate School of Engineering and Management (AFIT/EN) 2950 Hobson Way Wright-Patterson AFB, OH 45433-7765	8. PERFORMING ORGANIZATION REPORT NUMBER AFIT-ENP-MS-16-M-072
9. SPONSORING / MONITORING AGENCY NAME(S) AND ADDRESS(ES) Air Force Research Laboratory Dr. Michael R. Snure 2241 Avionic Circle Wright-Patterson AFB, OH 45433 michael.snure@us.af.mil	10. SPONSOR/MONITOR'S ACRONYM(S) AFRL/RY 11. SPONSOR/MONITOR'S REPORT NUMBER(S)

12. DISTRIBUTION / AVAILABILITY STATEMENT

Distribution Statement A. Approved for Public Release; Distribution Unlimited

13. SUPPLEMENTARY NOTES

This material is declared a work of the U.S. Government and is not subject to copyright protection in the United States.

14. ABSTRACT

The radiation response of 2 nm and 12 nm hexagonal boron nitride (hBN) thin film insulators was studied using metal insulator semiconductor (MIS) devices. Current-voltage, capacitance-voltage, and impedance spectroscopy measurements were compared to quantify changes in hBN resistance due to radiation damage. MIS devices exposed to a gamma total dose deposition of 3.1 Mrad(Si) from a Co-60 source exhibited a small increase in hBN resistance and no observable C-V shift associated with charge trapping. MIS devices irradiated with 4.5 MeV silicon ions showed no significant resistivity decrease to a threshold fluence of 1×10^{12} for the 2 nm sample and 5×10^{12} ions/cm^2 for the 12 nm sample, beyond which both devices exhibited hard dielectric breakdown. This result suggests a correlation between threshold ion fluence and a thickness dependent critical density of displacement defects. Conduction mechanism fitting showed a transition from electrode limited conduction to bulk limited conduction mechanisms at threshold ion fluence in both the 2 nm and 12 nm hBN samples, however, this result is inconclusive and requires further research.

15. SUBJECT TERMS

Boron Nitride, hBN, Semiconductor Radiation Effects, Radiation Resistant Dielectric, Thin Film Dielectric, MIS Device

16. SECURITY CLASSIFICATION OF:			17. LIMITATION OF ABSTRACT	18. NUMBER OF PAGES	19a. NAME OF RESPONSIBLE PERSON LtCol Michael R. Hogsed, AFIT/ENP
a. REPORT	b. ABSTRACT	c. THIS PAGE			19b. TELEPHONE NUMBER (Include Area Code)
U	U	U	UU	121	(937) 255-3636 x4547 Michael.Hogsed@afit.edu

Standard Form 298 (Rev. 8–98)
Prescribed by ANSI Std. Z39.18